Armin Moser

Crystal Structure Solution Based on Grazing Incidence X-ray Diffraction

Software Development and Application to Organic Films

Doctoral Thesis

For obtaining the Doctoral Degree
Doktor der technischen Wissenschaften

Doctoral Programme of Technical Sciences
Technical Physics

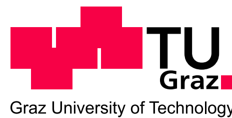

Graz University of Technology

Supervisor:

Ao. Univ.-Prof. Dr. Roland Resel
Institut of Solid State Physics

May, 2012

Deutsche Fassung:
Beschluss der Curricula-Kommission für Bachelor-, Master- und Diplomstudien vom 10.11.2008
Genehmigung des Senates am 1.12.2008

EIDESSTATTLICHE ERKLÄRUNG

Ich erkläre an Eides statt, dass ich die vorliegende Arbeit selbstständig verfasst, andere als die angegebenen Quellen/Hilfsmittel nicht benutzt, und die den benutzten Quellen wörtlich und inhaltlich entnommene Stellen als solche kenntlich gemacht habe.

Graz, am 03.05.2012

(Unterschrift)

Englische Fassung:

STATUTORY DECLARATION

I declare that I have authored this thesis independently, that I have not used other than the declared sources / resources, and that I have explicitly marked all material which has been quoted either literally or by content from the used sources.

05/03/2012
date

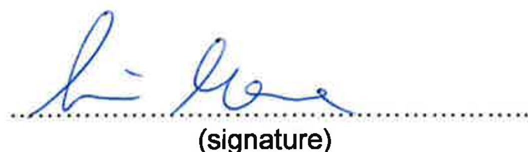

(signature)

To Martina

Thank you ...

After three years, it is time to say thank you to a lot of people without whom this work would not have been possible.

First of all, I would like to thank my supervisor **Roland Resel** who got hold of the FWF funding for my PhD position and financed all the travels to conferences and synchrotrons. But more importantly I appreciate his openness and the liberties he leaves to everyone to work on their own and focus on their interests. In my opinion this creates the good atmosphere and creativity in his working group. Thank you.

It was a great time in the office I shared with **Markus Koini, Oliver Werzer, Heinz-Georg Flesch, Karolf Marguc, Jiří Novák, Tatjana Ðuric, Alfred Neuhold, Markus Neuschitzer, Reinhold Hetzel, Michael Dohr,** and **Alexander Pichler**. You had an open ear for all kinds of questions and discussions. It is pleasant to enter the office and meet friends, not just colleagues. I have learned a lot about *"Life, the* **q**-*space and everything"* from all of you.

Special thanks to **Tatjana Ðuric** for reading my thesis and giving very valuable comments and critics about it. She even sacrificed one bridge day just to read my thesis. Thanks a lot.

For company at the beamtimes at Hasylab as well as suggestions and discussions about PyGid and crystal structure solving I thank **Ingo Salzmann** and **Martin Oehzelt**. Your enthusiasm for your research was inspiring.

For discussions and support regarding the structure solution of the pentacene thin-film phase I thank **Dmitrii Nabok** and **Peter Puschnig**.

It was a pleasure to meet **Gabin Gbabode, Yves Geerts,** and **Michele Sferazza** from Brussels as well as **Raffaele Guido Della Valle**, and **Elisabetta Venuti** from Bologna. It was all of you who created an enjoyable atmosphere at our meetings in Bologna, Brussels and Graz.

At the Cornell High Energy Synchrotron source I thank **Detlef-M. Smilgies** and **Arthur Woll** for their support during our beamtimes. I was delighted by the atmosphere at this facility.

For the preparation of several pentacene samples I thank **Anja Haase** and **Alexander Fian** as well as **Jan Ivanco** for preparing a nice set of sexithiophene samples for us.

Abstract

Organic semiconductors in organic electronic devices generally exist as thin films and both their structural quality and crystalline order significantly impact the device performance. Hence, it is of major importance to solve their crystal structures. However, in thin films, often surface-induced crystallographic phases form which are not existent in powders or single crystals. As a consequence their crystal structures cannot be solved with the main established techniques, i.e. single-crystal and powder diffraction. It is therefore desirable to develop a procedure to solve surface induced crystal structures from grazing incidence X-ray diffraction – a perfect technique to investigate thin (organic) films. For this purpose the software PyGid was developed.

PyGid is tailored to the evaluation of reciprocal space maps recorded with a one-dimensional detector. The most important features of PyGid are quick and easy visualization of the data, transformation to q-space, indexation of Bragg peaks as well as proper intensity extraction. Crystal structures can then be obtained with any program that can fit molecular packings to a list of measured intensities. In the present work, concepts and some implementation details will be given. Up to now, PyGid was used to solve three surface induced phases of organic molecules. With the help of these examples, the developed structure solution procedure will be introduced and its possibilities and shortcomings will be discussed.

Another major – but still unsolved – point in organic thin film research is the question why surface induced phases form. The lack of knowledge in this field is partly due to the fact that studies published in literature are primarily focused on morphology and not on crystallographic properties. Because of that the capabilities of PyGid were used to thorougly investigate crystallographic properties of promising organic semiconductors pentacene and sexithiophene. The thermal expansion and thermal phase behavior of pentacene thin films as well as its growth on organic dielectrics was analyzed. Furthermore, the influence of growth parameters on the phase behavior of α-sexithiophene films was investigated

Technical Note

Parts of this work are heavily based or literally cited from the masters thesis of myself (Moser; 2008). As this paragraph these parts are typset in a sans serif fonts to distinguish them from the rest of this work.

Kurzfassung

Dünne Schichten organischer Moleküle sind ein wesentlicher Teil organischer Elektronik. Die Kristallstrukturen dieser Schichten haben einen maßgebenden Einfluss auf die physikalischen Eigenschaften von organischen Elektronikbauteilen. Aus diesem Grund ist es von großer Bedeutung, diese Kristallstrukturen zu bestimmen. Da sich in dünnen Schichten aber oft oberflächeninduzierte Kristallstrukturen bilden, ist es nicht möglich, eine der beiden Standardmethoden – Röntgenstreuung an Einkristallen oder Pulvern – zu verwenden. Aus diesem Grund ist es notwendig, eine Methode zu entwickeln, um oberflächeninduzierte Kristallstrukturen mit Röntgenstreuung unter streifendem Einfall zu lösen. Um dies zu bewerkstelligen, wurde die Software PyGid entwickelt.

PyGid ist auf die Auswertung von zweidimensionalen Abbildungen des reziproken Raums, die mit einem eindimensionalen Detektor gemessen wurden, ausgelegt. Wichtige Anwendungen von PyGid sind schnelle und einfache Darstellung von Daten, Transformation dieser Daten in den reziproken Raum, Indizierung von Bragg-Reflexen und die Extraktion von Intensitäten. Kristallstrukturen können dann mit jeder Software bestimmt werden, die es erlaubt, die Packung von Molekülen an gemessene Strukturfaktoren anzupassen. In der vorliegenden Arbeit werden die Konzepte und einige implementationsspezifische Details von PyGid vorgestellt. Unter Anwendung von PyGid wurden bis jetzt drei oberflächeninduzierte Kristallstrukturen gelöst. Diese Beispiele werden verwendet um vorzustellen, wie PyGid im konkreten genutzt werden kann, um Kristallstrukturen zu lösen. Im Weiteren werden die Möglichkeiten und Einschränkungen der vorgestellten Methode diskutiert.

Eine weitere wichtige Frage in der Untersuchung von organischen dünnen Schichten ist, warum sich oberflächeninduzierte Phasen überhaupt bilden. In der Literatur ist zu diesem Thema wenig bekannt, da die meisten Studien sich hauptsächlich mit Morphologie und nicht mit Kristallstrukturen beschäftigen. Um diese Lücke zu schließen, wurde PyGid im Laufe dieser Arbeit eingesetzt, um die kristallographischen Eigenschaften von wichtigen organischen Halbleitern zu untersuchen. So wurde die thermische Ausdehnung sowie das thermische Phasenverhalten von dünnen Pentazenschichten wie auch das Wachstum von Pentazen auf organischen dielektrischen Schichten untersucht. Außerdem wurde das Phasenverhalten von α-Sexithiophene in Abhängigkeit von Wachstumsparametern untersucht.

Contents

I. Fundamentals 17

1. Crystallography and Diffraction Principles 19
1.1. The Direct Lattice . . . 19
1.2. The Reciprocal Lattice . . . 21
1.3. Interaction of X-rays with Matter . . . 22
1.4. Position of the Diffraction Maxima . . . 23
1.4.1. The Laue Conditions . . . 25
1.4.2. The Interference Function . . . 25
1.4.3. The Scattering Vector . . . 26
1.4.4. The Scattering Process in Direct Space . . . 26
1.5. Bragg Peak Positions and Translation Lattice . . . 27
1.6. The Intensities of Bragg Peaks . . . 28
1.6.1. The Electron Density as Fourier Series . . . 28
1.6.2. The Phase Problem . . . 29

2. Experimental Details 33
2.1. Experiments with Polycrystalline Materials . . . 33
2.1.1. Single Crystals . . . 33
2.1.2. Powder . . . 33
2.1.3. Two-Dimensional Powder . . . 34
2.2. Coordinate Systems . . . 34
2.2.1. Sample System . . . 36
2.2.2. The Laboratory System . . . 39
2.2.3. The Crystal Coordinate System . . . 39
2.3. Calibration of a One-Dimensional Detector . . . 39
2.4. Reciprocal Space Maps . . . 41
2.5. Co-Planar Experiments . . . 42
2.5.1. The $\theta/2\theta$-Experiment . . . 42
2.5.2. Rocking Curves . . . 42
2.5.3. Co-Planar Scans with a One Dimensional Detector . . . 43
2.6. Grazing Incidence Diffraction . . . 46
2.6.1. Transformation Equations for Different Goniometer Geometries 47
2.7. Intensity Correction . . . 53
2.7.1. Correction Factors in the Sample Coordinate System . . . 53

2.7.2. Magnitude of Correction Factors 55

3. PyGid **59**
3.1. Simulation of Bragg Peak Positions 59
3.1.1. Examples for Indexation 61
3.2. Regridding 64
3.3. Correction for Attenuator 68
3.4. Correction for Monitor 68
3.5. Extraction of Line Scans 70
3.6. Error on Intensity Data 70

II. Results **71**

4. Structure Solution of Thin Film Phases **73**
4.1. Test Case Pentacene 74
4.1.1. Indexation 74
4.1.2. Extraction of Intensities 74
4.1.3. Correction of Intensities 77
4.1.4. Structure Optimization 77
4.1.5. Check Solution 77
4.1.6. Comparison to Literature Structures 80
4.2. Structure Solution of Pentacene Quinone on Silicon Oxide 81
4.3. Structure Solution of Perfluoropentacene on Graphite 85
4.4. Conclusion 89

5. Pentacene on Organic Dielectrics **91**
5.1. Abstract 91
5.2. Introduction 92
5.3. Experimental Details 92
5.3.1. Organic Dielectrics 92
5.3.2. Pentacene Deposition 93
5.3.3. Investigation Techniques 94
5.4. Experimental Results 95
5.4.1. Pentacene on Parylene-C 95
5.4.2. Pentacene on PBHND 97
5.4.3. Pentacene on T-SC/SA 98
5.5. Discussion 98
5.6. Conclusion 100
5.7. Acknowledgment 100
5.8. Supporting Informtaion 100

6. Temperature Stability of Pentacene Thin-Films **103**
6.1. Abstract 103

6.2. Introduction 103
6.3. Experimental Details 105
6.4. Results and Discussion 105
6.5. Conclusion 109
6.6. Acknowledgement 109
6.7. Supplementary Material 110
6.8. Not Published Information 111
6.8.1. Unit Cell Determination 111

7. Rate dependent phase behavior of α-sexithiophene 113
7.1. Abstract 113
7.2. Introduction 113
7.3. Experimental Details 114
7.4. Experimental Results 115
7.5. Discussion 119

III. Appendix 131

A. Fourier Synthesis of Electron Density 133

Part I.

Fundamentals

1. Crystallography and Diffraction Principles

A large part of solids is characterized by a periodic arrangement of atoms on a microscopic scale, resulting in both periodic and anisotropic physical behavior. For example mechanical, electrical and optical properties depend on the crystal structure of the material in question.

Crystallography deals with the description of these systems by reducing them to a repetitive element, sufficient for the description of physical properties. Conclusions can even be drawn without regarding the actual material (i.e. the type of molecules or atoms) but by merely taking the specific crystal structure into account. Please note that it is also of vital importance to consider defects in crystals because they have a significant influence on the physical properties.

In the following sections, the basic elements of crystallography will be introduced following the textbooks by Schwarzenbach (1993) and by Luger (1980). The introduction on the basics of X-ray diffraction is based on the book of Birkholz (2006) and the one of Weißmantel and Hamann (1995).

1.1. The Direct Lattice

Periodicity on microscopic scales means that a specific motif, composed of physical objects (as atoms or molecules), is repeated regularly in space. Therefore such systems are fully described by their *translational lattice*. In three-dimensional space translations in 3 directions are possible.

$$\mathbf{r}_{uvw} = u\mathbf{a} + v\mathbf{b} + w\mathbf{c}, \qquad \text{with}\, u, v \;\text{ and }\; w\, \text{integers.} \tag{1.1}$$

The *lattice vectors* $\mathbf{a}, \mathbf{b}$ and $\mathbf{c}$ are the - in general oblique - base of the translation lattice and all lattice points are linear combinations as given in Eq. (1.1). This lattice base is also called unit cell and is a parallelepiped with volume $V = (\mathbf{a} \times \mathbf{b})\mathbf{c}$. In crystallography, usually not the vectors, but their magnitudes in combination with the mutual angles are used. Therefore, the six *unit cell parameters* are:

$$\boxed{\begin{array}{ll} a, & \alpha = \angle(\mathbf{b}, \mathbf{c}) \\ b, & \beta = \angle(\mathbf{a}, \mathbf{c}) \\ c, & \gamma = \angle(\mathbf{a}, \mathbf{b}) \end{array}}$$

Table 1.1.: Notation of points, lines and planes in a lattice

uvw	a single lattice point
x_f, y_f, z_f	fractional coordinates $0 \leq x_f, y_f, z_f < 1$
$[uvw]$	specific lattice direction (or lattice line)
$\langle uvw \rangle$	all equivalent lattice lines
(hkl)	one single lattice plane (Miller indices)
$\{hkl\}$	all equivalent lattice planes
hkl	a diffraction maximum (Laue indices)

Positions within a unit cell are described relative to the corresponding lattice point (u, v, w) by fractional coordinates (x_f, y_f, z_f):

$$\mathbf{r}_{uvw,x_f y_f z_f} = \mathbf{r}_{uvw} + \mathbf{r}_{x_f y_f z_f} = (u+x_f)\mathbf{a} + (v+y_f)\mathbf{b} + (w+z_f)\mathbf{c} \qquad \text{with } 0 \leq x_f, y_f, z_f < 1 \tag{1.2}$$

A very important concept in X-ray diffraction are the *Miller indices*. Lattice points are referred to by their coordinates (u, v, w) whereas lattice planes are denoted by their Miller indices. A plane can be described by the following equation:

$$\frac{u}{m} + \frac{v}{n} + \frac{w}{p} = 1. \tag{1.3}$$

Here (u, v, w) are coordinates of points in the plane, and (m, n, p) are the intersections of the plane with the axes of the corresponding base. The ratio of the axis intersections $m : n : p$ is for parallel planes the same (a family of lattice planes) and it follows that m_N, n_N and p_N are integral multiples of m, n and p. Hence

$$\frac{u_N}{m_N} + \frac{v_N}{n_N} + \frac{w_N}{p_N} = 1, \tag{1.4}$$

$$\frac{u_N}{m} + \frac{v_N}{n} + \frac{w_N}{p} = M. \tag{1.5}$$

For practical purposes, not m, n and p but

$$h = C/m \tag{1.6}$$

$$k = C/n \tag{1.7}$$

$$l = C/p \tag{1.8}$$

are used where C is the least common multiple of m, n, p. h, k, l are the *Miller Indices*. They are integers and equal for all parallel lattice planes.

The notation listed in Tab. 1.1 is used in crystallography by convention and will be used in this work as well.

1.2. The Reciprocal Lattice

The reciprocal lattice is an important concept of crystallography especially crucial for the description of X-ray diffraction experiments. The reciprocal lattice is - like the direct one - an oblique translational lattice and its unit cell vectors are defined via

$$\mathbf{a}^* = 2\pi \frac{\mathbf{b} \times \mathbf{c}}{\mathbf{a}(\mathbf{b} \times \mathbf{c})}, \tag{1.9}$$

$$\mathbf{b}^* = 2\pi \frac{\mathbf{c} \times \mathbf{a}}{\mathbf{a}(\mathbf{b} \times \mathbf{c})}, \tag{1.10}$$

$$\mathbf{c}^* = 2\pi \frac{\mathbf{a} \times \mathbf{b}}{\mathbf{a}(\mathbf{b} \times \mathbf{c})}. \tag{1.11}$$

The angles α^*, β^* and γ^* are defined in analogy to the direct lattice (page 19).

Using trigonometric functions the vector equations (1.9)-(1.11) can also be expressed by the six scalar lattice parameters (Krischner and Koppelhuber-Bitschnau; 1994):

$$V = abc \cdot \sqrt{1 - \cos\alpha^2 - \cos\beta^2 - \cos\gamma^2 + 2\cos\alpha\cos\beta\cos\gamma} \tag{1.12}$$

$$a^* = 2\pi \cdot bc \cdot sin\alpha/V \tag{1.13}$$

$$b^* = 2\pi \cdot ca \cdot sin\beta/V \tag{1.14}$$

$$c^* = 2\pi \cdot ba \cdot sin\gamma/V \tag{1.15}$$

$$\cos\alpha^* = \frac{\cos\beta\cos\gamma - \cos\alpha}{\sin\beta\sin\gamma} \tag{1.16}$$

$$\cos\beta^* = \frac{\cos\gamma\cos\alpha - \cos\beta}{\sin\gamma\sin\alpha} \tag{1.17}$$

$$\cos\gamma^* = \frac{\cos\alpha\cos\beta - \cos\gamma}{\sin\alpha\sin\beta} \tag{1.18}$$

By interchanging $\mathbf{a}^*$ with $\mathbf{a}$, $\mathbf{b}^*$ with $\mathbf{b}$ etc., the back-transformation from the reciprocal to the direct lattice parameters is obtained.

All reciprocal lattice vectors $\mathbf{h}$ are

$$\mathbf{h} = h\mathbf{a}^* + k\mathbf{b}^* + l\mathbf{c}^* \qquad \text{with}\, h, k, l\, \text{integers.} \tag{1.19}$$

Directly from the definition of the reciprocal lattice it follows:

$$\begin{array}{lll} \mathbf{aa}^* = 2\pi & \mathbf{ab}^* = 0 & \mathbf{ac}^* = 0 \\ \mathbf{ba}^* = 0 & \mathbf{bb}^* = 2\pi & \mathbf{bc}^* = 0 \\ \mathbf{ca}^* = 0 & \mathbf{cb}^* = 0 & \mathbf{cc}^* = 2\pi \end{array} \tag{1.20}$$

Finally, two important relations between direct lattice planes and reciprocal lattice vectors are introduced (Weißmantel and Hamann; 1995, p.140f).

1. *Reciprocal lattice vectors with coordinates h, k, l are perpendicular to the direct lattice plane (h, k, l).*

   Assuming a lattice plane which intersects the axes at: $m\mathbf{a}, n\mathbf{b}, p\mathbf{c}$, three vectors in this plane are found as

   $$\mathbf{r}_1 = m\mathbf{a} - n\mathbf{b}, \quad \mathbf{r}_2 = p\mathbf{c} - m\mathbf{a}, \quad \mathbf{r}_3 = n\mathbf{b} - p\mathbf{c}$$

   Scalar products of these vectors with $\mathbf{h} = n(h\mathbf{a}^* + k\mathbf{b}^* + l\mathbf{c}^*)$ yield (consider Eq. (1.20)):

   $$\mathbf{r}_1\mathbf{h} = 2\pi(mh - nk) \overset{(1.6)}{=} 2\pi(m\frac{C}{m} - n\frac{C}{n}) = 0;$$

   $\mathbf{r}_2\mathbf{h} = 0$ and $\mathbf{r}_3\mathbf{h} = 0$ follow analogously. Hence the reciprocal lattice vector $\mathbf{h}$ is perpendicular to the direct lattice plane. It also follows that every direct lattice plane is represented as a lattice point in the reciprocal lattice.

2. *The distance of equivalent lattice planes is proportional to the length of the corresponding reciprocal lattice vector*

   $$d_{hkl} = \frac{2\pi}{|\mathbf{h}_{hkl}|}. \tag{1.21}$$

   One possiblity of representing a plane is

   $$\mathbf{r}_{uvw} \cdot \mathbf{e}_\mathbf{n} = d_{hkl}.$$

   $\mathbf{r}_{uvw}$ points to a lattice point contained in the lattice plane, $\mathbf{e}_\mathbf{n}$ is a unit vector perpendicular to this plane and d_{hkl} the distance to the origin. With $\mathbf{e}_\mathbf{n} = \frac{\mathbf{h}}{|\mathbf{h}|}$ and Eq. (1.19) equation (1.21) follows immediately.

1.3. Interaction of X-rays with Matter

On interaction of an X-ray beam with matter, three basic processes - divided into elastic and inelastic ones - occur. Inelastic processes cause Compton- and photo-electron emission. Both processes are not significant for structure investigations considered here.

For this task the elastic part, stemming from electrons performing forced oscillations with the same frequency as the incoming radiation, is used. Due to the acceleration the charges emit dipole radiation of the same wavelength as the incoming radiation. For this reason, such interaction is called *elastic scattering*. If a fixed relation between the phase of incoming and scattered wave exists this process is called *coherent elastic scattering*.

For specifying the radiation commonly the wave number

$$|\mathbf{k}| := \frac{2\pi}{\lambda} = \frac{\omega}{c} \tag{1.22}$$

is used instead of the wavelength. Multiplying this number by the unit vector $\mathbf{s}$ of the propagation direction leads to the wave vector

$$\mathbf{k} := |\mathbf{k}|\mathbf{s} = \frac{2\pi}{\lambda}\mathbf{s}. \tag{1.23}$$

The only quantity which changes during the scattering process is the direction of the momentum. The conservation of the magnitude of momentum ($\mathbf{p} = \hbar\mathbf{k}$) is expressed by

$$|\mathbf{k}_0| = |\mathbf{k}|, \tag{1.24}$$

where $\mathbf{k}_0$ is the primary and $\mathbf{k}$ the scattered wave.

1.4. Position of the Diffraction Maxima

Through interaction with the primary beam every electron in a crystal becomes the origin of a spherical wave.[1] The diffraction pattern is the result of the superposition of all these secondary waves at specific test points where the diffraction pattern is recorded.

The electric field of a spherical wave is given by

$$\mathbf{E}(\mathbf{r}) = C(\hat{\mathbf{r}})\mathbf{E}(\hat{\mathbf{r}})\frac{\exp(i\mathbf{k}(\mathbf{r}-\hat{\mathbf{r}}))}{r}, \tag{1.25}$$

where $\mathbf{E}(\hat{\mathbf{r}})$ is the electric field vector at the position of the scattering center. By choosing the origin of the coordinate system inside the crystal, $|\hat{\mathbf{r}}|$ is in the order of magnitude of inter atomic distances. Therefore, $|\mathbf{r}-\hat{\mathbf{r}}| >> |\hat{\mathbf{r}}|$ and so $\mathbf{r}-\hat{\mathbf{r}}$ can be approximated by $\mathbf{r}$. On addition to this approximation, spherical waves can be substituted by plane waves if the sample to test point distance is large

$$\mathbf{E}(\mathbf{r}) = \mathbf{A}(\hat{\mathbf{r}})\exp\{i(\mathbf{k}\mathbf{r}-\omega t)\}\cdot\exp(i\phi). \tag{1.26}$$

The new (phase)factor $\exp(i\phi)$ accounts for the path difference Δl of two X-rays of wavelength λ and leads to interference. Hence, $\mathbf{E}(\mathbf{r})$ is the electrical field of two interfering X-rays at the measurement point. The phase difference of two beams is obtained by (see Fig. 1.1)

$$\begin{aligned} \phi &= 2\pi\frac{\Delta l}{\lambda} \\ &= \frac{2\pi}{\lambda}\underbrace{(\mathbf{s}'-\mathbf{s})\hat{\mathbf{r}}}_{\Delta l}. \end{aligned} \tag{1.27}$$

And with equation (1.23) it follows

$$\phi = (\mathbf{k}-\mathbf{k}_0)\hat{\mathbf{r}} = \mathbf{q}\cdot\hat{\mathbf{r}} \tag{1.28}$$

In the last step the *scattering vector* $\mathbf{q} := \mathbf{k}-\mathbf{k}_0$ was introduced. It will be shown below that this physical quantity is of central importance in X-ray scattering.

[1] Strictly this is only true for non-polarized primary radiation. If polarized radiation - e.g. at a synchrotron - is used, it has to be taken into account that each electron emits dipole radiation.

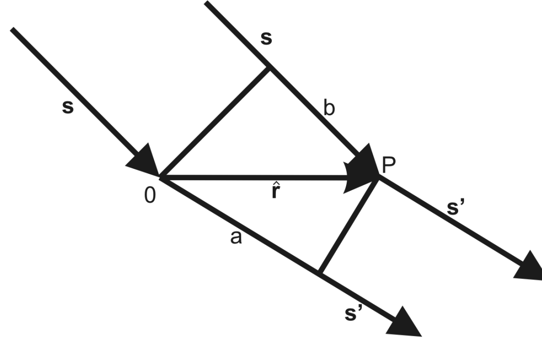

Figure 1.1.: The phase difference expressed by the path difference of two interfering X-rays. The path difference between the scattered waves is $\Delta l = a - b = \hat{\mathbf{r}}\mathbf{s}' - \hat{\mathbf{r}}\mathbf{s} = \hat{\mathbf{r}}(\mathbf{s}' - \mathbf{s})$

Relation (1.26) together with (1.28) holds for a scattering process from two scattering centers. To calculate the electric field stemming from a solid body, an integration over the whole volume of the crystal has to be performed

$$\mathbf{E}(\mathbf{r}) = \int_V d^3\hat{\mathbf{r}}\mathbf{A}(\hat{\mathbf{r}}) \exp\{i(\mathbf{kr} + \mathbf{q}\hat{\mathbf{r}})\}. \tag{1.29}$$

$\mathbf{A}(\hat{\mathbf{r}})$ is the amplitude of the scattered wave and depends on the atom where scattering takes place. Typically, a discrete set of scattering centers (atoms) located inside the unit cell is of interest. Therefore the vector $\hat{\mathbf{r}}$ for the position of one specific atom located at $(uvw, x_f y_f z_f)$ gets

$$\hat{\mathbf{r}} = \mathbf{r}_{uvw} + \mathbf{r}_{x_f y_f z_f} = (u + x_f)\mathbf{a} + (v + y_f)\mathbf{b} + (w + z_f)\mathbf{c}. \tag{1.30}$$

Thus the integration can be changed to a summation over all lattice points uvw and atoms j inside the unit cell

$$\begin{aligned}
\mathbf{E}(\mathbf{r}) &= \sum_{u,v,w} \sum_j \mathbf{A}(\mathbf{r}_{x_f y_f z_f,j}) \exp\{i(\mathbf{kr} + \mathbf{q}\mathbf{r}_{uvw} + \mathbf{q}\mathbf{r}_{x_f y_f z_f,j})\} \qquad (1.31)\\
&= \exp(i\mathbf{kr}) \underbrace{\sum_j \mathbf{A}(\mathbf{r}_{x_f y_f z_f,j}) \exp(i\mathbf{q}\mathbf{r}_{x_f y_f z_f,j})}_{F(\mathbf{q})} \cdot \sum_{u,v,w} \exp\{i\mathbf{q}(u\mathbf{a} + v\mathbf{b} + w\mathbf{c})\}\\
&= F(\mathbf{q}) \exp(i\mathbf{kr}) \sum_u \exp\{iu(\mathbf{aq})\} \cdot \sum_v \exp\{iv(\mathbf{bq})\}\\
&\quad \cdot \sum_w \exp\{iw(\mathbf{cq})\}.
\end{aligned}$$

$F(\mathbf{q})$ is called the *structure factor*. Details are found in Sec. 1.6.

1.4.1. The Laue Conditions

From equation (1.31) it can be seen that a single phase shift depends on the scalar product of a direct lattice vector with the scattering vector $\mathbf{q}$. It can be seen that maxima are observed if the equations

$$\begin{aligned} \mathbf{aq} &= 2\pi\hat{h}, \\ \mathbf{bq} &= 2\pi\hat{k}, \\ \mathbf{cq} &= 2\pi\hat{l}, \end{aligned} \tag{1.32}$$

are fulfilled simultaneously, with the Laue indices, $\hat{h}, \hat{k}$ and $\hat{l}$ taking integer values between $-\infty$ and ∞.

The relations (1.32) are known as *Laue conditions*. From the equations (1.20) and (1.19) it follows that the Laue conditions are simultaneously fulfilled if the scattering vector equals a reciprocal lattice vector

$$\mathbf{q} = \mathbf{h}.$$

Here, it becomes clear why the reciprocal lattice is important for the description of X-ray scattering.

It has to be noted that the relation

$$n \cdot (h, k, l) = \hat{h}, \hat{k}, \hat{l}$$

holds between Laue and Miller indices. If $n > 1$, the triplet $\hat{h}, \hat{k}, \hat{l}$ corresponds to a higher order diffraction maximum from the lattice plane (hkl). Please note that in the following Laue indices will be written without the hat. But to distinguish, Miller indices are written in parentheses and Laue indices are not (Tab. 1.1).

1.4.2. The Interference Function

To gain better understanding of the above sums (Eq. (1.31)) they are further evaluated by applying the formula of the geometric sum (Birkholz; 2006, p.7). To get an expression for the intensity - the measurable quantity - the evaluated sums are multiplied by their complex conjugate. The resultant expression reads

$$I(\mathbf{q}) = |F(\mathbf{q})|^2 \underbrace{\frac{\sin^2(N_1\mathbf{aq}/2)}{\sin^2(\mathbf{aq}/2)} \cdot \frac{\sin^2(N_2\mathbf{bq}/2)}{\sin^2(\mathbf{bq}/2)} \cdot \frac{\sin^2(N_3\mathbf{cq}/2)}{\sin^2(\mathbf{cq}/2)}}_{\text{Interference function}}. \tag{1.33}$$

The last three terms of this equation are known as the interference function. This function differs significantly from zero only if the argument of the sine-function in the denominator becomes an integral multiple of π which is equivalent to fulfilling the Laue conditions. An exemplary graph of the interference function is plotted in Fig. 1.2.

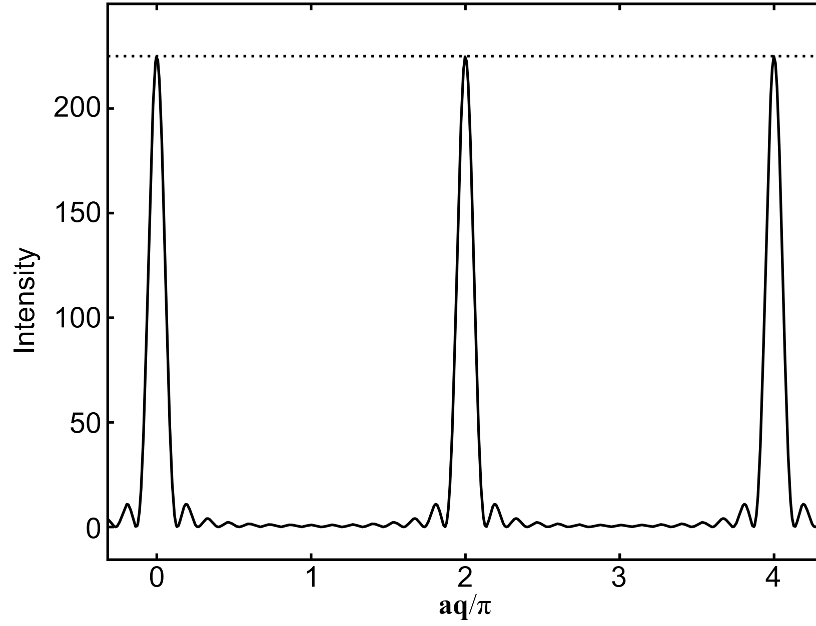

Figure 1.2.: The interference function for a one-dimensional lattice $I(\mathbf{q}) = \frac{\sin^2(N\mathbf{aq}/2)}{\sin^2(\mathbf{aq}/2)}$, for $\mathbf{a} = 1$ and $N = 15$. It can be seen that maxima of intensity are observed if the product $\mathbf{aq}$ becomes an integral multiple of 2π. The maximum intensity is determined by $N^2 = 225$ and plotted as a dotted line.

1.4.3. The Scattering Vector

The scattering vector $\mathbf{q}$ has already been introduced above (Eq. (1.28)). The magnitude of this vector can be calculated from the scattering angle and the used wavelength. Considering elastic scattering ($|\mathbf{k}| = |\mathbf{k}_0| = \frac{2\pi}{\lambda}$) it can be derived as

$$\begin{aligned} |\mathbf{q}| &= \sqrt{(\mathbf{k}-\mathbf{k}_0)^2} \\ &= \sqrt{\mathbf{k}^2 - 2\mathbf{k}_0\mathbf{k} + \mathbf{k}_0^2} \\ &= \tfrac{2\pi}{\lambda}\sqrt{2 - 2\cos 2\theta} \quad \Big|\cdot\tfrac{2}{2} \\ &= \tfrac{4\pi}{\lambda}\underbrace{\sqrt{\frac{1-\cos 2\theta}{2}}}_{\sin\theta} = \tfrac{4\pi}{\lambda}\sin\theta, \end{aligned} \tag{1.34}$$

where 2θ is the angle enclosed by the wave vectors of the primary and scattered beam.

1.4.4. The Scattering Process in Direct Space

It has already been shown that the Laue equations (1.32) are fulfilled if the scattering vector coincides with a reciprocal lattice vector.

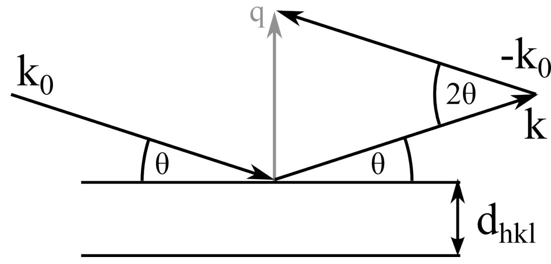

Figure 1.3.: Scattering geometry at an arbitrary lattice plane

In section 1.2 it is shown that every reciprocal lattice vector is perpendicular to a specific set of direct lattice planes and that the distance between these lattice planes d_{hkl} is given by

$$d_{hkl} = n\frac{2\pi}{|\mathbf{q}_n|},$$

where the different orders of diffraction are considered by the factor n.

By substituting that for the left hand side in equation (1.34) the *Bragg Equation*

$$n\lambda = 2d_{hkl}\sin\theta \tag{1.35}$$

is derived.

From the elastic nature of the process and the fact that the scattering vector is perpendicular to the lattice plane it follows that the incidence angle θ and the exit angle have to have the same value (Fig. 1.3) to observe a Bragg peak.

The *Bragg equation* and this *symmetry condition* are implications of the Laue conditions and it can be concluded that a diffraction maximum is observed if both criteria are simultaneously met by the experimental settings.

1.5. Bragg Peak Positions and Translation Lattice

The interference function (Eq. (1.33)) expresses that the observed intensity pattern is a function of the scattering vector and the lattice parameters $\mathbf{a}, \mathbf{b}$ and $\mathbf{c}$. Therefore it is clear that the positions of the Bragg peaks depend only on the translational lattice and the motif does not have to be taken into account. Furthermore to each Bragg peak a reciprocal lattice vector can be assigned. So a scattering experiment yields a set of Bragg peaks and the corresponding reciprocal lattice vectors. The matching translational lattice is found by determining a base $\mathbf{a}^*, \mathbf{b}^*, \mathbf{c}^*$ which describes all these vectors by integer coordinates.

1.6. The Intensities of Bragg Peaks

The *structure factor* was already introduced above for point charges inside the unit cell. In the following it is derived for more realistic cases. The electron density ρ_e of the atoms is taken into account by introducing the *atomic form factor* f

$$f = \int_{at} \rho_e(\mathbf{r}') \exp(-i\mathbf{q}\mathbf{r}') d\mathbf{r}'. \tag{1.36}$$

The structure factor F is defined by taking the electron density (ρ_e) of the whole unit cell into account

$$\begin{aligned} F &= \int\limits_{UC} \rho_e(\mathbf{r}') \exp(-i\mathbf{q}\mathbf{r}') d\mathbf{r}' & (1.37) \\ &= \sum_{n=1}^{N} \int_{at} \rho_e(\mathbf{r}') \exp(-i\mathbf{q}(\mathbf{r}' - \mathbf{r}_{x_f y_f z_f,n})) d\mathbf{r}' & (1.38) \\ &= \sum_{n=1}^{N} f_n(\mathbf{q}) \exp(i\mathbf{q}\mathbf{r}_{x_f y_f z_f,n}). & (1.39) \end{aligned}$$

In the second and third step, the expression for the atomic form factor (Eq. (1.36)) was inserted into the structure factor equation. Hence the integration was reduced to a summation over the form factors of the atoms f_n at the discrete positions $\mathbf{r}_{x_f y_f z_f,n}$ inside the unit cell.

From the interference function (Eq. 1.33) it is seen that intensity can only be observed if the vector $\mathbf{q}$ corresponds to a reciprocal lattice vector $\mathbf{h}$. Hence, it is only necessary to calculate the structure factor for these scattering vectors

$$\begin{aligned} \mathbf{h}\mathbf{r}_{x_f y_f z_f} &= (h\mathbf{a}^* + k\mathbf{b}^* + l\mathbf{c}^*)(x_f\mathbf{a} + y_f\mathbf{b} + z_f\mathbf{c}) \\ &= 2\pi(hx_f + ky_f + lz_f). \end{aligned} \tag{1.40}$$

Substituting this expression into Eq. (1.37) yields

$$\begin{aligned} F(hkl) &= \sum_{n=1}^{N} f_n(\mathbf{h}) \exp(2\pi i(hx_{f,n} + ky_{f,n} + lz_{f,n}) & (1.41) \\ &= \sum_{n=1}^{N} f_n(\mathbf{h}) \exp(2\pi i \cdot \mathbf{h}\mathbf{r}_{x_f y_f z_f,n}). & (1.42) \end{aligned}$$

1.6.1. The Electron Density as Fourier Series

Eq. (1.37) expresses that the structure factor is the Fourier transform of the electron density within the unit cell. The position vector is now again expressed via the fractional coordinates $(x_f, y_f z_f)$ and the volume element $d\mathbf{r} \equiv dV$ is expressed by

an infinitesimal parallelepiped built from the three base vectors of the direct lattice $dV = d\mathbf{a}[d\mathbf{b} \times d\mathbf{c}] = \mathbf{a}[\mathbf{b} \times \mathbf{c}]dx_f dy_f dz_f = V dx_f dy_f dz_f$. Hence it follows

$$F(hkl) = V \int_{UC} \rho_e(x_f, y_f, z_f) e^{-2\pi i(hx_f + ky_f + lz_f)} dxdydz, \quad (1.43)$$

and the electron density ρ_e is therefore the inverse Fourier transform with the structure factors as amplitudes. Due to the fact that h, k and l are only integers the integral can be expressed as a triple sum over all possible values for the Laue indices

$$\rho_e(x_f, y_f, z_f) = \frac{1}{V} \sum_{h=-\infty}^{\infty} \sum_{k=-\infty}^{\infty} \sum_{l=-\infty}^{\infty} F(hkl) e^{2\pi i(hx_f + ky_f + lz_f)}. \quad (1.44)$$

This representation can be derived intuitively by developing the periodic function $\rho_e(x_f, y_f, z_f)$ into a Fourier series and inserting this series into Eq. (1.43) or formally from Fourier transform theory (Bennett; 2010; Shmueli; 2007).

The representation of the electron density as a Fourier series leads to fundamental interpretations:

1. The intensity of each Bragg peak represents the squared amplitude of a plane wave which interpolates the electron density. Hence, strong peaks indicate the frequency and direction of strong electron density variations.

2. Plane waves contain only information about the electron density in the direction of the wave vector and no lateral one.

3. Higher $\mathbf{q}$-reflections correspond to higher frequencies and hence are sensitive to electron density details on a smaller scale.

Some more details about the Fourier series representations and illustrations are found in Appendix A.

1.6.2. The Phase Problem

It follows from above that the structure factor is a complex quantity and hence consists of a real and imaginary part

$$F(\mathbf{h}) = A(\mathbf{h}) + iB(\mathbf{h}). \quad (1.45)$$

Writing a complex number as vector in the complex plane it can also be expressed via its amplitude and the angle the vector encloses with the positive $\mathbf{e}_x$-axis. Hence

$$\begin{aligned} A(\mathbf{h}) &= |F(\mathbf{h})| \cos(\varphi(\mathbf{h})), \\ B(\mathbf{h}) &= |F(\mathbf{h})| \sin(\varphi(\mathbf{h})), \end{aligned} \quad (1.46)$$

and therefore

$$F(\mathbf{h}) = |F(\mathbf{h})|(\cos(\varphi(\mathbf{h})) + i \sin(\varphi(\mathbf{h}))) = |F(\mathbf{h})| \exp(i\varphi(\mathbf{h})). \quad (1.47)$$

Considering that the intensity - the quantity observed in an X-ray experiment - is proportional to the squared magnitude of F

$$I \propto |F|^2 = FF^* = |F|^2 \underbrace{\exp(i\varphi(\mathbf{h}))\exp(-i\varphi(\mathbf{h}))}_{\equiv 1},$$

it is obvious that the phase is not measured in an X-ray experiment. Therefore an inverse Fourier transformation is not possible to obtain the electron density. This fact is known as the phase problem. Through the years several methods for retrieving the phase information or circumventing the phase problem have been developed.

Patterson Method

Patterson (1934) developed a first systematic approach to structure determination. Starting point for this method is the fact that, while the structure factors depend on the positions of the atoms within the unit cell, the relative intensities depend on the differences of these vectors. This is demonstrated by following Shmueli (2007)

$$\begin{aligned} I(\mathbf{h}) &\propto |F(\mathbf{h})|^2 && (1.48)\\ &= F(\mathbf{h})F^*(\mathbf{h}) && (1.49)\\ &= \sum_j \sum_k f_j f_k \exp[2\pi i \mathbf{h} \cdot (\mathbf{r_j} - \mathbf{r_k})]. && (1.50) \end{aligned}$$

A Fourier transformation of the squared structure factor yields the autocorrelation function of the electron density with the correlation vector $\mathbf{u}$; i.e. $\mathbf{u}$ represents an inter atomic distance (Shmueli; 2007)

$$\begin{aligned} P(\mathbf{u}) &= \frac{1}{V}\sum_{\mathbf{h}} |F(\mathbf{h})|^2 \exp(-2\pi i \mathbf{h} \cdot \mathbf{u}) && (1.51)\\ &= \int_{\text{cell}} \rho(\mathbf{r})\rho(\mathbf{r}+\mathbf{u}) d^3\mathbf{r}. && (1.52) \end{aligned}$$

Eq. (1.51) is the Patterson function which is the basis for the Patterson Method. It has the following properties:

- It has the same periodicity as the electron density and hence both can be described by the same unit cell. But, while N atomic peaks are observed for the electron density $\rho_e(\mathbf{r})$, N^2 peaks are observed for the Patterson function. Therefore the unit cell can be quite crowded by Patterson peaks leading to substantial peak overlaps.

- It is always centro symmetric. This results from the fact that it depends on inter atomic distances and the corresponding scattering factors of involved atoms.

For details about the Patterson method please consult for example Shmueli (2007) or Bennett (2010). Here it is just noted that based on the Patterson function crystal

structures can be solved if heavy atoms or known fragments are present in the investigated material. While the presence of heavy atoms is not very likely in organic crystals, known fragments might be present. Molecular shapes can be calculated isolated from any crystal structure. These calculated molecular shapes are not influenced by the weak van der Waals forces, which govern molecular crystals. Thus, known fragments (e.g. intra molecular distances of atoms) are expected to be present in a molecular crystal.

To conclude, Patterson methods might be useable for structure determinations of organic thin films but have not been tested during this work.

Direct Methods

In contrast to Patterson methods, where some prior knowledge about the investigated material is essential, direct methods do not rely on prior knowledge. Therefore they might also be regarded as an ab-initio crystal structure solution procedure. The main concept of direct methods is that the phases of some structure factors can be determined; e.g. from space group considerations. Then, special sets of structure factors can be constructed and yet unknown phases predicted by probabilistic methods. The probability to find the correct crystal structure solution with direct methods is proportional to the number of measured reflexes. For structure determination on molecular single crystals typically several thousands of reflexes are used to determine around hundred parameters (fractal coordinates). Keeping in mind, that at best one to two hundred peaks can be observed from thin organic films it is obvious that this method cannot be applied to these systems.

More details about direct methods are again found in the books by Shmueli (2007) and Bennett (2010).

Direct Space Methods

Direct and Patterson methods are also known as reciprocal-space methods because they are based on structure factor amplitudes ($|F_{hkl}|$, Eq. (1.46)) measured in the X-ray experiment. Another approach is chosen by direct space methods. There, test crystal structures of the molecules are randomly sampled in direct space and the corresponding scattering pattern is calculated. This is repeated until the calculated scattering pattern fits the experimental data. Due to this approach the phase problem is circumvented, because starting from a “known” crystal structure, the scattering pattern can readily be calculated. Rietveld (1969) developed the first direct space method for powder diffraction, where it is virtually impossible to extract the required number of structure factor amplitudes necessary for direct or Patterson methods.

In essence, direct space methods are global optimization procedures of (potentially) great complexity. Because of the increase in computing power and the availability of efficient global optimization algorithms these methods have great potential today. Algorithms used are Monte Carlo search with simulated annealing or parallel tempering as well as genetic algorithms. Direct space methods can also be regarded as

a basic (brute-force) approach which can be executed with minimal input. But of course chances to find a solution increase if some prior knowledge is included, because then the complexity of the optimization problem is reduced.

During an optimization procedure a criterion to measure the quality of a test model is needed. Therefore a cost function, depending on the optimized parameters is introduced and minimized during the optimization. For powder diffraction for example, the χ^2-misfit between a calculated powder pattern and the experimentally observed one is frequently used. If structure factor amplitudes can be extracted the χ^2-misfit between observed (F_{obs}) and calculated structure factors (F_{calc}) can be used

$$\chi^2 = \sum_i \frac{(|F_{\text{obs}_i}|^2 - |F_{\text{calc}_i}|^2)^2}{\sigma^2_{F_{\text{obs}_i}}}, \tag{1.53}$$

with $\sigma_{F_{\text{obs}_i}}$ the standard deviation of the observed structure factor amplitude. Choosing this approach, one is not limited to the usage of cost functions based solely on X-ray scattering data. It is also possible to use a properly weighted sum of cost functions, e.g. one taking the X-ray data into account and a second one which considers the energy of the packing

$$C_{\text{total}} = A \cdot C_{\text{cryst}} + B \cdot C_{\text{energy}}. \tag{1.54}$$

Several software packages exist which employ direct space methods for crystal structure solutions. Please consult the paper by Favre-Nicolin and Černý (2002) for references.

For this thesis the software FOX published in the above paper was successfully used to solve surface induced phases of three different organic materials (See Chap. 4) by solely taking X-ray scattering data into account. This reveals that direct space methods have large potentials in the field of crystal structure determination of new systems.

Energy Based Optimization

As indicated above it is also possible to consider energetic calculations during a packing optimization. It is even possible to derive crystallographic structures solely by packing optimizations using an energy based cost function calculated by force field or density functional theory techniques. There are several examples of a successful application of this method (Moser et al.; 2009; Yoshida et al.; 2007; Nabok et al.; 2007; Puschnig et al.; 2003; Hummer et al.; 2003).

To determine the quality of results obtained that way, a comparison of the resulting structure factors with experimental intensities is obligatory. This step may also be used to select the proper solution from a set of solutions similar in energy. More details about this procedure are found in Chap. 4 or in one of the above papers.

2. Experimental Details

The aim of an X-ray experiment is to record the spatial distribution and intensities of X-ray diffraction peaks to gain insight into the micro structure of materials. As known from Sec. 1.4.4, Bragg reflexes are only observed at distinct positions in space when the Laue conditions are fulfilled. Especially for unknown systems it is therefore in general necessary to scan the reciprocal space over a large volume for diffraction peaks; i. e. orientation and length of the scattering vector have to be changed.

In an experiment, the reciprocal space is scanned by rotating the detector and the sample on a *goniometer* around a common center of rotation. During the scan all motor positions and the diffracted intensities are recorded. To obtain crystallographic data the scattering vectors are calculated from the recorded motorpositions.

In this chapter first the implications of specific sample properties for the experiment are discussed. Then the used coordinate systems are introduced. Subsequently possible scans and different goniometer geometries are introduced and the equations for transforming the recorded data to $\mathbf{q}$-space derived.

2.1. Experiments with Polycrystalline Materials

X-ray diffraction maxima are observed if the Laue conditions are fulfilled; i.e. if the scattering vector equals a reciprocal lattice vector. If polycrystalline samples are investigated the superposition of the reciprocal lattices of all the crystallites determines how the Laue conditions can be fulfilled. It also determines which information can be obtained from a sample with specific properties. Details for selected systems will be discussed in the following.

2.1.1. Single Crystals

A single crystal is characterized by a perfect motif arrangement. The corresponding reciprocal lattice is a set of points. To observe a Bragg reflex the scattering vector has to coincide with one of these points. This makes it necessary to change the length as well as the orientation of the scattering vector to record a specific Bragg peak (Fig. 2.1).

2.1.2. Powder

A crystalline powder consists of randomly oriented crystallites. The corresponding reciprocal lattice superposition is a set of spheres - each radius corresponding to one lattice plane distance. Hence the orientation of the scattering vector is not important any more because a fraction of crystallites will always be oriented correctly for observing a Bragg

reflex. This means, each lattice plane distance can be investigated by only changing the length of the scattering vector via changing the scattering angle 2θ (Fig. 2.2).

2.1.3. Two-Dimensional Powder

A two-dimensional powder is an intermediate case between a single crystal and a crystalline powder. Typical examples are organic thin films formed by physical vapor deposition onto isotropic surfaces. A two-dimensional powder consists of crystallites oriented with the same lattice plane parallel to a substrate surface but not showing in-plane alignment. Missing in-plane alignment means that crystallites are randomly oriented around the surface normal (Fig. 2.3(a)).

The resulting reciprocal lattice superposition is a set of rings where the radii are determined by the in-plane component of the scattering vector, $q_p = \sqrt{q_x^2 + q_y^2}$. The z-positions of the rings correspond directly to q_z.

The shape of this reciprocal lattice implies that the rotation of the sample around the surface normal does not have to be taken into account. Performing at each q_z a radial scan along q_p reveals all possible information.

Texture

Two-dimensional powder is the name given to the phenomenon outlined above. A description of two-dimensional powders is possible with the concept of *texture*. A powder of crystallites is said to have a texture if the crystallites are not oriented randomly but show some *preferred orientation*; i.e. a large fraction of the crystallites is oriented in the same way.

A texture where one degree of freedom (here the rotation around the surface normal) is present is called *fiber-texture* and the direction of preferred orientation is the *fiber axis* (Birkholz; 2006, p. 183ff). In more detail the texture is specified by giving the crystallographic plane (hkl) perpendicular onto the fiber axis. In this framework, a two-dimensional powder is characterized by a fiber axis parallel to the substrate surface normal.

In a real two-dimensional powder, it is likely to observe deviations from a very strict alignment; i.e. an onset of a three-dimensional distribution is present. This results in the observation of partial Debye-Scherrer rings in diffraction patterns.

2.2. Coordinate Systems

Frequently the relation between the microstructure of the film and the substrate properties is of interest; e.g. crystallographic orientation of the film relative to the crystallographic directions of the substrate; which lattice plane is parallel to the substrate surface. That is, one is interested in the relation between the *sample coordinate system* and the *crystal system.* As mentioned above detector and sample are positioned using a *goniometer.* The goniometer commonly operates in the *laboratory coordinate*

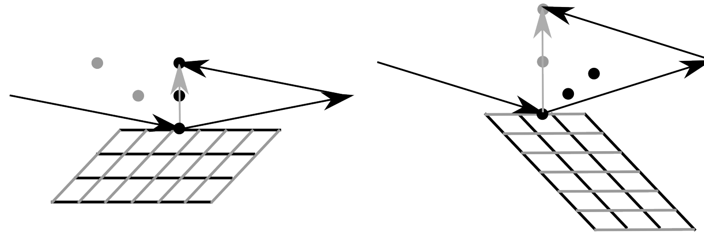

Figure 2.1.: Two sets of lattice planes of a single crystal and the corresponding reciprocal lattice. The orientation of the crystal as well as the length of the scattering vector has to be changed for recording the Bragg reflex of another family of lattice planes (Moser; 2008).

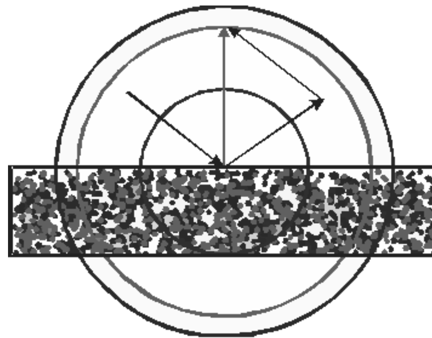

Figure 2.2.: Reciprocal lattice superposition of a crystalline powder. Only the length of the scattering vector has to be taken into account. When the tip of the scattering vector intersects a sphere (of reflection), a Bragg peak will be observed (Moser; 2008).

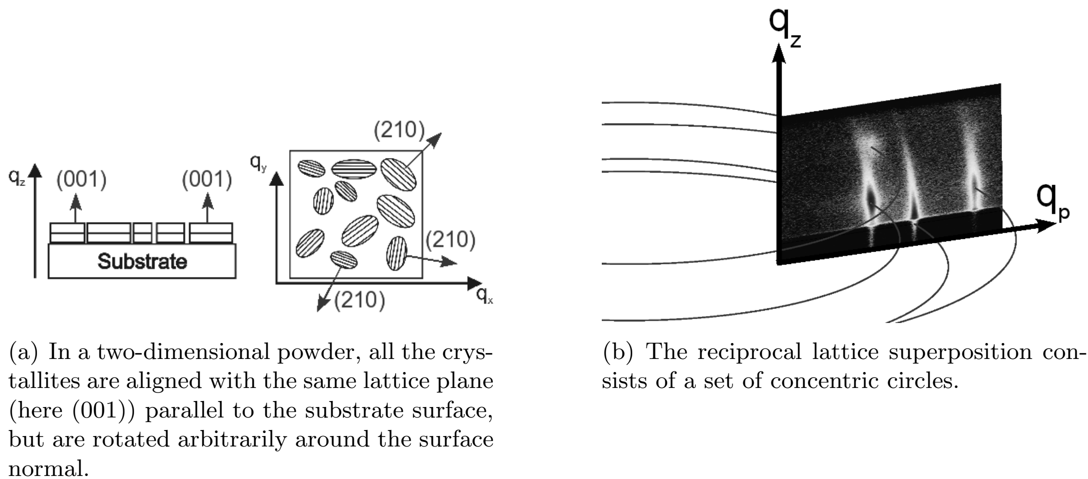

(a) In a two-dimensional powder, all the crystallites are aligned with the same lattice plane (here (001)) parallel to the substrate surface, but are rotated arbitrarily around the surface normal.

(b) The reciprocal lattice superposition consists of a set of concentric circles.

Figure 2.3.: Schematic drawing and reciprocal lattice superposition of a two-dimensional powder (Moser; 2008).

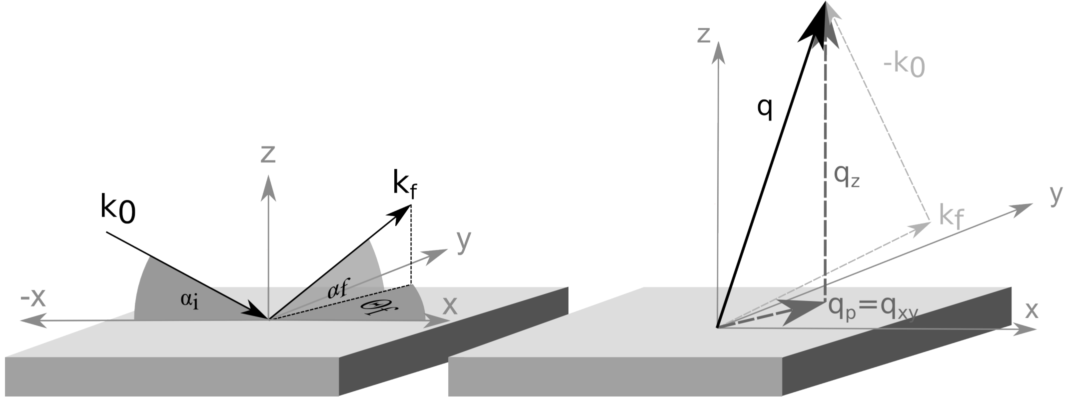

Figure 2.4.: The sample coordinate system. **Left:** The incoming $\mathbf{k_0}$ and scattered wave vector $\mathbf{k_f}$ are shown. Also the incidence angle (α_i), the in-plane (θ_f) and out-of-plane (α_f) scattering angles are indicated. **Right:** The scattering vector $\mathbf{q} = \mathbf{k_f} - \mathbf{k_0}$ and its in-plane ($q_p \equiv q_{xy}$) and out-of-plane (q_z) components are shown.

system. In this section these three coordinate systems (all right handed) are introduced. The mathematical relations between them – as significant for the experiments – will be derived in Sec. 2.5 and 2.6.1.

2.2.1. Sample System

The sample coordinate system (Fig. 2.4) is defined with the z-axis perpendicular on the sample surface. The x- and y-axis are chosen in the plane of the substrate surface. The incoming wave is contained in the (-x,z)-plane. Frequently it is possible to rotate the sample around its surface normal (rotation angle ϕ). In this case the incoming wave is contained in the (-x,z)-plane for zero ϕ-rotation. The angles of incoming and diffracted wave are (Fig. 2.4 (left)):

θ_i ... in-plane incidence angle (equals zero in Fig. 2.4 (left))
α_i ... out-of-plane incidence angle
θ_f ... in-plane scattering angle
α_f ... out-of-plane scattering angle

For two-dimensional powders the rotation of the sample around its surface normal has not to be considered (Fig. 2.3). Hence the angle θ_i will be treated as zero throughout this work.

Fig. 2.4 (right) shows the scattering vector $\mathbf{q} = \mathbf{k_f} - \mathbf{k_0}$ and defines its in-plane $q_p \equiv q_{xy}$ and out-of-plane q_z component. The components of the vectors $\mathbf{k_0}$ and $\mathbf{k_f}$ can be calculated by geometrical considerations from Fig. 2.4 (left), and the scattering

vector follows

$$\begin{aligned}
\mathbf{q} &= \mathbf{k}_f - \mathbf{k}_0 = (q_x, q_y, q_z), && (2.1)\\
q_x &= \frac{2\pi}{\lambda}(\cos\alpha_f \cos\theta_f - \cos\alpha_i), && (2.2)\\
q_y &= \frac{2\pi}{\lambda}(\cos\alpha_f \sin\theta_f), && (2.3)\\
q_z &= \frac{2\pi}{\lambda}(\sin\alpha_f + \sin\alpha_i), && (2.4)\\
q_p &= \sqrt{q_x^2 + q_y^2}. && (2.5)
\end{aligned}$$

Inverting these equations yields θ_f and α_f as function of q_p and q_z

$$\begin{aligned}
\sin(\alpha_f) &= \frac{\lambda}{2\pi} q_z - \sin\alpha_i, && (2.6)\\
\cos(\theta_f) &= \frac{(\frac{\lambda}{2\pi} q_p)^2 - \cos^2\alpha_f - \cos^2\alpha_i}{-2\cos\alpha_i \cos\alpha_f}. && (2.7)
\end{aligned}$$

From the scalar product of $\mathbf{k}_0$ and $\mathbf{k}_f$ the scattering angle 2θ can be calculated.

$$\begin{aligned}
\cos 2\theta &= \frac{\lambda^2}{4\pi^2}\mathbf{k_0 k_f} && (2.8)\\
&= \begin{pmatrix} \cos\alpha_f \cos\theta_f \\ \cos\alpha_f \sin\theta_f \\ \sin\alpha_f \end{pmatrix} \begin{pmatrix} -\cos\alpha_i \\ 0 \\ \sin\alpha_i \end{pmatrix} && (2.9)\\
&= -\cos\alpha_i \cos\alpha_f \cos\theta_f + \sin\alpha_f \sin\alpha_i && (2.10)
\end{aligned}$$

For small incidence angles this equation reduces to

$$\cos 2\theta \sim \cos\alpha_f \cos\theta_f. \qquad (2.11)$$

Rotation Matrix Formulation

The above equations (2.1)-(2.5) can be derived geometrically from Fig. 2.4, but more generally they are achieved by using rotation matrices. This formulation will ease calculations for different goniometer geometries; especially when a one-dimensional detector is used. Therefore this approach will be introduced in the following. Matrix multiplications are not commutative and their sequence of application has to be chosen to reflect the properties of the goniometer. That is, some rotation axes will change their orientation during operation and this has to be reflected in the calculations. The rotation matrices are defined such that a rotation with a positive angle rotates a vector clockwise if looking along the rotation axis (e.g. a negative angle is necessary to rotate a vector around the y-axis towards the positive z-axis).

The rotation of vector $\mathbf{k}_f$ in Fig. 2.4 (left) for example consists of a rotation θ_f around the z-axis of the sample system followed by a rotation $-\alpha_f$ around the rotated y-axis= y'-axis. The matrix for this rotation is given as:

$$\mathbf{R} = \mathbf{R_{y'}}(-\alpha_\mathbf{f})\mathbf{R_z}(\theta_\mathbf{f}). \tag{2.12}$$

With $\mathbf{R_z}$ the rotation matrix around the z-axis of the sample system and $\mathbf{R_{y'}}$ the rotation matrix around the y'-axis. The latter matrix is obtained by transforming the y-rotation matrix of the sample system according to the first z-rotation

$$\mathbf{R_{y'}}(-\alpha_f) = \mathbf{R_z}(\theta_\mathbf{f})\mathbf{R_y}(-\alpha_\mathbf{f})\mathbf{R_z}(\theta_\mathbf{f})^{-1}. \tag{2.13}$$

Substituting this expression into the above equation (2.12) yields

$$\mathbf{R} = \mathbf{R_z}(\theta_\mathbf{f})\mathbf{R_y}(-\alpha_\mathbf{f}). \tag{2.14}$$

It is seen that the matrix of the complete rotation is given as product of the basic rotation matrices (the matrices which rotate around the coordinate axes) of the starting coordinate system. The sequence of the matrices in the product is inverse to the sequence of the rotations.

For calculations one starts now with the wave vectors for all goniometer angles set to zero ($\mathbf{k_0} = \mathbf{k}_f = \frac{2\pi}{\lambda}\mathbf{e_x}$) and rotates them to their new positions. Application of this strategy in the sample coordinate system results in

$$\begin{aligned}
\mathbf{k_0} &= \frac{2\pi}{\lambda}\mathbf{R_y}(\alpha_i)\mathbf{e_x} \\
&= \frac{2\pi}{\lambda}\begin{pmatrix}\cos\alpha_i & 0 & \sin\alpha_i \\ 0 & 1 & 0 \\ -\sin\alpha_i & 0 & \cos\alpha_i\end{pmatrix}\begin{pmatrix}1\\0\\0\end{pmatrix} \\
&= \frac{2\pi}{\lambda}\begin{pmatrix}\cos\alpha_i \\ 0 \\ -\sin\alpha_i\end{pmatrix}
\end{aligned} \tag{2.15}$$

and

$$\begin{aligned}
\mathbf{k_f} &= \frac{2\pi}{\lambda}\mathbf{R_z}(\theta_\mathbf{f})\mathbf{R_y}(-\alpha_\mathbf{f})\mathbf{e_x} \\
&= \frac{2\pi}{\lambda}\begin{pmatrix}\cos\theta_f & -\sin\theta_f & 0 \\ \sin\theta_f & \cos\theta_f & 0 \\ 0 & 0 & 1\end{pmatrix}\begin{pmatrix}\cos\alpha_f & 0 & -\sin\alpha_f \\ 0 & 1 & 0 \\ \sin\alpha_f & 0 & \cos\alpha_f\end{pmatrix}\begin{pmatrix}1\\0\\0\end{pmatrix} \\
&= \frac{2\pi}{\lambda}\begin{pmatrix}\cos\alpha_f\cos\theta_f \\ \cos\alpha_f\sin\theta_f \\ \sin\alpha_f\end{pmatrix}.
\end{aligned} \tag{2.16}$$

Calculating $\mathbf{q} = \mathbf{k}_f - \mathbf{k}_0$ from this two vectors gives the same results as derived geometrically above (Eqs. (2.1)-(2.5)).

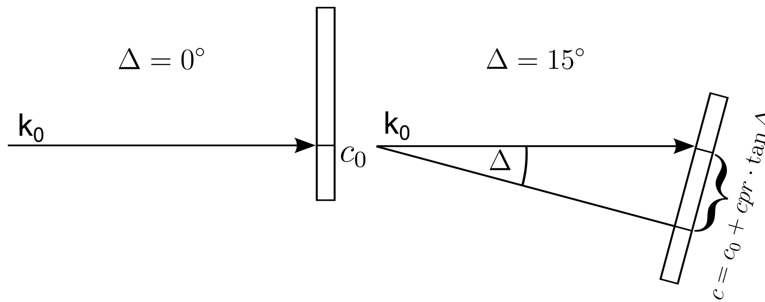

Figure 2.5.: Sketch of the detector calibration. **Left:** The detector position with all motors set to 0. At this stage the primary beam $\mathbf{k_0}$ hits the zero channel of the detector c_0. **Right:** By scanning the detector through the primary beam the two calibration parameters c_0 and cpr are obtained.

2.2.2. The Laboratory System

This is the coordinate system in which the goniometer operates. The x-axis is parallel to the primary X-ray beam, the z-axis chosen vertically, and the y-axis is perpendicular on the (x,z)-plane. The origin is located at the center of rotation of the goniometer. If all goniometer motors are set to zero all its rotation axes coincide with one of the coordinate axes of the laboratory system.

2.2.3. The Crystal Coordinate System

The direct and reciprocal lattice (Sec. 1.1 and 1.2) are vector spaces spanned by their unit cell axes. They are used to describe the crystal structure of the investigated material. According to symmetry there exist 7 crystal systems (Schwarzenbach; 1993, page 62 ff.).

In an X-ray experiment the reciprocal lattice is observed and hence this will mainly be used in this work. The Laue indices *hkl* are the (integer) coordinates. The lattice base is generally oblique and hence the coordinates (Laue indices) will be transformed to an orthogonal coordinate system to ease calculations. Most important is the transformation to the sample coordinate system because there the relation between the crystal structure of a thin film and the substrate can be studied most naturally.

2.3. Calibration of a One-Dimensional Detector

Nowadays one dimensional detectors are quite widespread. But before using them the angular resolution has to be calibrated properly. For this purpose the detector is scanned with a defined step width through the primary beam as illustrated in Fig. 2.5. This scan provides data tuples (c,Δ) (channel number, angle). The two calibration parameters *zero channel* (c_0) and *channel per rad* (cpr)[1] are obtained by a linear fit

[1]Please note that in PyGid this value is called channel per degree *cpd*.

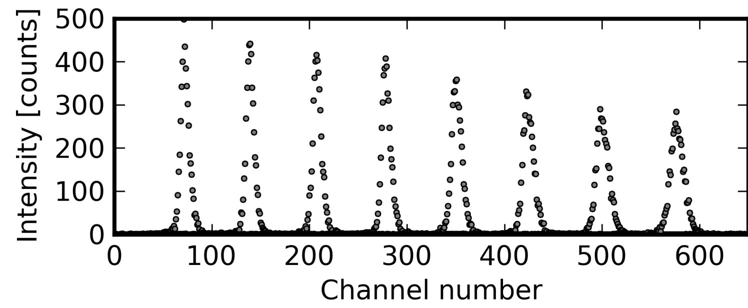

(a)

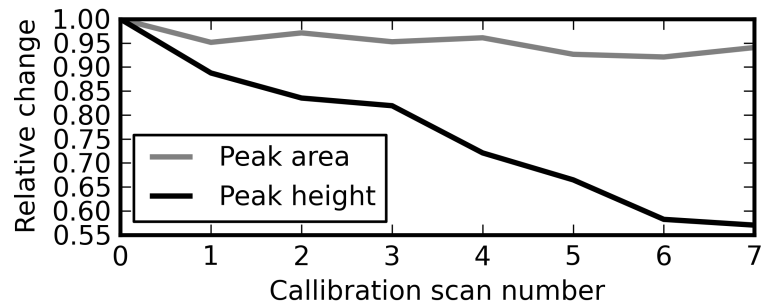

(b)

Figure 2.6.: Data of a detector calibration experiment. (a) shows the curves measured during one calibration scan with a step width of one degree. (b) shows area and height of the individual peaks. The peak height decreases by $\approx 40\%$ while the area is more or less constant.

of the equation

$$c = c_0 + cpr \cdot \tan\Delta. \quad (2.17)$$

After calibration channel numbers are transformed into (detector-)angles by applying

$$\Delta = \arctan\left(\frac{c - c_0}{cpr}\right). \quad (2.18)$$

For calibration it is not necessary to take the goniometer radius into account, because only directions of diffracted waves will be measured (i.e. vectors with fixed length $\frac{2\pi}{\lambda}$), and hence knowing the angles is sufficient.

Fig. 2.6 (a) shows the individual calibration curves where Δ was scanned from $0\ldots7°$ in one degree steps. The detector was mounted such that for $\Delta = 0°$ the lower part of the detector was hit by the primary beam (at approximately channel number 80).

The calibration experiment illustrates an important implication of one-dimensional detectors. The incidence angle of the radiation (onto the detector) changes along the detector, leading to a decrease of the peak height and an increase of the peak width. But while height and width change, the peak area is constant. This can be seen from Fig. 2.6 (b) where peak area (estimated by the sum of all data points) and peak height (estimated by the maximum of the data points) are shown. Therefore only peak areas are a proper measure for intensities obtained with a one-dimensional detector.

2.4. Reciprocal Space Maps

By using a one-dimensional detector for X-ray experiments not only one-dimensional but two-dimensional data is recorded. The best way of representing them is by means two-dimensional pseudo color plots.

From the Bragg equation (1.35) it is evident that angular positions of Bragg peaks depend on the used wavelength. Therefore different patterns will be obtained for different X-ray sources, making a comparison of the different results quite difficult. Because of that a wavelength-independent representation of the measured signals is favored.

Keeping in mind that the scattering vector corresponds to the momentum transfer in the scattering process it is clear that it is independent from the used primary beam energy and therefore independent from the used X-ray source. Hence the scattering vector ($\mathbf{q} = (q_x, q_y, q_z)$) is well suited to be used as the independent variable. Which components of the scattering-vector are meaningful depends on the nature of the investigated system; e.g. for a powder only the magnitude $|\mathbf{q}|$ while for a two-dimensional powder the q_z and the q_p component are relevant. For a single crystal all three components q_x, q_y and q_z are significant.

The representation of the experimental results in a two-dimensional plot is called *reciprocal space map*. For grazing incidence diffraction data of a two-dimensional powder this is the best representation because it is indeed a two dimensional system with coordinates q_p and q_z.

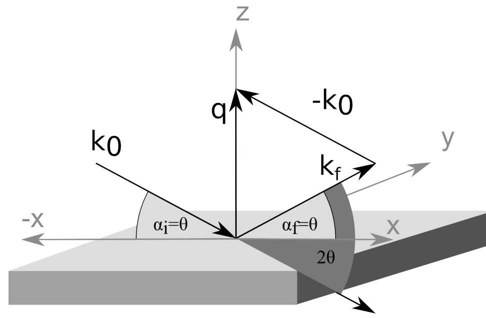

Figure 2.7.: Schematics of the $\theta/2\theta$ geometry in the sample coordinate system.

2.5. Co-Planar Experiments

In X-ray diffraction the plane spanned by the incoming wave $\mathbf{k}_0$ and the scattered wave $\mathbf{k}_f$ is called the *scattering plane*. This plane divides X-ray experiments into *co-planar* and *non-co-planar* scans. For co-planar scans the surface normal of the sample is contained within the scattering plane while for non-co-planar ones it is not. $\theta/2\theta$ scans and *rocking curves* discussed in the following are co-planar scans while in grazing incidence reciprocal space mapping mainly non-co-planar data is recorded.

2.5.1. The $\theta/2\theta$-Experiment

A schematic representation of the $\theta/2\theta$ scan in the sample coordinate system is given in Fig. 2.7. The main characteristic of this setup is a synchronous variation of the angle of incidence and diffraction, both called θ. Due to this symmetric configuration the beam is reflected *specularly* from the sample and the primary and the diffracted beam always enclose an angle of 2θ (Fig. 2.7). I.e. the scattering vector is constantly perpendicular onto the sample surface and only its length is changed. Hence it follows that only crystallites oriented parallel to the sample surface contribute to the diffraction pattern.

In the case of two-dimensional powders only one lattice plane is parallel to the substrate surface and therefore only one Bragg peak and its higher order reflections are expected in a specular pattern. This is not the case if the two-dimensional powder is polymorphic, i.e. it is built from crystallites of different crystallographic phases each obeying a preferred orientation. In that case more than one - but a small number of - Bragg peak series will be observed.

2.5.2. Rocking Curves

The length of the scattering vector is solely determined by the angle between primary and scattered wave (2θ, Eq. (1.34)). For rocking curves this 2θ angle is set to a constant value, and the incidence angle - called ω now - is varied (Fig. 2.8 right). Due to the fixed 2θ-angle the scattered intensity is not sensitive to different lattice plane distances but to the number of crystallites which are oriented symmetrically to

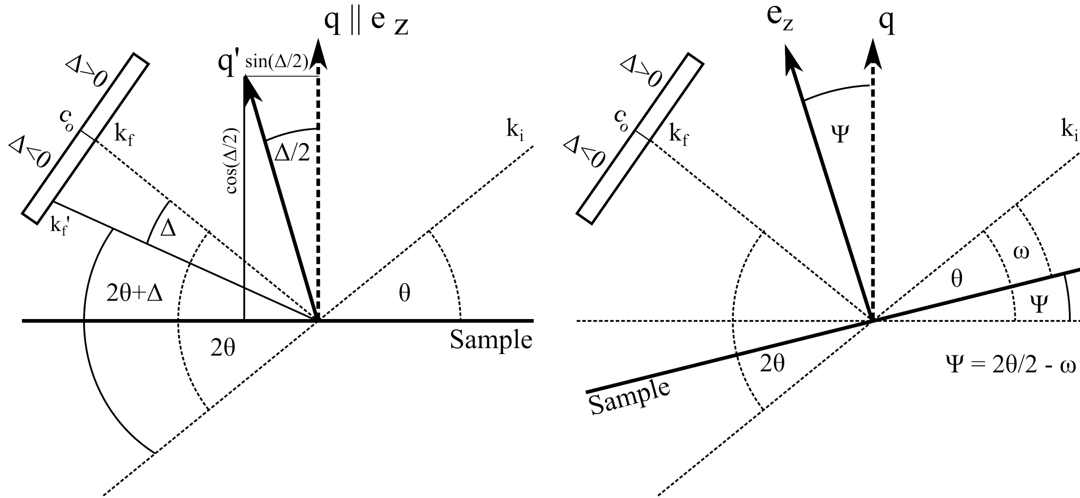

Figure 2.8.: Sketch of the beam paths when a one dimensional detector is used in co-planar scattering. Diffraction corresponding to a bunch of scattering vectors different in length and orientation is recorded simultaneously. **Left:** The situation of a $\theta/2\theta$ scan is shown. The dashed lines show the situation for a specular scattering vector ($\mathbf{q}$), the full lines the situation for an off specular scattering vector ($\mathbf{q}'$). The components of the scattering vector are calculated according to Eq. 2.19. **Right:** The situation for a rocking scan is shown. The components of the scattering vector in the sample coordinate system are calculated according to Eq. 2.20

incoming and diffracted wave. Hence the orientation distribution of the crystallites can be mapped. In studying two-dimensional powders this scan is used to check how well defined the preferred orientation of the crystallites is.

2.5.3. Co-Planar Scans with a One Dimensional Detector

$\theta/2\theta$ Scans If a one dimensional detector is used in a $\theta/2\theta$ scan, not only the specular scattering vector but also a bunch of off-specular scattering vectors are recorded (sketched in Fig. 2.8 left). In that case also co-planar data can be presented as a reciprocal space map. Figure 2.9 shows on the left the raw data of such an experiment with the incidence angle θ on the x-axis and the detector angle Δ on the y-axis. According to Fig. 2.8 (left) the q-coordinates for each pixel of the raw data are calculated as

$$\begin{aligned} q &= \tfrac{4\pi}{\lambda}\sin(\theta+\Delta/2), \\ q_p &= -q\sin(\Delta/2), \\ q_z &= q\cos(\Delta/2). \end{aligned} \tag{2.19}$$

The right image of Fig. 2.9 shows the result of applying these equations to the raw data.

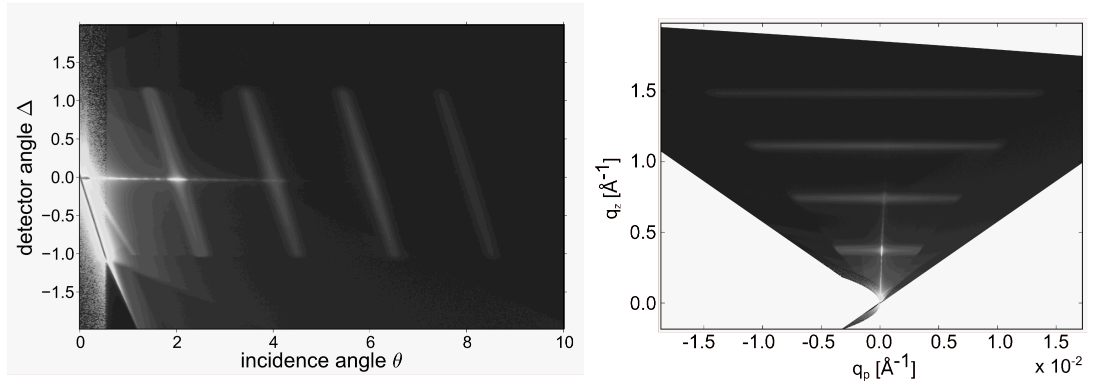

Figure 2.9.: **Left:** $\theta/2\theta$ scan measured with a one-dimensional detector. **Right:** The data transformed to q

Rocking Curves In the case above the accessible q_p-range is limited by the size of the detector. To measure the maximum q_p range possible in a co-planer experiment one has to perform a rocking scan. I.e. each channel of the detector is kept at a fixed angle $2\theta = 2\theta_{c0} + \Delta$ and the incidence angle ω is changed (independently of 2θ from $0 \ldots 2\theta$). Hence there is no relationship between 2θ and ω. Therefore 2θ and ω have to be used as coordinates for transforming to $\mathbf{q}$ (Fig. 2.8 right) (this is contrary to the above case where it was sufficient to know (the constant) Δ)

$$\begin{aligned} q &= \frac{4\pi}{\lambda}\sin(2\theta/2), \\ q_p &= q\sin(\omega - 2\theta/2), \\ q_z &= q\cos(\omega - 2\theta/2). \end{aligned} \tag{2.20}$$

Please note that rocking scans are a good possibility to fill the part of a pattern which is not accessible in grazing incidence geometry. An example of this application is found in Fig. 5.2.

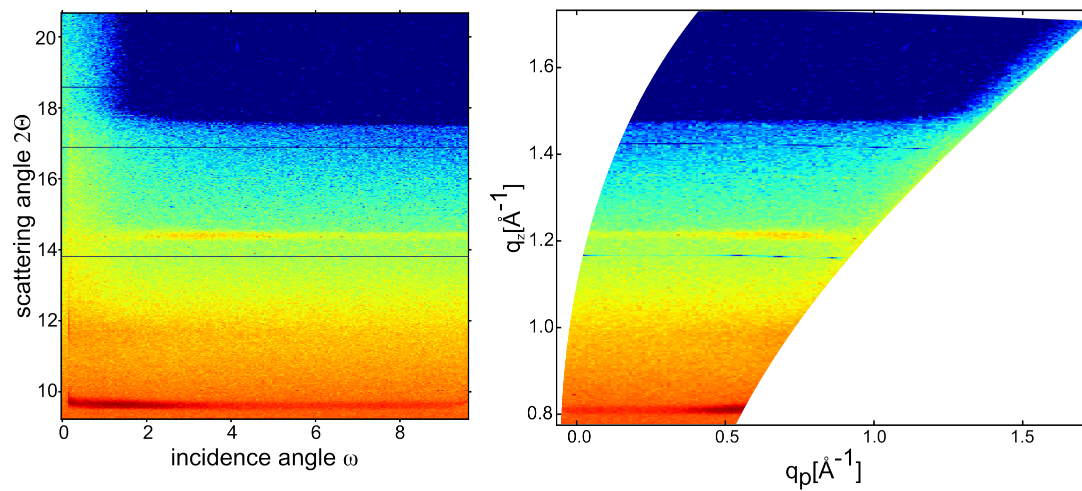

Figure 2.10.: **Left:** Rocking curve measured with a one-dimensional detector. **Right:** The data transformed to q. The same data is shown together with grazing incidence data in Fig. 5.2.

2.6. Grazing Incidence Diffraction

Above it was outlined that for two-dimensional powders only information on one family of lattice planes is obtained from specular scans. This information is not sufficient to perform an indexation and in the following a crystal structure determination.

Grazing Incidence Diffraction (GID) is a surface (sensitive) diffraction technique well suited for obtaining lateral crystallographic information from thin-textured films. In GID one works with an incidence angle near the critical angle of total external reflection; i.e. for organic materials it is commonly chosen below $0.5°$. At these angles very low penetration depths are achieved and scattering mainly from the top layers is observed, i.e. from the organic film. The penetration depth is below 10nm for angles smaller than α_c while it exceeds 100 μm at specular Bragg peaks.

Another advantage of this setup is that for an incidence angle near to the critical angle an enhancement of the intensity is observed. This is due to refraction effects and is described by the transmission function. The transmission function (T_i) depends on the incidence angle and the electron density ($\rho_e \propto \delta$). Neglecting absorption it is (Dosch; 1987)

$$T_i(\alpha_i, \delta) = \frac{2 \sin \alpha_i}{\sin \alpha_i + \sqrt{\sin \alpha_i^2 - 2\delta}}. \tag{2.21}$$

Multiplying the right side by $\frac{2k}{2k}$, and substituting 2δ by the critical angle gives

$$T_i(q, \alpha_c) = \frac{2q}{q + \sqrt{q^2 - 4k^2\alpha_c^2}}. \tag{2.22}$$

Finally dividing by q and considering that α_c is generally very small and hence $\alpha_c \simeq \sin \alpha_c$ results in an expression which depends only on the scattering vector

$$T_i(q, q_c) = \frac{2}{1 + \sqrt{1 - q_c^2/q^2}}. \tag{2.23}$$

The transmission function takes it maximum value of 2 at the critical angle of total reflection. Therefore a fourfold enhancement of the measured intensity $I_m = I \cdot T_i^2$ is observed, if the incidence angle is set to the critical angle of total reflection. Please note that an analogous expression holds for the diffracted wave. Instead of the incidence angle α_i the out-of-plane diffraction angle α_f is the independent variable and the function is called T_f.

GID is also suited for the investigation of layers as thin as mono-layers. It is recalled that the diffracted intensity is proportional to the number of unit cells illuminated in the direction of the scattering vector (Eq. (1.33)). Therefore, the diffracted intensity of a thin layer increases with the in-plane component of the scattering vector.

In grazing incidence diffraction with a fixed incidence angle ($\alpha_i \approx 0$) not the whole reciprocal space is accessible. The accessible region of reciprocal space for a fixed incidence angle can be determined from Eq. (2.1)-(2.5). These equations show that all reciprocal lattice points within a circle of radius $2\pi/\lambda$ centered at $2\pi/\lambda(\cos \alpha_i, -\sin \alpha_i)$

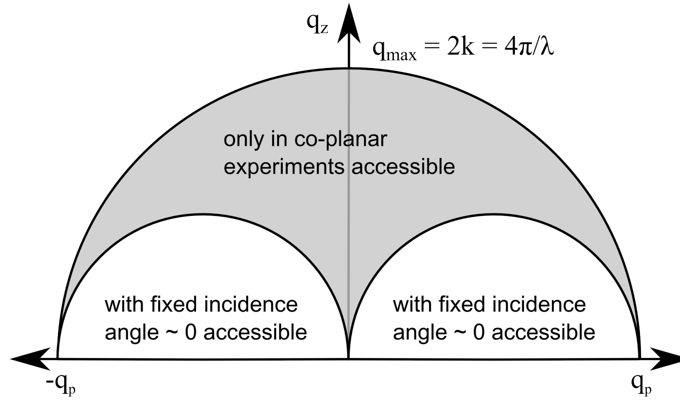

Figure 2.11.: Sketch of the accessible region in co-planar and grazing incidence geometry with incidence angle $\alpha_i \approx 0$.

can be accessed (sketched in Fig. 2.11). For small incidence angles this is in very good approximation the region which cannot be accessed by experiments in co-planar geometry, making these two techniques complementary. A reciprocal space map where these two techniques have been combined is shown in Fig. 5.2.

2.6.1. Transformation Equations for Different Goniometer Geometries

As mentioned in the introduction within this work different goniometer geometries were used. For each geometry the transformation to the sample system is different. In the following sections transformation equations for the used experimental setups will be derived.

The Z-Axis Setup

The z-axis setup (Fig.: 2.12 (a)) is very common in surface diffraction (Lohmeier and Vlieg; 1993; Bloch; 1985). The rotation axes of the goniometer are the axes of the laboratory coordinate system x_L, y_L, z_L and the laboratory coordinate system coincides with the sample system as long as ω and χ are set to zero (Fig. 2.6 (a)). In this setup the goniometer motors are directly corresponding to the angles in the sample coordinate system $\alpha_i = \omega, \theta_f = \nu$ and $\alpha_f = \delta$. The δ-motor is mounted on top of the ν motor; i.e. a ν-rotation influences the δ-rotation-axis. Hence the scattered beam is given by a rotation around the z-axis of the laboratory system, followed by a rotation around the rotated y-axis (Fig. 2.6 (a)). This is the same sequence of rotations as used above (Eq. 2.16). Hence the scattering vector can be calculated according to above formulas with α_i, α_f and θ_f substituted by ω, ν, and δ

$$\mathbf{k_f} = \frac{2\pi}{\lambda}\mathbf{R_z}(\nu)\mathbf{R_y}(-\delta)\mathbf{e_x}.$$

If a one dimensional detector mounted vertically on the goniometer is used the formulas change as derived in the following.

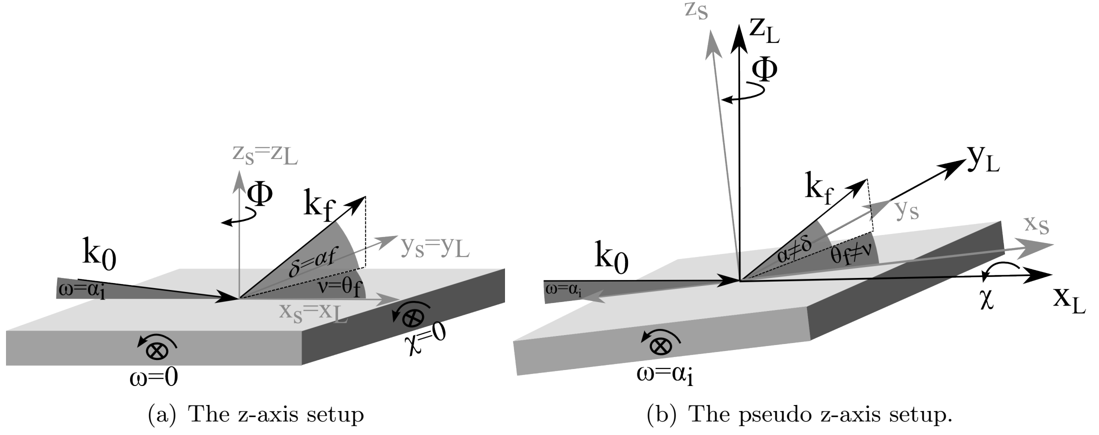

(a) The z-axis setup

(b) The pseudo z-axis setup.

Figure 2.12.: (a) The z-axis setup and (b) the pseudo-z-axis setup. The sample coordinate system and the laboratory coordinate system are sketched. Also the names for the goniometer angles are defined.

The position vector to the channel number c - with all motors set to 0 - is given as $\mathbf{d}_c = (1, 0, \tan\Delta)$. Δ is the detector angle which is calculated from the channel number c (Eq. 2.18). By applying the goniometer rotations to the position vector $\mathbf{d}_c$ one obtains the diffracted wave vector $\mathbf{k}_{f_c}$ corresponding to this channel. Elastic scattering is used and therefore $\mathbf{d}_c$ has to be normed because otherwise the length of $\mathbf{k}_{f_c}$ would be different from $\mathbf{k}_0$.

$$\begin{aligned}\mathbf{k}_{f_c} &= \frac{2\pi}{\lambda}\mathbf{R_z}(\nu)\mathbf{R_y}(-\delta)\frac{\mathbf{d}_c}{|\mathbf{d}_c|} \\ &= \frac{2\pi}{\lambda\sqrt{1+\tan\Delta^2}}\begin{pmatrix}\cos\nu(\cos\delta - \sin\delta\tan\Delta)\\ \sin\nu(\cos\delta-\sin\delta\tan\Delta)\\ \sin\delta+\cos\delta\tan\Delta\end{pmatrix}\end{aligned} \tag{2.24}$$

Calculating the in-plane scattering angle

$$\begin{aligned}\tan\theta_f &= \frac{k_{f_c,y}}{k_{f_c,x}} \\ &= \frac{\sin\nu}{\cos\nu}\times\frac{(\cos\delta-\sin\delta\tan\Delta)}{(\cos\delta-\sin\delta\tan\Delta)} \\ &= \tan\nu \\ &\Rightarrow \\ \theta_f &\equiv \nu\end{aligned} \tag{2.25}$$

shows that θ_f is independent of Δ, i.e. for each channel of the detector (each scattering vector measured simultaneously) the in-plane scattering angle is the same and equals the motor position ν (Fig. 2.14).

The Pseudo Z-Axis Mode

Very often it is more convenient to set α_i by tilting the sample (around the y-axis) instead of the incoming X-ray beam. Then the sample coordinate system and laboratory system do not coincide and after calculating $\mathbf{k}_{f_c}$ according to equation (2.24) one has to transform it into the sample system. This transformation is performed with a positive rotation around the y-axis

$$\begin{aligned}
\mathbf{k}'_{f_c} &= \mathbf{R_y}(\alpha_\mathbf{i})\mathbf{k}_{f_c} \\
&= \frac{2\pi}{\lambda\sqrt{1+\tan\Delta^2}} \begin{pmatrix} \cos\alpha_i & 0 & \sin\alpha_i \\ 0 & 1 & 0 \\ -\sin\alpha_i & 0 & \cos\alpha_i \end{pmatrix} \begin{pmatrix} \cos\nu(\cos\delta - \sin\delta\tan\Delta) \\ \sin\nu(\cos\delta - \sin\delta\tan\Delta) \\ \sin\delta + \cos\delta\tan\Delta \end{pmatrix} \qquad (2.26) \\
&= \frac{2\pi}{\lambda\sqrt{1+\tan\Delta^2}} \begin{pmatrix} \cos\alpha_i\cos\nu(\cos\delta - \sin\delta\tan\Delta) + \sin\alpha_i(\sin\delta + \cos\delta\tan\Delta) \\ \sin\nu(\cos\delta - \sin\delta\tan\Delta) \\ -\sin\alpha_i\cos\nu(\cos\delta - \sin\delta\tan\Delta) + \cos\alpha_i(\sin\delta + \cos\delta\tan\Delta) \end{pmatrix}.
\end{aligned}$$

Comparing the x- and y-component of the $\mathbf{k}'_{f_c}$-vector it is seen that Δ does no more cancel out if the in-plane scattering angle θ_f is calculated as above (Eq. (2.25)). That is, not only α_f but also θ_f depends on Δ (or rather the channel number). In grazing incidence diffraction this is not crucial because due to the small incidence angle the tilt is negligible ($\sin\alpha_i \simeq 0$ and $\cos\alpha_i \simeq 1$ in the term for the x-component).

The 2+2 Geometry

The 2+2 geometry is very similar to the z-axis setup. The degrees of freedom for rotating the detector and sample are the same as in the z-axis setup. But the motors of the detector are mounted opposite. The first rotation is around the y-axis (angle δ) and the second one around the rotated z-axis=z'-axis (angle ν). That is, the detector moves in a plane enclosing the angle δ with the sample surface (Fig. 2.13(left)). Hence – compared to the z-axis geometry – one has to switch the sequence of the rotations:

$$\begin{aligned}
\mathbf{k_f}_c &= \frac{2\pi}{\lambda}\mathbf{R_y}(-\delta)\mathbf{R_z}(\nu)\frac{\mathbf{d}_c}{|\mathbf{d}_c|} \qquad (2.27) \\
&= \frac{2\pi}{\lambda\sqrt{1+\tan\Delta^2}} \begin{pmatrix} \cos\nu\cos\delta - \sin\delta\tan\Delta \\ \sin\nu \\ \sin\delta\cos\nu + \cos\delta\tan\Delta \end{pmatrix}.
\end{aligned}$$

Like in the pseudo z-axis setup the in-plane θ_f and out-of-plane scattering angle α_f depend on Δ. While in the pseudo z-axis setup the detector tilt was determined by the incidence angle it is here determined by the value of δ. This leads to a significant tilt which is sketched in Fig. 2.14.

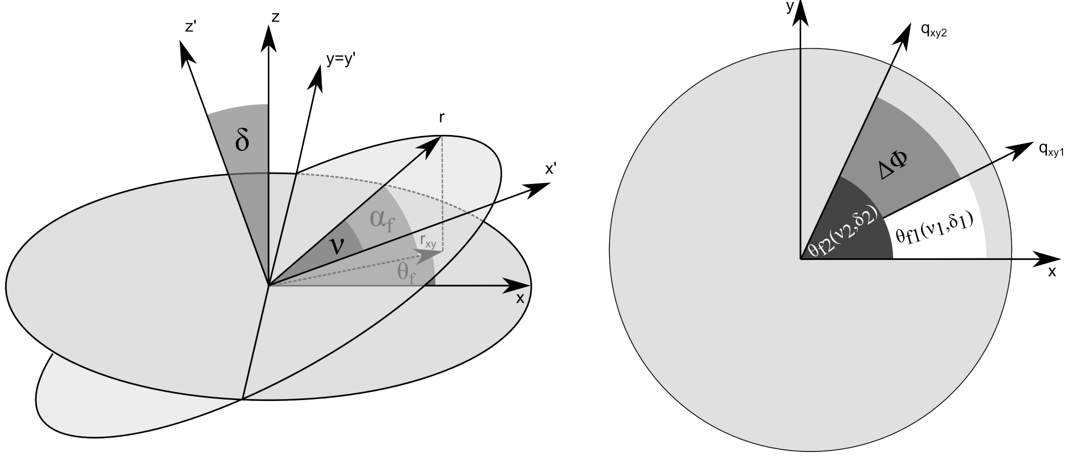

Figure 2.13.: **Left:** Sketch of the 2+2 geometry. The vector $\mathbf{r}$ points towards the detector at position (ν, δ). δ is the rotation angle around the y-axis and ν the rotation angle around the z'-axis. The ν-rotation moves the detector in the plane which encloses the angle δ with the sample surface. The azimuth and elevation in the sample coordinate system θ_f and α_f are also sketched. **Right:** The projection of two scattering vectors onto the sample surface. To measure the correct azimuthal angle between $\mathbf{q_1}$ and $\mathbf{q_2}$ ϕ has to be realigned about $\Delta\phi$ (Eq. 2.29)

Grazing Incidence Pole Figures in 2+2 Geometry

If azimuthal relationships (pole figures) in the 2+2 geometry are measured it has to be considered, that the projection of the scattering vector onto the sample depends on the position of the detector. This is sketched in the left image of Fig. 2.13. The vector $\mathbf{r}$ points towards the detector at position (ν, δ), and its projection on the sample surface is $\mathbf{r_{xy}}$. The angles θ_f and α_f are the azimuth and elevation in the sample coordinate system. If the detector is moved around the z'-axis both θ_f and α_f change. To measure the correct azimuthal relation between two lattice planes the rotation angle around the sample surface normal ϕ has to be realigned. The actual value of the realignment depends on the detector position (ν,δ).

In the 2+2 geometry the scattering vector in the sample coordinate system is

$$\mathbf{q} = \begin{pmatrix} \cos\nu\cos\delta - \cos\alpha_i \\ \sin\nu \\ \cos\nu\sin\delta + \sin\alpha_i \end{pmatrix}. \tag{2.28}$$

For each scattering vector (detector position) the azimuthal angle ($\theta_f = \angle(\mathbf{q}_{xy}, \mathbf{e}_x)$) in the (x,y)-plane is calculated. The differences $\Delta\phi_n$ relative to θ_f of the first experiment gives the necessary realignment (right image in Fig.: 2.13); i.e. the first experiment

defines the zero point of ϕ on the sample.

$$\begin{aligned}
\theta_{f1} &= \arctan\left(\frac{q_{1y}}{q_{1x}}\right) = \arctan\left(\frac{\sin\nu_1}{\cos\nu_1\cos\delta_1 - 1}\right) \\
\theta_{fn} &= \arctan\left(\frac{q_{ny}}{q_{nx}}\right) = \arctan\left(\frac{\sin\nu_n}{\cos\nu_n\cos\delta_n - 1}\right) \\
\Delta\phi_n &= \theta_{f1} - \theta_{fn}
\end{aligned} \tag{2.29}$$

Please note that the above formulas are only valid for point detectors, or rather the zero channel of a one-dimensional detector.

The pseudo 2+2 Geometry

Also in the 2+2 geometry the incidence angle is frequently set by tilting the sample (as in the pseudo z-axis geometry). It can be taken into account as in the above treatment (Eq. (2.26)) and it follows

$$\begin{aligned}
\mathbf{k_f}'_c &= \mathbf{R_y}(\alpha_\mathbf{i})\mathbf{k_f}_c \\
&= \frac{2\pi}{\lambda\sqrt{1+\tan\Delta^2}} \begin{pmatrix} \cos\alpha_i & 0 & \sin\alpha_i \\ 0 & 1 & 0 \\ -\sin\alpha_i & 0 & \cos\alpha_i \end{pmatrix} \begin{pmatrix} \cos\nu\cos\delta - \sin\delta\tan\Delta \\ \sin\nu \\ \sin\delta\cos\nu + \cos\delta\tan\Delta \end{pmatrix} \\
&= \frac{2\pi}{\lambda\sqrt{1+\tan\Delta^2}} \begin{pmatrix} \cos\alpha_i(\cos\nu\cos\delta - \sin\delta\tan\Delta) + \sin\alpha_i(\sin\delta\cos\nu + \cos\delta\tan\Delta) \\ \sin\nu \\ -\sin\alpha_i(\cos\nu\cos\delta - \sin\delta\tan\Delta) + \cos\alpha_i(\sin\delta\cos\nu + \cos\delta\tan\Delta) \end{pmatrix}.
\end{aligned} \tag{2.30}$$

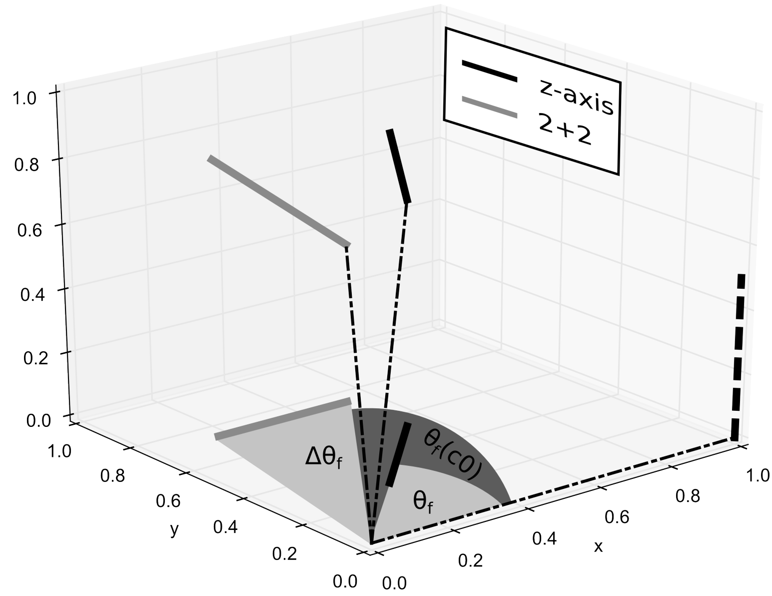

Figure 2.14.: Detector movements in the z-axis (black) and 2+2 setup (grey). The black dash-dotted lines give the arm on which the detector is mounted, the thick dashed black line represents the position of the detector when all diffractometer angles are set to zero. The solid black and grey line show the detector position for the two geometries with the two detector angles set to 45 degrees. The black and grey line in the (x,y) plane represent the projection of the detector onto the sample surface. Clearly it can be recognized, that in the z-axis setup each channel measures the same in-plane scattering angle θ_f while in the 2+2 geometry the detector is heavily tilted and each diffracted wave measured simultaneously corresponds to a different in-plane diffraction angle $(\theta_f(c_0) + \Delta\theta_f)$.

2.7. Intensity Correction

For a crystal structure determination structure factor amplitudes are necessary. These amplitudes can be determined from Bragg peak intensities because

$$I \propto |F|^2. \tag{2.31}$$

The intensity is not equal to the structure factor because several correction factors – considering geometrical influences of the experiment – have to be applied. For surface diffraction there are four correction factors necessary. They have been derived in the sample coordinate system by Smilgies (2002). Applying the correction factors the proportionality is turned into an equality

$$I = L \cdot P \cdot A \cdot R \cdot |F|^2, \tag{2.32}$$

and the squared structure factor can be calculated

$$|F|^2 = \frac{I}{LPAR}. \tag{2.33}$$

The four correction factors are

L ... the Lorentz factor,
P ... the polarization factor,
A ... the area factor,
R ... the rod interception factor.

2.7.1. Correction Factors in the Sample Coordinate System

In the following the equations for L, P, and R as derived by Smilgies (2002) will be reproduced. Please consult the reference for details. For the area factor a numerical approach was used; the details will be outlined.

The Lorentz Factor takes into account how the detector entrance window intersects the Ewald sphere for different goniometer angles. For the z-axis setup at a synchrotron it is given by

$$L = 1/(\cos(\alpha_i)\sin(\theta_f)\cos(\alpha_f)). \tag{2.34}$$

The Polarization Factor is influenced by the polarization of the X-ray source. Taking into account that synchrotron radiation is horizontally polarized in the ring plane, the polarization factor

$$P = \cos^2(\alpha_f)\cos^2(\theta_f) + \sin^2(\alpha_f) \tag{2.35}$$

follows.

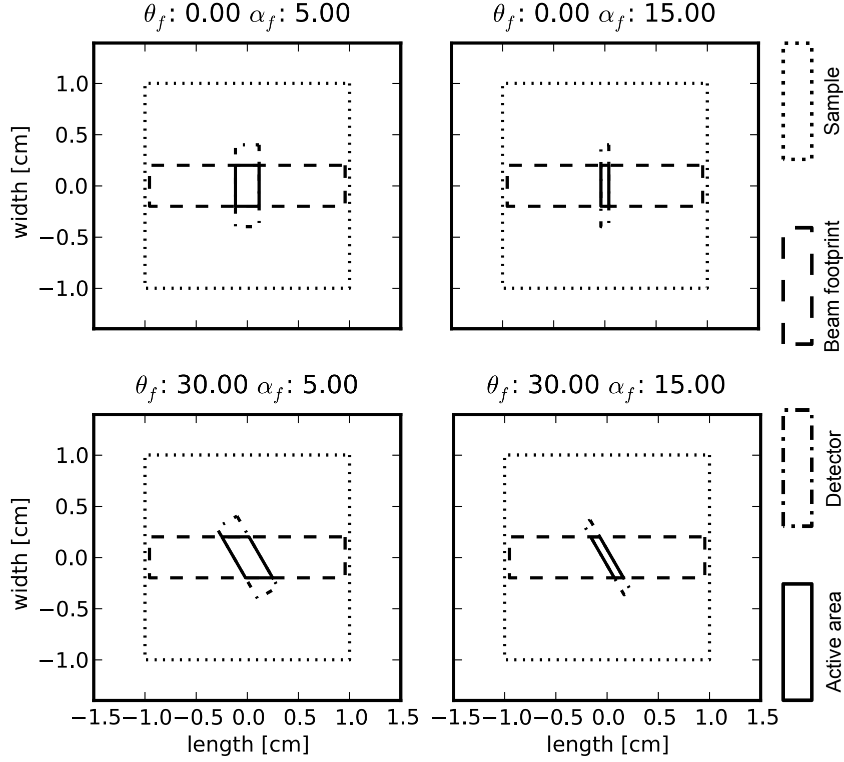

Figure 2.15.: Visualization of the active area for different detector positions. The used parameters are: $\alpha_i = 0.15°$, $SI_w \times SI_h = (0.4 \times 0.005)$cm, $SO_w \times SO_h = (0.8 \times 0.02)$cm (Variables are defined in the text). Please note the primary beam strikes the sample from the right.

The Area Factor takes into account that depending on sample position the beam footprint on the sample changes. It also considers, that depending on the detector position, the portion of the sample "seen" by the detector changes. The cut of a rectangle representing the sample, with one representing the beam footprint and one representing the region seen by detector is the active area for the intensity (Fig. 2.15). The calculations of the rectangle sizes are executed under the assumption of a perfectly parallel beam. Fig. 2.15 gives four examples for the active area. The angular positions θ_f and α_f are given in the titles of the plots.

The footprint of the incoming beam is a rectangle with

$$\text{length} \times \text{width} = \frac{SI_h}{\sin(\alpha_i)} \times SI_w. \tag{2.36}$$

With SI_h and SI_w the height and width of the incoming slits in front of the sample. α_i is the incidence angle. The area that the detector sees is given by an analogous expression. It depends on the height SO_h and width SO_w of the slit in front of the

detector, and the out-of-plane scattering angle α_f. For $\theta_f = 0$ it reads

$$\text{length} \times \text{width} = \frac{SO_h}{\sin(\alpha_f)} \times SO_w. \quad (2.37)$$

The θ_f-rotation is then taken into account by rotating this rectangle around the z-axis. Please note that this is strictly only valid for the z-axis geometry, but has been also applied this way for the 2+2 geometry. This is definitely a point which needs closer inspection for upcoming experiments because the tilt of the detector in the 2+2 geometry should be taken into account.

SO_h and SO_w are height and width of the slit on the receiving side. While for a point detector this values are well defined the situation is different for one-dimensional ones. The width is still given by the used slit or the entrance window of the used Soller slits. But for the height there is no beam limiting element and therefore the vertical "slit height" is given by the size of the single channels on the detector.

Actual calculation of the active area was done with the python polygon package (Rädler; n.d.). This package allows to define several polygons and to perform enables cutting operations.

The Rod Interception Factor according to Smilgies (2002) is necessary because: *"Scattering from a surface is diffuse in the direction of the surface normal, the so-called scattering rods (Feidenhans'l; 1989; Robinson and Tweet; 1992). For proper integrated intensities, the interception of the rod, as defined by the detector slits, has to be corrected for (Feidenhans'l; 1989). The rod is measured with a fixed slit size and not with fixed Δq_z."*

The expression for R depends on the slit height, SO_h, and the out-of-plane diffraction angle, α_f

$$R = SO_h \cos(\alpha_f). \quad (2.38)$$

2.7.2. Magnitude of Correction Factors

To get an impression about the magnitude of the correction factors they are shown in Fig. 2.16 for a region of reciprocal space, where – for organic rod like molecules – strong peaks are observed. Black crosses indicate peak positions of the thin-film phase of pentacene. The indicated peaks have been used in a test where the thin-film phase of pentacene was solved (details in Chap. 4).

In Fig. 2.16 the reciprocal value of each correction factor – scaled to the interval $[0 \ldots 1]$ – is shown. The values have been calculated for the following parameters:

$$\begin{aligned}
\alpha_i &= 0.15°, \\
\theta_f &= [10° \ldots 45°], \\
\alpha_f &= [0° \ldots 30°], \\
\lambda &\approx 1.27[\text{Å}] \approx 10[\text{keV}], \\
SI_w \times SI_h &= (0.4 \times 0.2)\text{cm}, \\
SO_w \times SO_h &= (0.8 \times 0.02)\text{cm}.
\end{aligned}$$

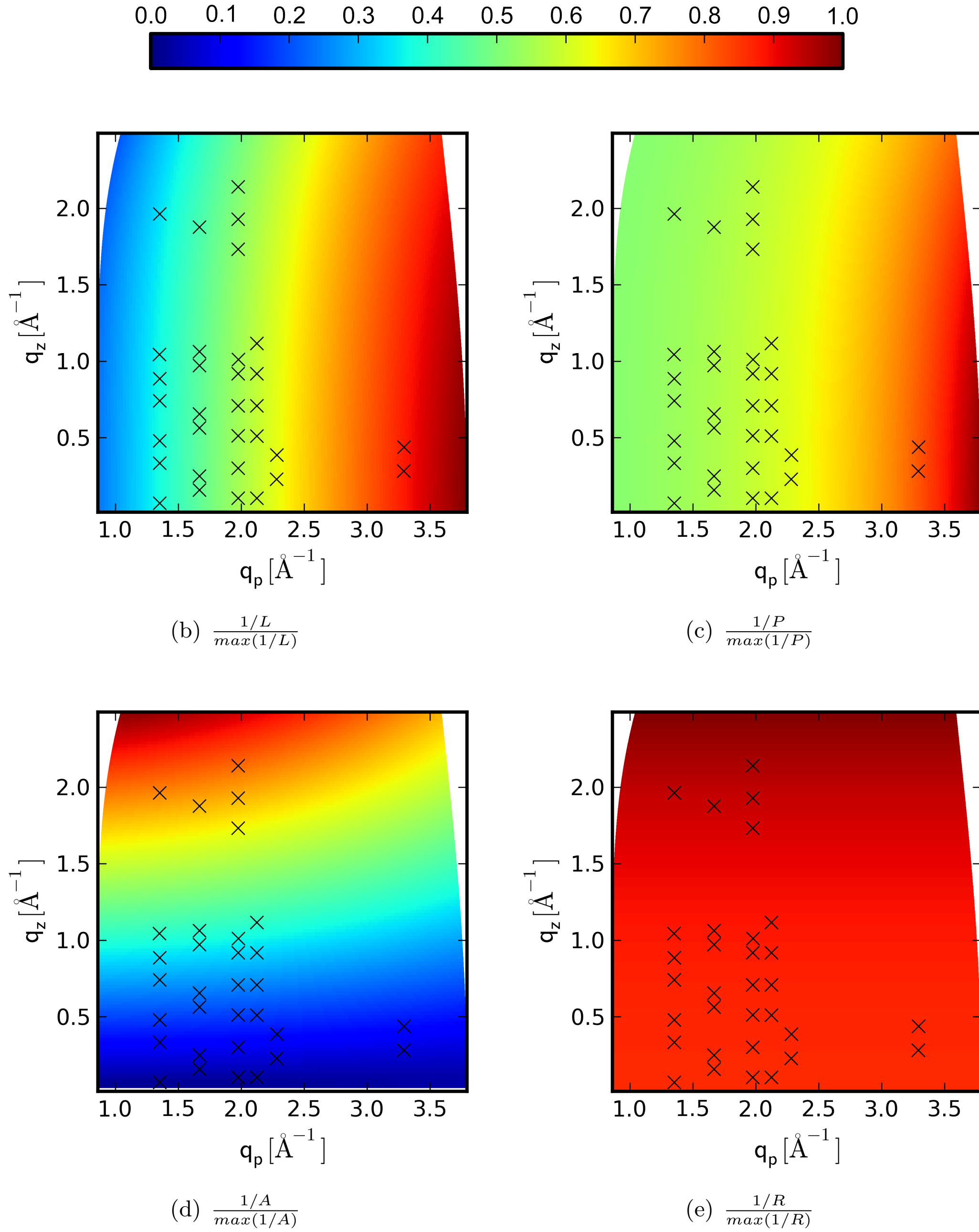

(b) $\frac{1/L}{max(1/L)}$

(c) $\frac{1/P}{max(1/P)}$

(d) $\frac{1/A}{max(1/A)}$

(e) $\frac{1/R}{max(1/R)}$

Figure 2.16.: Visualization of the reciprocal Lorentz factor (b), polarization factor (c), area factor (d) and rod interception factor (e). The black crosses show peak positions of pentacene, and the correction factors for these positions are shown in detail in Fig. 2.17. The top colorbar shows the color scaling for all pictures.

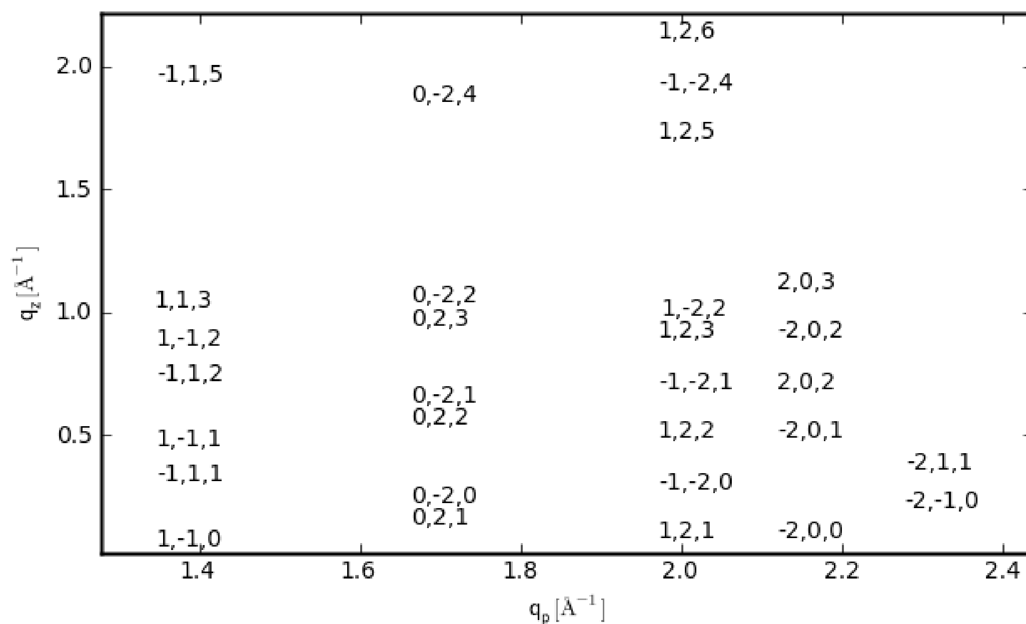

(a) Indexation of pentacene positions shown in Fig. 2.16. Please note that the axes limits are different. Therefore the two rightmost peaks of above maps are not contained here. Their indexation is -3,-1,0 for the lower and -3,1,1 for the upper position.

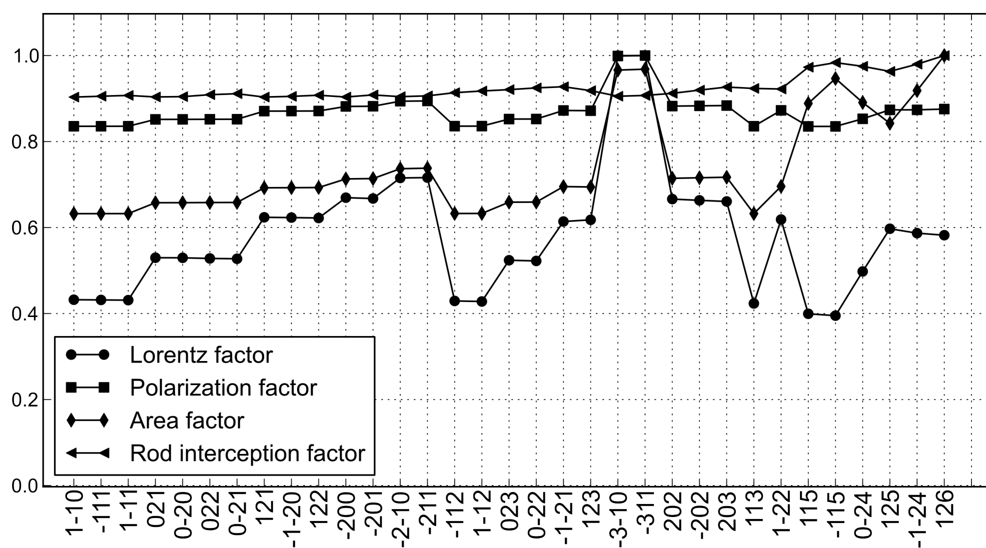

(b) Calculated relative correction factors for the selected peaks shown as crosses in the maps in Fig. 2.16.

Figure 2.17.: Effect of correction factors on selected peak positions.

Subsequently the data has been transformed to q. Please note, the correction factors – although shown in q – depend on the diffraction angles. Hence they are wavelength dependent. A wavelength independent representation is not possible.

Additionally to the pseudo color plots in Fig. 2.16 the concrete correction factors for the pentacenen peak positions are shown in Fig. 2.17. From both figures it is evident, that the polarization factor and rod interception factor play a minor role for the correction of the intesities. Especially the rod interception factor is virtually constant in the investigated region and could safely be ignored for correction.

This is not the case for the Lorentz and area factor. The Lorentz factor changes mainly along q_p because the sine in

$$L = 1/(\cos(\alpha_i)\sin(\theta_f)\cos(\alpha_f)) \tag{2.39}$$

has a steep slope in this region while the slope of the cosine is rather slight for the investigated angular region.

Also the area factor has a strong influence. The area changes strongly with α_f while θ_f only has a minor influence. This can be understood by looking at Fig. 2.15. By elevating the detector (angle α_f) the footprint gets quickly smaller ($\propto 1/\sin(\alpha_f)$) while rotating the detector around the z-axis (θ_f) increases the active area only slightly. Furthermore for some $\theta_{f\min} < \theta_f < \theta_{f\max}$ it can even happen that the active area does not depend on θ_f any more, because the “detector rectangle”is then completely contained within the beam footprint.

3. PyGid

PyGid is a software designed for reciprocal space map analysis of two-dimensional powders, measured in grazing incidence geometry. Its main focus leis on the crystal structure determination of thin organic films. In the following, some underlying concepts and aspects concerning the indexation, data handling, and intensity extraction will be outlined. These explanations should avoid that the program behaves like a black box for the user.

PyGid is an advancement of the MATLAB tool `indapp_ng` (Moser; 2008). One major difference is the change to the python programming language. Due to its open source nature no license restrictions exist. This makes the program easily usable by everyone. A further advantage of python is that it is for computing tasks already today quite popular and it seems its popularity will further increase. At the European synchrotron radiation facility, for example, its use is promoted as well. Because of its wide spread there are several libraries aimed to the scientific community. But due to the fact that python is a full-fledged programming language also general task libraries (e.g. graphical user interface libraries, data base interfaces) are available. This makes it in many aspects superior to MATLAB. One disadvantage is that in some aspects the python libraries are not as efficient as MATLAB libraries. But for the development of PyGid this was not a major drawback.

3.1. Simulation of Bragg Peak Positions

For (manual) indexation the positions of Bragg peaks – i.e. the parallel and z-component of the scattering vector $\mathbf{q}$ – in an orthogonal coordinate system have to be calculated. As is known from Sec. 1.4.1, a Bragg peak is observed if the scattering vector $\mathbf{q}$ coincides with any vector of the reciprocal lattice. Therefore Bragg peak positions can be generated as linear combinations of the reciprocal lattice base $\mathbf{a}^*, \mathbf{b}^*$ and $\mathbf{c}^*$

$$\mathbf{q}_{hkl} = h\mathbf{a}^* + k\mathbf{b}^* + l\mathbf{c}^*, \tag{3.1}$$

where h,k and l are the Laue indices of the respective Bragg reflex. As already mentioned above (Sec. 2.2), one is generally interested in the orientational relation between crystallites and the substrate. Hence, it is a good choice to calculate the Bragg peak positions in the sample coordinate system via a coordinate transformation

$$\mathbf{q} = \mathbf{A} \cdot \begin{pmatrix} h \\ k \\ l \end{pmatrix}. \tag{3.2}$$

One possible matrix for the transformation is (Salzmann and Resel; 2004)

$$\mathbf{A} = \begin{pmatrix} a^* \sin\beta^* \sin\gamma & 0 & 0 \\ -a^* \sin\beta^* \cos\gamma & b^* \sin\alpha^* & 0 \\ a^* \cos\beta^* & b^* \cos\alpha^* & c^* \end{pmatrix}. \tag{3.3}$$

This transformation matrix is valid for a textured film (two-dimensional powder) with the (001) lattice plane parallel to the substrate surface. Hence the $\mathbf{c}^*$-vector is parallel to the substrate surface normal (z-axis). How $\mathbf{b}^*$ and $\mathbf{a}^*$ are mapped to the sample system is irrelevant, because for a textured film only the in-plane-component (parallel component) $q_{xy} \equiv q_p = \sqrt{q_x^2 + q_y^2}$ can be measured. It is seen that for a successful indexation 7 parameters have to be determined: the 6 (reciprocal) unit cell parameters and the surface parallel lattice plane. The latter can often be deduced from a specular scan because this scan is exactly sensitive to the surface parallel lattice plane.

Change of Texture Axis; Rotation of the Crystal

If the (001) lattice plane is not parallel to the substrate the $\mathbf{A}$ matrix has to be transformed for indexation. It has to be rotated around an axis perpendicular to the plane spanned by the $[001]^*$-vector and the new orientation vector. This axis is calculated as the vector product between the two orientations, $\mathbf{o}_1$ and $\mathbf{o}_2$

$$\mathbf{n} = \frac{\mathbf{o_1} \times \mathbf{o_2}}{|\mathbf{o_1} \times \mathbf{o_2}|}.$$

The angle of rotation is obtained from the scalar product of the two orientations

$$\cos(\phi) = \frac{\mathbf{o_1 o_2}}{|\mathbf{o_1}||\mathbf{o_2}|}.$$

It has to be noted that these vector operations have to be performed in an orthogonal coordinate system. E.g. for a rotation from $[001]^*$ to $[111]^*$, $\mathbf{o_1}$ and $\mathbf{o_2}$ are given by

$$\mathbf{o_1} = \mathbf{A} \begin{pmatrix} 0 \\ 0 \\ 1 \end{pmatrix} \quad \mathbf{o_2} = \mathbf{A} \begin{pmatrix} 1 \\ 1 \\ 1 \end{pmatrix}.$$

The rotation matrix around axis $\mathbf{n}$ is then given by (Shmueli; 2006, sec. 1.1.4)

$$R_{ij} = n_i n_j (1 - \cos\phi) + \delta_{ij} \cos\phi - \epsilon_{ikj} n_k \sin\phi$$

or written in matrix form

$$\mathbf{R} = \begin{pmatrix} n_1^2(1-\cos\phi) + \cos\phi & n_2 n_1(1-\cos\phi) + n_3 sin(\phi) & n_3 n_1(1-\cos\phi) - n_2 \sin\phi \\ n_1 n_2(1-\cos\phi) - n_3 \sin\phi & n_2^2(1-\cos\phi) + \cos\phi & n_3 n_2(1-\cos\phi) + n_1 \sin\phi \\ n_1 n_3(1-\cos\phi) + n_2 \sin\phi & n_2 n_3(1-\cos\phi) - n_1 \sin\phi & n_3^2(1-\cos\phi) + \cos\phi \end{pmatrix}.$$

And finally the new $\mathbf{A}'$-Matrix, for simulating the spots of the rotated crystal is found

$$\mathbf{A}' = \mathbf{RA}.$$

3.1.1. Examples for Indexation

The positions of Bragg peaks in the surface reference frame are completely defined by the above equations. They depend on the lattice parameters, the Laue indices and the texture axis. Analytically analyzing these equations for special cases reveals typical Bragg peak patterns. In the following this is demonstrated for an (001) textured monoclinic and triclinic crystal structure. For an (001) orientation this can be done straight forward and the resulting formulas are relatively simple. For other orientations than (001) the **A**-matrix has to be transformed analytically, and for a "mixed" texture axis (e.g. $(1, 1, 4)$) the resulting formulas might get quite involved. Nevertheless this is a possibility to systematically approach an indexation problem and equations might be simplified again for special index-triplets (i.e. if one or two indices are set to zero).

A Monoclinic System

For monoclinic systems ($\alpha = \alpha^* = 90°$ and $\gamma = \gamma^* = 90°$) the **A** matrix simplifies and $\mathbf{q}$ in the sample coordinate system is calculated as

$$\mathbf{q} = \begin{pmatrix} a^* \sin\beta^* & 0 & 0 \\ 0 & b^* & 0 \\ a^* \cos\beta^* & 0 & c^* \end{pmatrix} \begin{pmatrix} h \\ k \\ l \end{pmatrix}. \tag{3.4}$$

Applying this to an arbitrary (h, k, l)-vector gives the relations for q_p and q_z

$$q_p = \sqrt{h^2 \cdot a^{*2} \sin\beta^{*2} + k^2 \cdot b^{*2}}, \tag{3.5}$$

$$q_z = h \cdot a^* \cos\beta^* + l \cdot c^*. \tag{3.6}$$

Some conclusions which can be drawn from these equations are:

- k has only an influence on the q_p position of the peak. Furthermore only its squared value is relevant for Eq. (3.5) and therefore peaks corresponding to $\pm k$ are observed at the same position. This is demonstrated by the $0 \pm 2l$ series in Fig. 3.1(a).
- The sign of h has no influence on the q_p position, but changes the q_z position according to

$$q_{z_{\pm hkl}} = l \cdot c^* \pm h \cdot a^* \cos\beta^*, \tag{3.7}$$

$$\Delta q_{z_{\pm hkl}} = 2h \cdot a^* \cos\beta^*. \tag{3.8}$$

  This is demonstrated by the $\pm h, 2, l$ series in Fig. 3.1(a). There it is also seen that the peaks are arranged symmetrically above and below the value of lc^*.
- l does only influence the q_z position. This should be evident because $\mathbf{c}^*$ was chosen parallel to the z-axis.

- For the q_z component of any $h00$ peak it follows

$$q_{z_{h00}} = h \cdot a^* \cos\beta^*, \tag{3.9}$$

and hence the angle enclosed by any $h00$ peak and the $\mathbf{e}_z$-axis (or rather the $00l$-series) is β^* (Fig 3.1(a)).

A Triclinic System

Here, no values in the **A**-matrix get zero (Eq. 3.4) and $\mathbf{q}$ in the sample system is

$$\mathbf{q} = \begin{pmatrix} h \cdot a^* \sin\beta^* \sin\gamma \\ -h \cdot a^* \sin\beta^* \cos\gamma + k \cdot b^* \sin\alpha^* \\ h \cdot a^* \cos\beta^* + k \cdot b^* \cos\alpha^* + l \cdot c^* \end{pmatrix}, \tag{3.10}$$

and it follows for q_p

$$\begin{aligned} q_p &= \sqrt{q_x^2 + q_y^2} && (3.11) \\ &= \sqrt{h^2 a^{*2} \sin\beta^{*2} \sin\gamma^2 + (kb^* \sin\alpha^* - ha^* \sin\beta^* \cos\gamma)^2} && (3.12) \\ &= \sqrt{h^2 a^{*2} \sin\beta^{*2} + k^2 b^{*2} \sin\alpha^{*2} - 2hkb^* a^* \sin\alpha^* \sin\beta^* \cos\gamma}. && (3.13) \end{aligned}$$

Substituting for γ from Eqs. (1.12) results in a representation of q_p which only depends on reciprocal lattice parameters. Finally it is found

$$\begin{aligned} q_p &= \sqrt{h^2 a^{*2} \sin\beta^{*2} + k^2 b^{*2} \sin\alpha^{*2} - 2hkb^* a^* (\cos\alpha^* \cos\beta^* - \cos\gamma^*)}, && (3.14) \\ q_z &= ha^* \cos\beta^* + kb^* \cos\alpha^* + lc^*. && (3.15) \end{aligned}$$

Of course these equations are now more involved than in the monoclinic case. Some conclusions which can be drawn from these equations are:

- k now has also an influence on the q_z component. Hence the $0, \pm 2, l$ series splits into two series with identical q_p component (Fig. 3.1(b)).

$$q_{z_{0 \pm k 0}} = lc^* \pm kb^* \cos\alpha^* \tag{3.16}$$

- l does still only influence the q_z-component, because c^* is still chosen parallel to the $\mathbf{e}_z$-direction.

- The $h00$-series behaves still as in the monoclinic case and the $0k0$-series behaves now analogously because $\alpha^* \neq 90°$

$$q_{z_{0k0}} = k \cdot b^* \cos\alpha^*, \tag{3.17}$$

and any $0k0$ peak encloses the angle α^* with the $\mathbf{e}_z$-axis (or rather the $00l$-series).

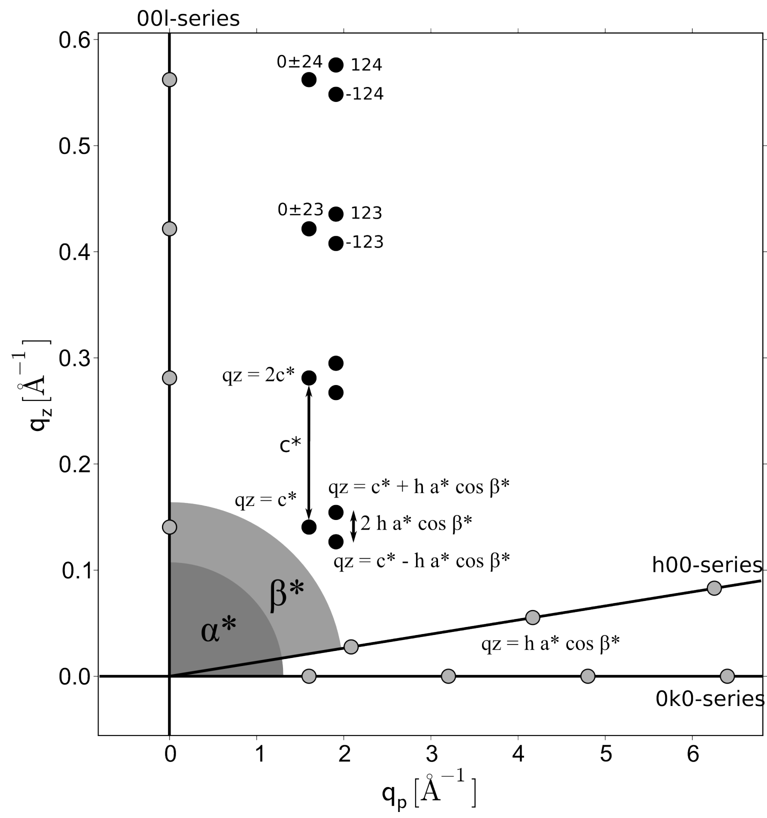

(a)

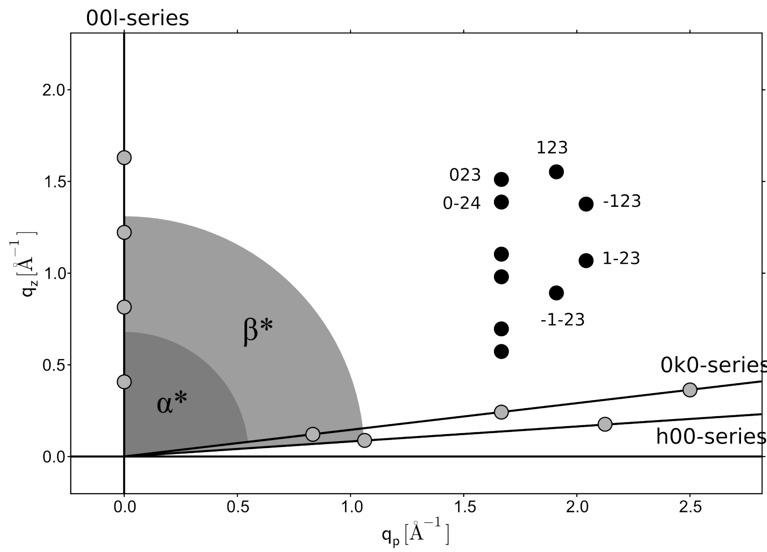

(b)

Figure 3.1.: Peak positions for selected indices in a (a) monoclinic and (b) triclinic system.

- The last term in the expression for q_p (Eq. (3.14)) can take two different values depending on the sign of h and k. Hence the signs of h and k have now also an influence on the q_p position. If both have the same sign the peak is shifted to the left, while for opposite signs the peak is shifted to the right. Also the q_z position depends on the signs of both indices now. Therefore the peaks $\pm h, \pm k, l$ are observed at four different positions. This is demonstrated by the $\pm 1, \pm 2, 3$ peaks in Fig. 3.1(b).

3.2. Regridding

Regridding is the task of interpolating data measured on a scattered grid onto a rectangular one. There are two important reasons for regridding:

1. **Visualization** of data with two-dimensional pseudo color plots in python is far more efficient if data on a regular grid is present. This fact poses a quite severe requirement to the algorithm. Because each time data is drawn it has to be regridded and hence an efficient algorithm for this task is necessary.

2. **Extraction of line-scans** (one-dimensional data) is only easily possible if the rows and columns of the intensity data matrix share one common coordinate; i.e. all data points in a row should belong to the same y-coordinate, and all points in a column to the same x-coordinate. If this prerequisite is met, ranges of data coordinates can easily be mapped to index ranges of the data matrix.

Unfortunately no library function exists in python which meets the performance requirements and hence a custom one had to be implemented. In the following the used regridding algorithm will be described in detail. There are two major points to address:

1. Estimate the supporting point spacings (dx_i, dy_i) for the regridded grid, and

2. interpolate original intensity data to the new supporting points.

ad 1.) To estimate the new supporting point positions the original data is analyzed. For each row of the original matrix (points connected by grey lines in Fig. 3.2(a)) the x-distances are calculated. The same is done for each column (points connected by black lines in Fig. 3.2(a)) to calculate the y-distances. The new x-distances (dx_i) and y-distances (dy_i) are then chosen to the maximum of all the observed dx and dy. Please note, this way of estimating only works well if the deviation from a rectangular grid is not too large. For grazing incidence X-ray data in the introduced geometries, and on commonly used scan ranges these restrictions do not serve any problem. But if the data is for example transformed to polar coordinates the estimation of new supporting points fails (a too fine grid is created). The only possibility to regrid in this case is to export the data, and try to interpolate the data externally and re-import the data.

ad 2.) When the grid of new supporting points is found, the intensity data $I(x, y)$ has to be interpolated to the new grid $I(x_i, y_i)$. This is done by simply calculating the mean of all the intensities contained within a rectangle around (x_i, y_i) with lower left point $(x_i - dx_i/2.0, y_i - dy_i/2.0)$ and upper right point $(x_i + dx_i/2.0, y_i + dy_i/2.0)$. These rectangles are shown as black lines in Fig. 3.2(b) and their midpoints (x_i, y_i) as black crosses.

In the first step it has to be figured out to which rectangle an original intensity value belongs to. For each point (x, y) the x- (n_0) and y-distance (m_0) to the first point of the new grid (x_i, y_i) is calculated in multiples of $dx_i/2.0$ and $dy_i/2.0$. Then they are rounded down to get an integer

$$n_0 = \lfloor \frac{x - \min(x_i)}{dx_i/2} \rfloor \quad \Rightarrow n_0 \in \mathbb{N}, \tag{3.18}$$

$$m_0 = \lfloor \frac{y - \min(y_i)}{dy_i/2} \rfloor \quad \Rightarrow m_0 \in \mathbb{N}. \tag{3.19}$$

All odd values of n_0 (m_0) correspond to the left (lower) part in a rectangle and the even ones to the right (upper) part. But what is needed, are the indices (m, n) of the centers of the rectangles. That is, the position to which the intensity value belongs to in the new intensity matrix. These indices are found by adding one to all the odd values and divide by two

$$n = \frac{n_0 + n_0\%2}{2}, \tag{3.20}$$

$$m = \frac{m_0 + m_0\%2}{2}. \tag{3.21}$$

Finally the intensity at one point is estimated as the arithmetic mean of all points sharing the same matrix indices (m, n)

$$I(m, n) = \frac{1}{N} \sum^{N} I_n(m, n). \tag{3.22}$$

The according standard deviation (σ_{I_n}) is with assumption of a Poisson distribution for the original intensity data (i.e. $\sigma_{I_n}^2 = I_n$)

$$\sigma_I^2 = \frac{1}{N} \sum_{i=1}^{N} \sigma_{I_n}^2 = \frac{1}{N} \sum_{i=1}^{N} I_n = \frac{1}{N} I. \tag{3.23}$$

$$\sigma_I = \frac{1}{\sqrt{N}} \sqrt{I} \tag{3.24}$$

The advantage of this approach is, that the indices can be computed with the use of the internal matrix operations, which are quite efficient. Only the last step, looping over all data points and calculating the mean intensity for each $I(m, n)$ is

time critical. Therefore this last part has been implemented as c-extension module, which leads to a speed up of approximately 6 times compared to the loop written in python. Unfortunately plattform independency is reduced through this step, but if the c-extension cannot be used the program falls back to the python implementation. Another advantage of this algorithm is, that neighboring data points in the new intensity matrix remain uncorrelated. Regarding the error on the position of data points introduced through regridding it is recognized that the position is maximally $dx_i/2.0$, $dy_i/2.0$ off.

It was outlined above that in PyGid data is regridded each time it is visualized (if necessary). It is pointed out, that this is done on the fly for visualization, and that original data is not changed. The data is only manipulated if the user actively regrids the data.

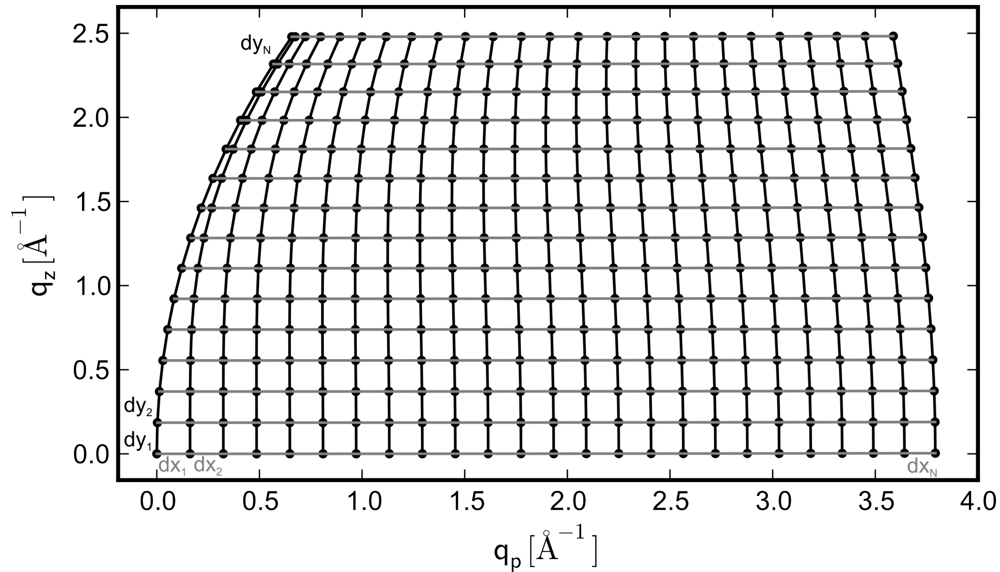

(a) Supporting points after transformation to q. The black lines connect points of one column while the grey lines connect points of one row.

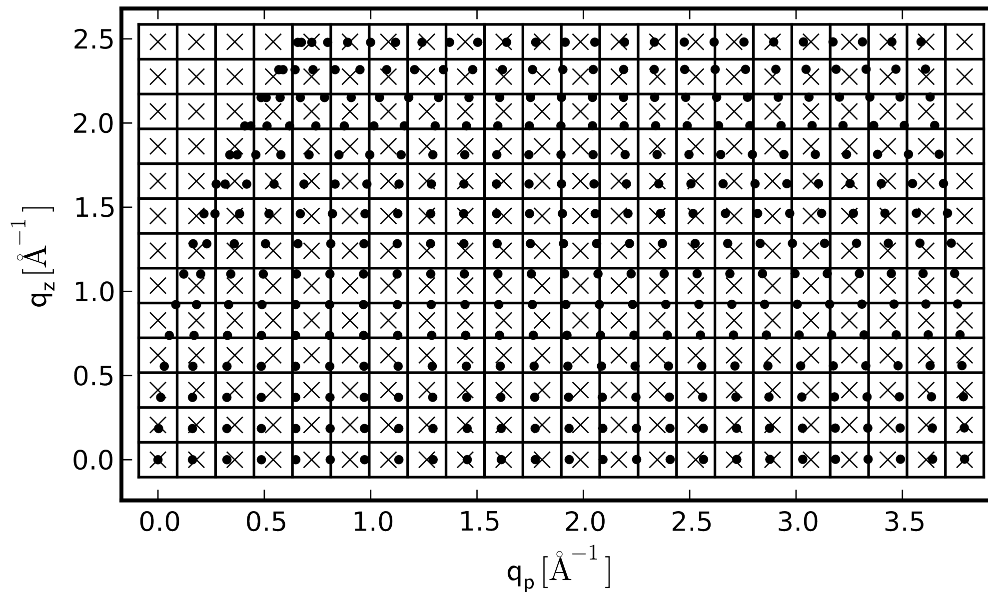

(b) Regridding of supporting points after transformation to q. The black points show original data points, the crosses the new supporting points on the regular grid. All data points in a rectangle are assigned to the same new supporting point.

Figure 3.2.: Regridding

3.3. Correction for Attenuator

Due to limited maximum count rates a detector can withstand it might be necessary to use an attenuator to decrease the beam intensity. Conventionally the attenuation is realized by introducing some absorbing material – frequently aluminum – into the primary beam. To tune the attenuation the thickness of the absorber can be changed linearly in discrete steps $d = kL$ ($k = 0, 1, 2, \ldots$). This decreases the measured intensity (I_k) according to a power law, and the corrected value I is obtained through

$$I = I_k \cdot a^{kL} = I_k \cdot \left(a^L\right)^k = I_k \cdot A^k. \tag{3.25}$$

a is the attenuation coefficient of the used material. In the following A (the attenuation of the material with specific thickness L) will be called attenuation factor.

The value of A can be determined by simply counting photons I_k for some time at a point for two different values of k where this can be without harming the detector. The attenuation factor is then with $I_k = I \cdot A^{-k}$

$$\frac{I_k}{I_{k+1}} = \frac{IA^{-k}}{IA^{-k-1}} = A. \tag{3.26}$$

Of course a more reliable value is obtained if I_k is measured for more than two k and A calculated by least squares fitting A to Eq. (3.25) (or just take the arithmetic mean of several measurements for different k and $k+1$).

Tab. 3.1 shows example data measured at the W1 beamline at Hasylab. The value for A is obtained by fitting the attenuator value to the absolute factor A^k (Fig. 3.3). In this example the value obtained for A was 8.6[1].

The standard deviation of an attenuation corrected intensity value ($I = A^k I_k$) is obtained by scaling the standard deviation (σ_{I_k}) of the measured intensity (I_k)

$$\sigma_I = A^k \sigma_{I_k} = A^k \sqrt{I_k}. \tag{3.27}$$

For the use of PyGid the value of k has to be accessible from the data file (selected by the appropriate counter); the value of A has to be determined and accessible via the `Att factor` box.

3.4. Correction for Monitor

Due to the changing primary beam intensity on a synchrotron the measured, scattered intensity (I_m) has to be set in relation to the primary beam intensity (I_0) which is measured by a beam monitor

$$I = I_m / I_0. \tag{3.28}$$

In PyGid this is done by selecting the counter under which name the monitor data is stored in the data file. If the monitor counts are very large ($I_m << I_0$) this might

[1] Note, that at the W1 beamline not the value of k but 28 times this value is contained within the data files. Hence one has to put $A^{1/28} = 1.08$ into the attenuator box of PyGid.

Table 3.1.: Data used for determination of the attenuation factor. At the detector angle 2θ the intensity was measured. k is the level of attenuation. A^k the absolute correction factor for the specific k. $A(k, k+1)$ gives the relative correction factors for the two specific values of k. The value of A can be calculated as arithmetic mean of the $A(k, k+1)$ or by fitting using column 2 (x) and 4 (y).

2θ	k (x)	Intensity	A^k (y)	$A(k, k+1)$
0.18	3	$3.2 \cdot 10^6$	630.84	7.66
0.18	2	$24.5 \cdot 10^6$		
0.21	2	$3.5 \cdot 10^6$	82.36	9.06
0.21	1	$31.7 \cdot 10^6$		
0.35	1	$3.2 \cdot 10^4$	9.09	9.09
0.35	0	$29.1 \cdot 10^4$	1	

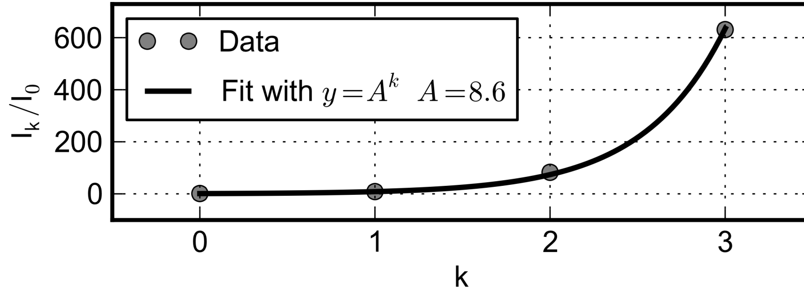

Figure 3.3.: Plot of the example data of Tab. 3.1 and fit for the determination of the attenuation factor.

lead to very small values of I and arithmetic underflows can occur. Therefore it might be of advantage to scale the measured intensity by S values before dividing it by I_0

$$I = \frac{I_m \cdot S}{I_0}. \tag{3.29}$$

In PyGid the scaling factor S is entered in the box labeled `Mul before moni`.

Of course the monitor has also an effect on the intensity error. Again the proper error is obtained by scaling the error of the actually measured intensity

$$\sigma_I = \frac{S}{I_0}\sigma_{I_m} = \frac{S}{I_0}\sqrt{I_m}. \tag{3.30}$$

This last correction of the intensity error can be omitted if S is chosen equal to the mean primary intensity during one scan; then the factor S/I_0 is approximately unity and the effects on the error are small.

3.5. Extraction of Line Scans

For a better insight on some aspects of reciprocal space map data it is often desired to extract one dimensional data (*line scans*). If intensity data is extracted from a rectangular grid, then each intensity point represents the same area in the reciprocal space map. Hence simply summing the intensities is a proportional estimation of the integral.

Due to the Poisson distribution the variance on each intensity value of the line scan ($I = \sum_{n=1}^{N} I_n$) can be estimated (with $\sigma_{I_n} = \sqrt{I_n}$),

$$\sigma_I^2 = \sum_{n=1}^{N} \sigma_{I_n}^2 = \sum_{n=1}^{N} I_n = I. \tag{3.31}$$

That is, the error on the sum of Poisson distributed variables is again Poisson distributed and the conventional equation for the variance is valid.

3.6. Error on Intensity Data

In general, intensity data is distributed according to counting statistics. I.e. according to the Poisson distribution. Hence, the standard deviation σ_I on one data point is

$$\sigma_I = \sqrt{I}. \tag{3.32}$$

The effects of operations like regridding, attenuator correction, monitor correction, and extraction of line scans on the error have been deduced above, here they are summarized. I_m represents the measured value of the intensity.

The standard deviation of:

1. **Regridded data** is $\sigma_I = \frac{1}{\sqrt{N}} \sqrt{\sum_n^N I_{m,n}}$.
2. **Attenuator corrected** data is $\sigma_I = A^k \sqrt{I_m}$.
3. **Monitor corrected** data is $\sigma_I = \frac{S}{I_0} \sqrt{I_m}$.
4. A data point in a **line scan** is $\sigma_I = \sqrt{\sum^N I_n} = \sqrt{I}$

Taking these effects into account is important if one wants to make use of quality parameters obtained by χ^2-fitting. E.g. the quality of peak fits of line scan data or subsequently the quality of crystal structure solutions. Of course all systematic errors have to be eliminated before.

For the structure determination of perfluoropentacene on graphite (discussed in Chap. 4) the intensity error was estimated as outlined. This was done outside of PyGid to test if a quality estimation is possible. During this test indication was found that the data is dominated by systematic errors and therefore error analysis capabilities were not implemented in PyGid. But it is desirable for the future to minimize systematic errors and establish an error estimation.

Part II.

Results

4. Structure Solution of Thin Film Phases

Thin films of organic molecules are key elements for organic electronics. The physical properties of organic thin film devices are strongly influenced by the structure and morphology of the deposited material (Nabok et al.; 2007). Structure and morphology in turn depend sensitively on the preparation conditions (Yagi et al.; 2004; Wu et al.; 2007), like e.g. type and temperature of the substrate (Dinelli et al.; 2004; Stadlober et al.; 2006) (see also Chap. 5). Depending on these parameters thin-film phases might form, which are phases whether observed in single crystals nor in powders. Therefore, the standard crystal structure solution procedures – based on powder or single crystal diffraction – cannot be applied for these systems.

In the following an experimental approach to the crystal structure determination of thin organic films, deposited as two-dimensional powders, will be introduced. The procedure is based on the extraction of structure factors from reciprocal space maps. Then the molecular packing is obtained by a direct space search (see Sec. 1.6.2). There, the misfit

$$\chi^2 = \sum_i \frac{(|F_{\mathrm{obs}_i}|^2 - |F_{\mathrm{calc}_i}|^2)^2}{\sigma^2_{F_{\mathrm{obs}_i}}} \tag{4.1}$$

between observed F_{obs} and calculated F_{calc} structure factors is minimized.

This new approach will be tested with three different materials. To cross check the solutions will be compared to solutions obtained by packing optimizations based on energy considerations.

Strategy

1. **Indexation** to find a proper unit cell for the investigated material.
2. **Extract intensities** from the reciprocal space map.
3. **Calculate observed structure factors** by applying the correction factors from Sec. 2.7.1 to the intensities.
4. **Structure optimization** based on extracted structure factors using rigid body refinement with the software FOX (Favre-Nicolin and Černý; 2002).
5. **Recheck** solution against measured pattern.
6. If necessary introduce **additional information** to the optimization procedure.
7. **Redo** steps 4, 5, and 6 until a satisfactory solution is found or none seems feasible.

4.1. Test Case Pentacene

4.1.1. Indexation

Finding the indexation of pentacene was not necessary because the thin-film phase unit cell was already well known with $a = 5.92$, $b = 7.54$, $c = 15.63$, $\alpha = 81.5$, $\beta = 87.2$, and $\gamma = 89.9$ (Nabok et al.; 2007; Yoshida et al.; 2007; Schiefer et al.; 2007). The reciprocal space map used for the structure solution is shown in Fig. 4.1. In this map the grey dots show all Bragg peak positions in the investigated region, which are expected from the thin-film phase. If they actually show intensity, i.e. are observable, is not considered. Due to limitations during intensity extraction (see below Sec. 4.1.2) only the peaks marked in white could be used for the structure solution.

Peaks not marked by dots are stemming from the bulk phase and are not analyzed.

4.1.2. Extraction of Intensities

In the reciprocal space map the peaks are quite broad along the q_z direction, and are overlapping. Due to the overlaps the peaks could not be fitted individually; therefore line scans along the q_z direction have been extracted, and multiple peak fits were executed (see Fig. 4.2). Please note, that some peaks overlap so strongly that it is not clear to which index the intensity should be assigned. Therefore they cannot be used for structure solution. This is demonstrated by the second peak ($q_z \approx 0.2$) in Fig. 4.2(a). This peak corresponds to the two lowest grey indexation dots in the dashed rectangle in the reciprocal space map. To explain the line scan well these overlapping peaks have been fitted but their intensities ignored for structure solution.

A second class of peaks which might not be used for the structure solution are peaks located directly at, or near to the critical angle of total reflection. There the intensity is enhanced due to the transmission function and $I_m = I \cdot |T_f|^2$ is measured (Sec. 2.6). The transmission function as function of q/q_c near to q_c is shown in Fig. 4.3(a). For values of $q \gtrsim 3q_c$ the influence of the transmission function is below 5%. So, for peaks with $q_z < 3q_c$ one may consider to correct the intensity for the transmission function, or ignore it (e.g. the first peak in Fig. 4.2(a)). In the present case no correction was performed, and three low-$\mathbf{q}$ peaks (Fig. 4.1) were still used for the structure solution. However, for enhancing the quality of structure solutions the influence of the transmission function should be taken into account in the future.

Yet, there is another requirement to satisfy. Extracting correct (relative) intensities from two-dimensional space maps is only possible if the sample is a good two-dimensional powder, i.e. the crystallites have to be indeed randomly rotated around the surface normal. Otherwise an in-plane texture exists, which has an influence on the intensities. I.e. the intensities depend not solely on the crystallographic packing but also on the texture (the investigated pentacene sample proved to be a good two-dimensional powder).

Finally, to determine intensities rod scans (like in Fig. 4.2) have been extracted from the whole map (each one from an equivalent area). Next to each rod a reference background (also representing the same area) was extracted additionally.

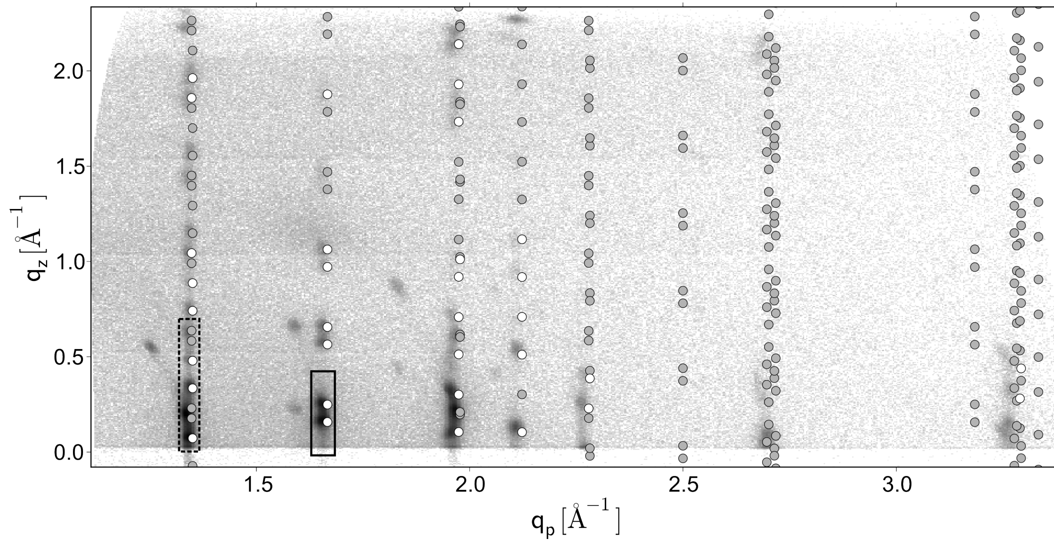

Figure 4.1.: Reciprocal space map of pentacene. The grey dots give all expected Bragg peak positions in the investigated region. The white dots show which peaks have been actually used for the crystal structure solution.

It was found that the background along each rod is constant, and therefore the line scans have been fitted by a sum of Gaussian peaks plus a constant background. This model described most of the line scans satisfactorily, only some would have been described better by another peak shape (e.g. Fig. 4.2(a)). As already mentioned it is not easily possible to estimate the quality of a fit via statistical methods, because the conditions for χ^2-fitting are poorly met. Hence it cannot be decided which model is the most likely one. Finally it was decided not to use different peak shapes for different line scans, and all peaks have been fitted by Gaussians.

After fitting, the area of each (reliably fitted) peak was used as a measure for its intensity. Please note, that areas are a better measure for the peak intensity than the peak height because they are less susceptible to statistical fluctuations (Birkholz; 2006). Furthermore, the peak heights depend on the incidence angle of the radiation on the detector, while the areas do not (See Sec. 2.3).

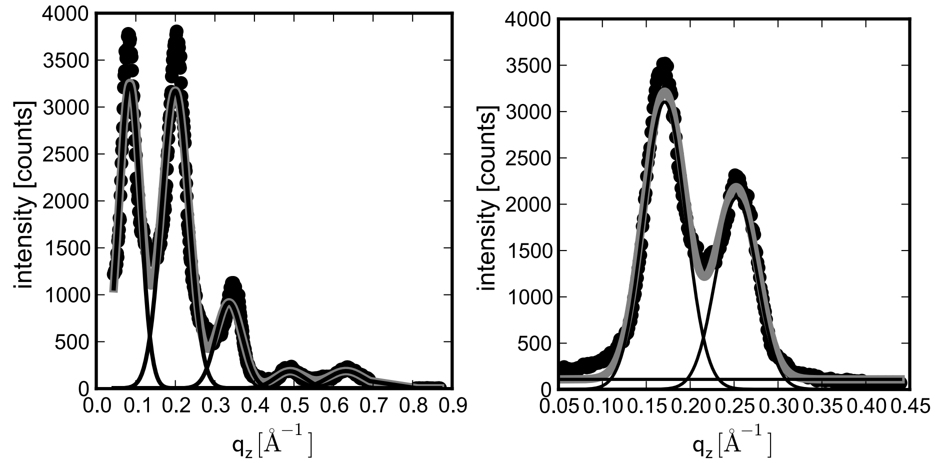

(a) Line scan along q_z of the region contained within the dashed rectangle in Fig. 4.1.

(b) Line scan along q_z of the region contained within the full rectangle in Fig. 4.1.

Figure 4.2.: Vertical line scans extracted from the data in Fig. 4.1. The black dots show the data points, the black lines the individual fit functions (Gaussian peaks and a constant background has been fitted). The grey line shows the sum of all the individual fit functions.

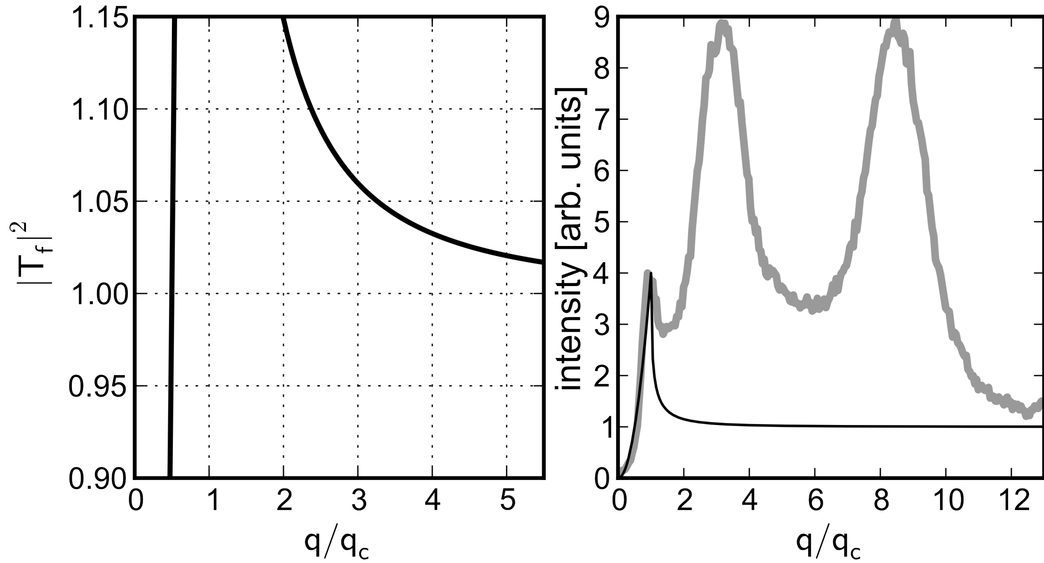

(a) The squared transmission function around the critical scattering vector q_c.

(b) Course of the transmission function together with the first two peaks of Fig. 4.2(a). Please note that the intensity has been scaled to fit the magnitude of the transmission function at q_c.

Figure 4.3.: Transmission function as function of q/q_c.

4.1.3. Correction of Intensities

To obtain structure factors the extracted areas are corrected (as described in Sec. 2.7.1) according to their positions in the sample coordinate system which are calculated from the known indexation (Eq. 2.6, Fig. 2.16).

4.1.4. Structure Optimization

The gained structure factors can now be used within any crystal structure solution software which is capable of finding a crystal structure by fitting a list of structure factors. In the present case, the software FOX by Favre-Nicolin and Černý (2002) was used. FOX is a relatively easy-to-use software built around a parallel tempering minimization algorithm performing trials in direct space, and is freely available. Furthermore, it is capable of treating the individual molecules as rigid body. Due to the generally low quality of the obtained data and the low number of diffraction features, rigid body refinement is the only feasible method for solving crystal structures from grazing incidence X-ray data of organic molecules.

To perform (rigid body) minimization with FOX one needs as input the conformation of the molecule (here taken from the single crystal solution by Campbell et al. (1962)), the unit cell, and a list assigning structure factors to hkl-triplets. The number of molecules within the unit cell has to be specified, and can generally be estimated from mass density considerations. If known also the proper space group can be given, but due to simplicity the test was performed with the space group set to P1. Two molecules have been put into the unit cell. The position(s) of the molecule(s) can be either kept fixed or can also be optimized. If the positions are fixed $3N$ parameters (N ... the number of molecules in the cell) are optimized, while for free positions $6N$ parameters are optimized. For pentacene the centers of mass of the two inequivalent molecules within the unit cell have been set to the fractal positions $(0.0, 0.0, 0.0)$ and $(0.5, 0.5, 0.0)$, and kept fixed. Trying to optimize with free molecules did not result in any physically plausible result.

Several Monte Carlo runs consisting of $2 \cdot 10^5$ steps have been executed for random starting configurations. For fixed positions the minimization proofed quite stable and always converged to the same minimum. For free positions several, but not a single meaningful, solutions were found demonstrating the far higher demands to the amount of data and data quality for this sort of problem.

4.1.5. Check Solution

After the refinement the solution is again compared with the reciprocal space map. This is neccessary, because for the refinement only a limited number of peaks – the ones for which intensity could be extracted – are used. Rechecking the data against the map might reveal that for the found packing intensity is expected for peaks where in the experiment no intensity was observed; in this case the solution is not satisfactorily. To improve the quality of the solution this information is then taken into account by

introducing structure factors of zero magnitude into the hkl list and then redoing the optimization.

Figs. 4.4 (a) and (c) show a comparison between the first pentacene solution and the experimental pattern. In the low-**q** region (Fig. 4.4 (a)) two structure factors are expected where no intensity was measured, i.e. the obtained solution shows a significant deviation from the experimental data and is not satisfactorily. Figs. 4.4 (b) and (d) show the comparison for a second solution found with a structure factor list containing a zero structure factor for the two obviously not fitting peaks. Although only two structure factors have been set to zero, the agreement with the data is increased significantly, even in the high-**q** region (Fig. 4.4(d)).

Generally it should be kept in mind, that for a rough structure solution low-**q** peaks are more important than high-**q** peaks. This is because the low-**q** peaks probe the electron density on a large scale while the high **q** peaks are sensitive to electron density variations on smaller scales (e.g. intra molecular features). It is thought that doing refinement on small scales is not justified by the data, but it is not obvious where the limit is.

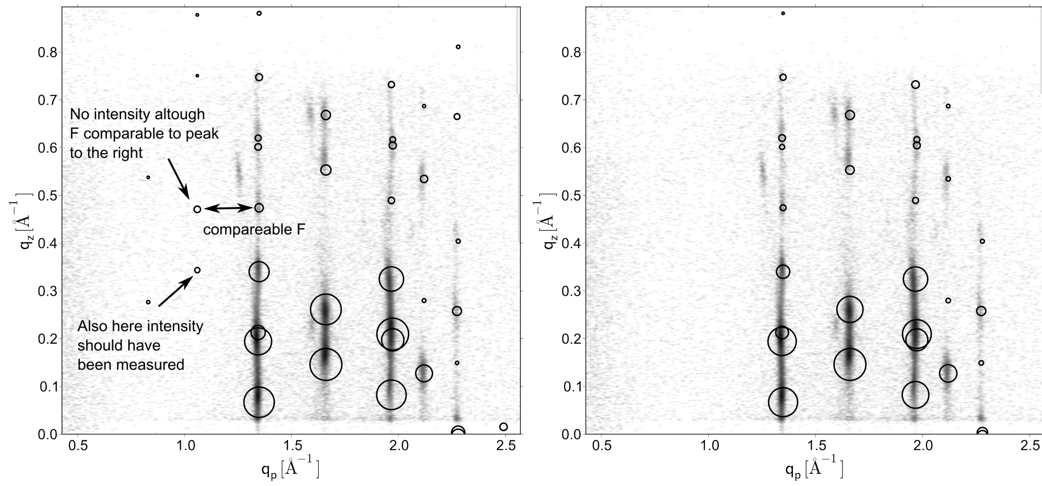

(a) Comparison of first solution in the low-**q** region.

(b) Comparison of solution in the low **q** region after setting the two marked structure factors in map (a) to zero.

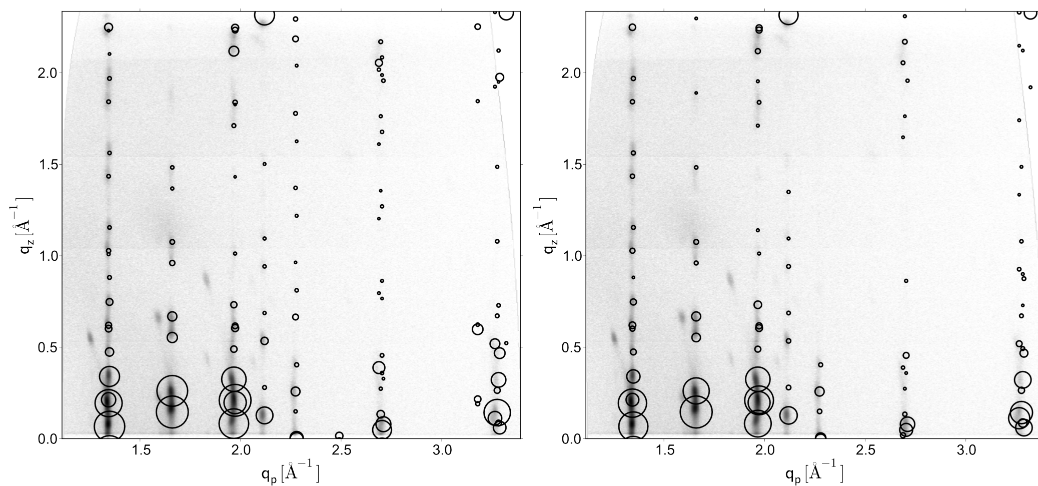

(c) Comparison of first solution in the whole region.

(d) Comparison of solution in the whole region after setting the two marked structure factors in map (a) to zero.

Figure 4.4.: Comparison of solution one ((a) and (c)) and two ((b) and (d)) with the experimental data. The center of the rings correspond to Bragg peak positions while their area is proportional to the structure factor.

Table 4.1.: Molecular orientation of the two obtained solutions compared with two solutions from literature. The herringbone angle is the angle between the surface normals of the two planar molecules in the unit cell. LMA1 and LMA2 are the long molecular axis of each molecule.

	Sol. 1	Sol. 2	Nabok et al. (2007)	Schiefer et al. (2007)
Herringbone angle	53.86°	54.13°	54.96°	54.31°
∠(LMA1,LMA2)	3.30°	0.14°	0.02°	0.63°
∠(LMA1, c*)	7.21°	4.79°	3.01°	5.68°
∠(LMA2, c*)	4.07°	4.83°	3.00°	6.02°

4.1.6. Comparison to Literature Structures

Finally, to estimate the quality of the solution, it is compared to two pentacene thin-film phase solutions found in literature. In particular the angle between the long molecular axes (LMA) of the two molecules within the unit cell, the angle between the LMA and the $\mathbf{c}^*$-direction of each molecule and the *herringbone angle* are compared. The latter is the angle formed by the surface normals of the two independent, planar molecules in the unit cell (a motif quite common for organic rod like molecules).

In Tab. 4.1.6 the parameters for the first solution (Sol. 1) without additional structure factors and for the second one (Sol. 2) with two additional structure factors is compared with the solution by Nabok et al. (2007) and the one by Schiefer et al. (2007). It is recognized that the angle between the two LMAs significantly decreases by introducing the two additional structure factors, and is then for solution 2 very similar to the two literature solutions. The orientations of the individual molecules (∠(LMA1, c*),∠(LMA2, c*)) reveal that mainly the first molecule becomes more upright, while the second one does not really change. On the other side the herringbone angle is quite stable and does not change significantly. To sum up, the second solution seems within an error margin that can be expected for thin film structure solutions.

4.2. Structure Solution of Pentacene Quinone on Silicon Oxide

After the encouraging test of the introduced structure solution approach it was successfully applied to solve the thin-film phase of pentacenequinone (PQ) on silicon-oxide substrates. The results were published in the Journal of Crystal Growth & Design. In this study the surface induced phase of pentacenequinone was also solved by theoretical calculations based on energy considerations and the result agreed well with the experimental solution.

Structure Solution of the 6,13-Pentacenequinone Surface-Induced Polymorph by Combining X-ray Diffraction Reciprocal-Space Mapping and Theoretical Structure Modeling

Ingo Salzmann[1], Dmitrii Nabok[2], Martin Oehzelt[3], Steffen Duhm[1], Armin Moser[4], Georg Heimel[1], Peter Puschnig[2], Claudia Ambrosch-Draxl[2], Jürgen P. Rabe[1], and Norbert Koch[1]

[1]Humboldt-Universität zu Berlin, Department of Physics, Germany
[2]Montanuniversity Leoben, Chair of Atomistic Modelling and Design of Materials, Austria
[3]Johannes Kepler Universität Linz, Department of Experimental Physics, Austria
[4]Graz University of Technology, Institute of Solid State Physics, Austria

Journal of Crystal Growth & Design, **11**, 600–606, (2011)
http://dx.doi.org/10.1021/cg1015143

To further illustrate the task of structure solution here details about this part of the work are given.

The reciprocal space map used for PQ on SiO_x is shown in Fig. 4.5. This map was measured at the W1 beamline of the HASYLAB Synchtrotron source with a point detector. The reciprocal space map could be indexed by Ingo Salzmann with the triclinic unit cell $a = 4.69Å, b = 5.99Å, c = 13.45Å, \alpha = 77.8°, \beta = 84.1°$, and $\gamma = 81.1°$.

For the structure solution the rod scans and backgrounds shown in Fig. 4.5 have been extracted as described in the last section. In contrast to the pentacene data a significant non-constant background is observed. Rather then including it into the fit equations it was stripped from the data prior to fitting. After background removal, the rod scans have been fitted again by a linear combination of Gaussian peaks. Opposite to the pentacene case above all peaks are satisfactorily described by Gaussian peaks.

The rod scan number 4 shows that there is one bad data point at the maximum of the peak; maybe caused by saturation of the detector. For fitting of the line scan this bad data point was ignored.

For structure solution the conformation of the PQ molecule was taken from the

single crystal solution, fixed with center of mass at the origin, and treated as rigid body (only one molecule is contained in the unit cell). The structure solution was performed three times. First for all data, second for data where doubtful fits were stripped (Rod 4 and Rod 7), and third where the strong 1 -1 1 peak was ignored (to exclude the influence of a wrong intensity due to the bad data point). Although the structure refinement has been done for three different data sets it was quite stable and all three runs yielded the same result.

Comparing the structure factors (Fig. 4.6(a)) of the found solution with the experimental data shows, in contrast to pentacene above, no obviously wrong structure factors, and hence no second structure solution run was necessary. Furthermore, the experimental solution (i.e. from extracted intensities) was confirmed by the theoretically obtained one (from energy considerations). A comparison between the measured, the theoretically obtained, and the experimentally fitted structure factors is shown in Fig. 4.6(b).

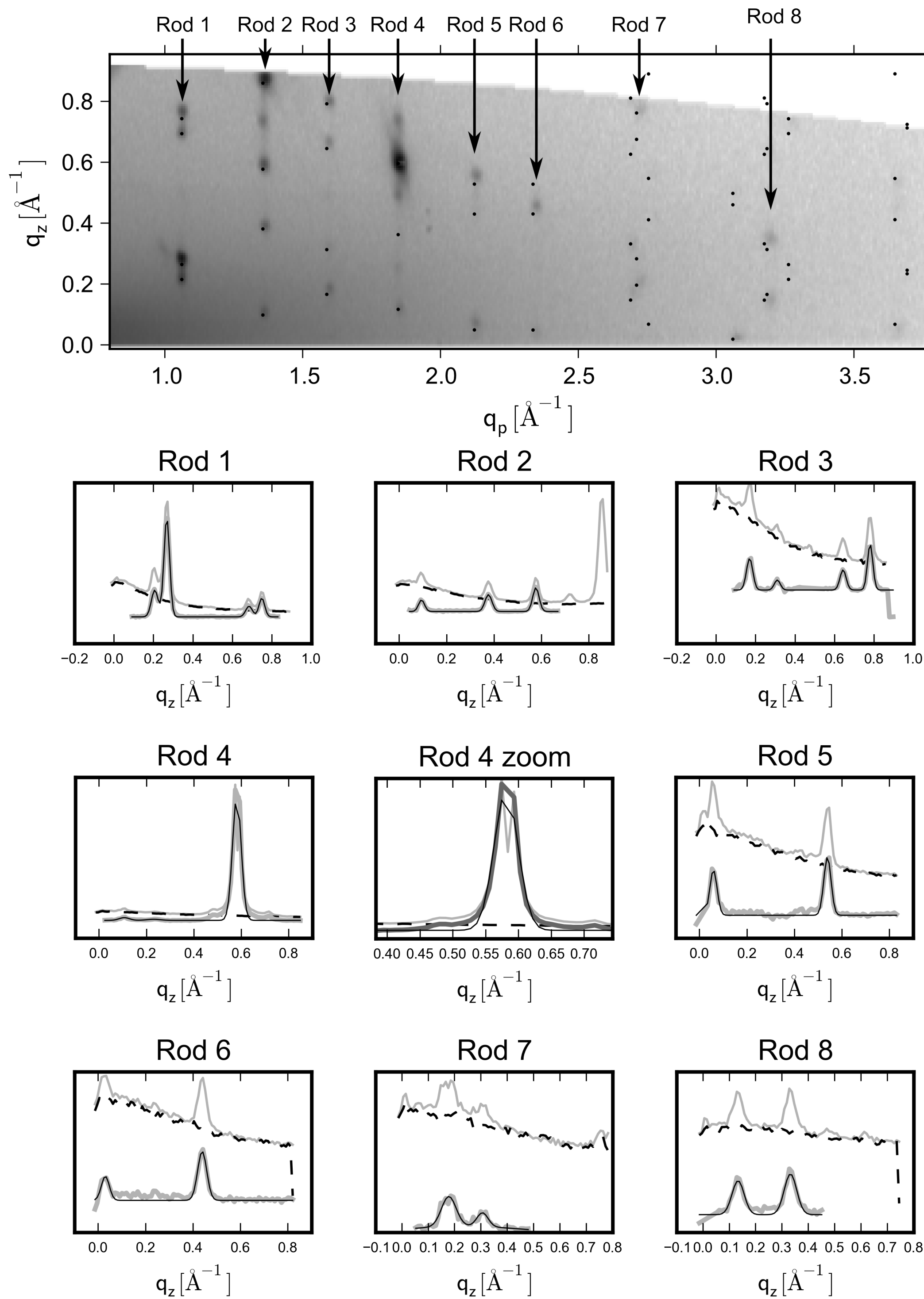

Figure 4.5.: Indexed (black dots) reciprocal space map and extracted rod scans of pentacenequinone. The rod scans show the raw data (light grey line), the background (dashed black line), the background corrected data (dark grey line) and the multiple peak fits (full black line).

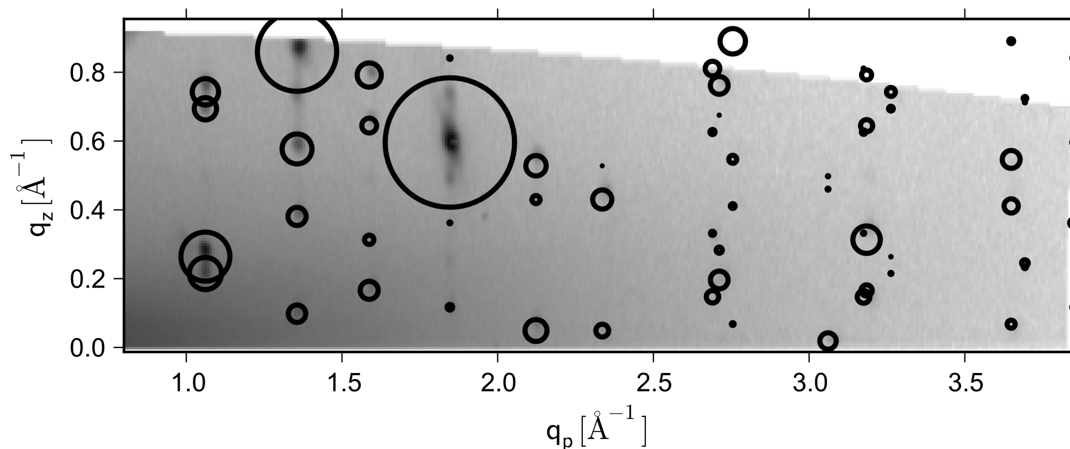

(a) Comparison between the experimentally obtained crystal structure and the measured data. The structure factors ($\propto$ area of the rings) are in good agreement with the data.

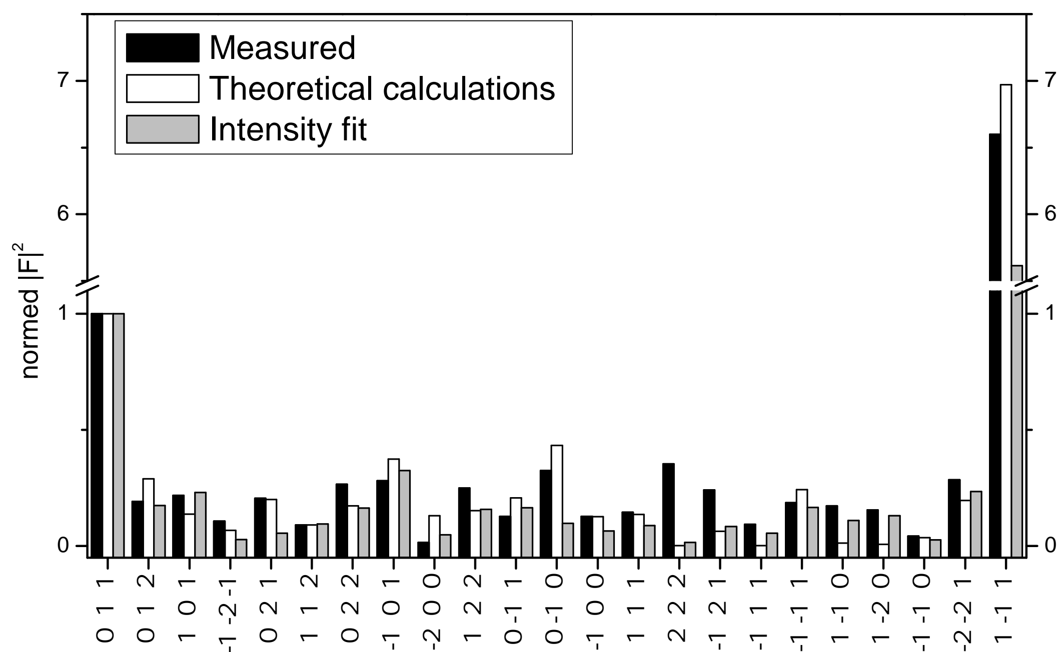

(b) Comparison of measured, theoretically obtained and experimentally fitted structure factors.

Figure 4.6.: Comparison of pentacenequinone structure factors.

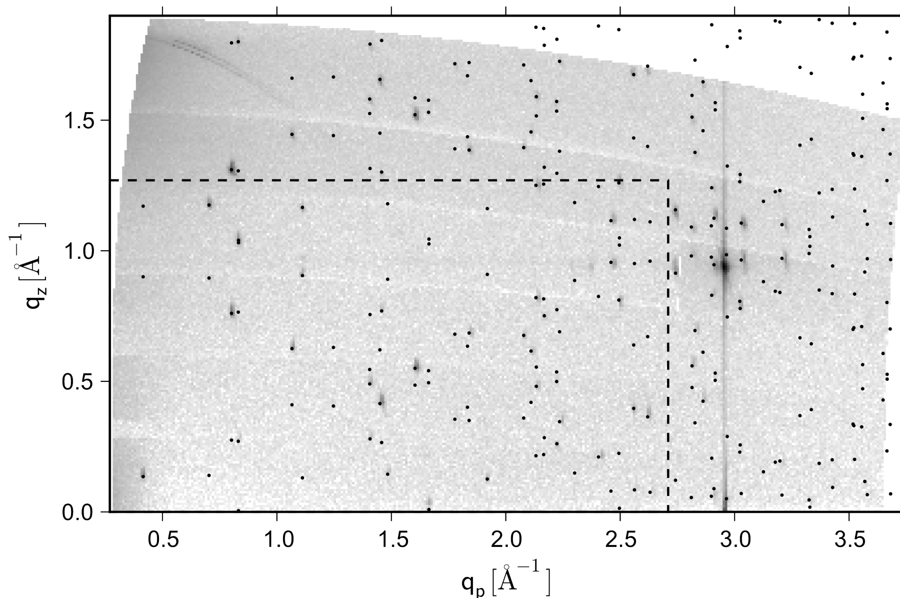

Figure 4.7.: Reciprocal space map of perfluoropentacene on graphite. The black dots show peak positions for the found unit cell. The dashed rectangle encloses the region which was measured in the first experiment with the point detector ($\sim$ 17 peaks are contained in this region).

4.3. Structure Solution of Perfluoropentacene on Graphite

Again in close cooperation with Ingo Salzmann a structure solution of thin films of perfluoropentacene (PFP) on graphite was performed. All the experiments and sample preparations have been executed by Ingo Salzmann or cooperation partners and only the structure optimization was performed by the author of this work. Therefore again mainly details about the structure optimization are given. The complete results of this work are on the way of being published.

Already some time ago first grazing incidence data of PFP have been measured with a point detector for a small region of reciprocal space (Fig. 4.7) and indexed (a = 15.13, b = 8.94000, c = 6.51, α = 78.56, β = 108.14, and γ = 92.44). In the reciprocal space map well defined not overlapping peaks were observed. Because of that no line scans but just the isolated peaks have been extracted and fitted by a Gaussian peak plus a linear background. The area from which intensity was extracted was not kept constant here. This is not crucial if the area of extraction is chosen large enough to contain the complete peak, because then different areas only effect the background (baseline) which is anyway considered during fitting. Due to the limitations of a point detector only a small part of reciprocal space could be mapped, and hence only 17 peak intensities have been measured (Fig. 4.7).

Executing the structure optimization with these 17 structure factors has not provided any meaningful result. For all minima found the two molecules within the unit

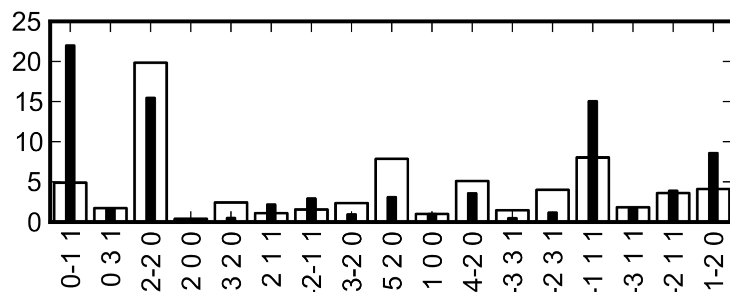

Figure 4.8.: Comparison of the structure factors from the first (black) and the ones from the second (white) experiment. The data of the first experiment was measured for a fixed sample, while it was oscillated around its surface normal during the second experiment.

cell draw too near or even did intersect. To avoid this problem it is possible to set a so called (not well-documented) *anti-bump-parameter* in FOX. Setting this parameter introduces an additional term into the minimized cost function. This term depends on a (minimum) distance parameter which has to be inserted for each possible combination of atoms (Carbon and Fluorine in the present case). The term reaches its maximum for half of the given distance. The anti-bump distances were set to the sum of half the van der Waals radii for all possible combinations of atoms, as it seems a physically plausible choice for molecular crystals. However, although the anti-bump parameter was set, no plausible result was obtained.

Subsequently performed LEED experiments of the substrate showed that the domains of the graphite substrate are azimuthally not random but rather preferred in-plane orientations exist. If the PFP crystallites grow epitaxially on these domains it has to be expected that also the PFP film is not a perfect two-dimensional powder; therefore the prerequisite that no in-plane texture exists is violated. Hence the relative intensities are no more depending solely on the packing but also on this in-plane texture rendering a structure solution impossible.

Because of these findings new scattering experiments have been performed (Fig. 4.7). To avoid the dependence of the intensity on the in-plane texture the sample was oscillated around its surface normal during the measurements. And indeed different intensities than in the first experiment have been measured. Fig. 4.8 compares the structure factors from the first experiment with the ones of the second experiment. Another difference between the two experiments was, that now a one-dimensional detector was available. Thus, a larger region could be measured and 75 intensities extracted.

Also from the new data the peaks have been extracted and fitted individually but looking at the vertical shape of one example peak (Fig. 4.9(a)) reveals a strange peak shape. It is thought that this shape is caused by small misalignments together with the oscillation of the sample. This is why, not vertical but horizontal line scans have been collected and fitted (Fig. 4.9(b)). Unfortunately they have been measured with

P1	P2	DOF	Comment
0,0,0	0,0.5,0.5	75-6 = 69	10 equivalent good solutions, pattern not explained perfectly
0,0,0	0,0.5,0,5	77-6 = 71	7 equivalent good solutions, 3 do not explain pattern
free,0,0	free,0.5,0.5	77-8 = 69	5 equivalent good solutions with arbitrary shift in x, 5 do not explain pattern
0,0,0	0.5,0.5,0.5	75-6 = 69	Pattern not explained
0,0,0	0.5,0.5,0.5	77-6 = 71	Pattern not explained
free,0,0	free,0.5,0.5	75-8 = 67	Pattern not explained
free	free	75-12= 63	Pattern not explained
free	free	77-12= 65	Pattern not explained

Table 4.2.: Parameters for the different settings for the structure solution of PFP. P1 and P2 are the positions of the first and second molecule in the unit cell given with fractal coordinates x,y,z. DOF are the degrees of freedom (i.e. number of structure factors minus fitted parameters).

quite a low resolution and only around 5 data points are contained within the peaks. This is definitely the lower limit for peak fitting.

Nevertheless several structure solution runs were tried. The molecular conformation was again taken from the single crystal solution and two molecules have been placed into the unit cell. The structure optimization was tried for several different settings (Tab. 4.2). For each setting 10 Monte Carlo runs have been performed. For settings with fixed positions $500 \cdot 10^3$ Monte Carlo steps were executed while for settings with free positions $1 \cdot 10^6$ steps were used. In a first step the solution has been executed exclusively with the 75 measured intensities. From the four different settings only the one with the molecules fixed at (0,0,0) and (0,0.5,0.5) gave a plausible result. Similar to the case of pentacene, also here some too strong structure factors have been observed. Therefore, a second run has been performed with two structure factors set to zero; again for all four settings. The second optimization yielded two plausible results. One for fixed molecules as in the first run, one with the x-coordinate left free. But in essence both results where equivalent because the relative positions of the molecules were quite similar, and the shift of the pair of them along the x-direction is due to symmetry not significant.

As in the case of pentacenequinone, energy based packing optimizations were performed as well. Roughly 200 different molecular packings have been obtained and the proper one selected by a comparison with the experimental pattern. The solution fitting best to the experimental pattern agreed well with the experimental one. Fig. 4.10 shows a comparison of both solutions with the experimental data.

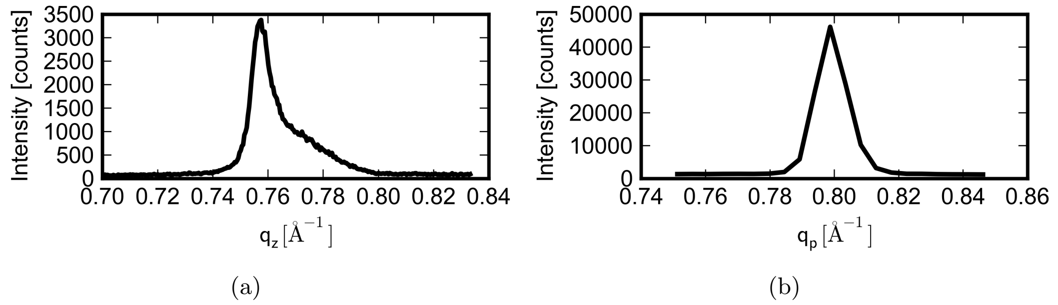

Figure 4.9.: Vertical and horizontal line scan of the -1 1 1 Bragg peak to illustrate the deformed out-of-plane peak shape caused by misalignment in combination with sample oscillation around the substrate surface normal.

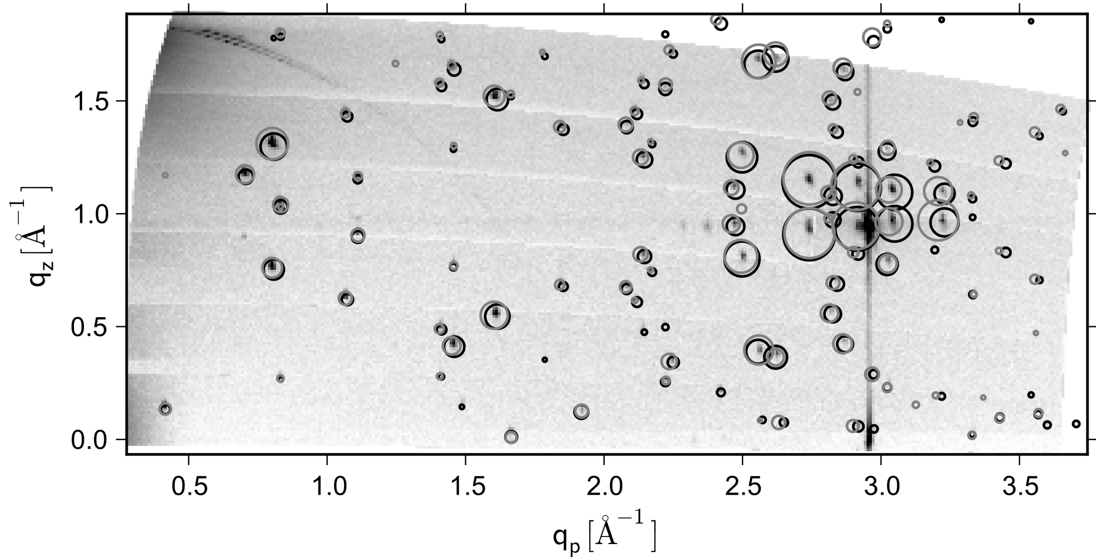

Figure 4.10.: Comparison of the theoretically obtained solution (black) and the experimental one (grey) with the measured data. For the theoretical solution an older not so accurate unit cell was used, hence the peak positions are a little different to the experimental solution, but this has no critical influence on the molecular packing.

4.4. Conclusion

In this chapter three different successful structure solutions of thin-film phases have been shown. While the solution of the PQ phase was quite straight forward and was found without any tweaks, the pentacene and PFP cases have been more challenging. The examples demonstrated that one crucial part is the extraction of the intensities. The second important point is to recheck the found packings against the data, and introduce zero structure factors for non-fitting peaks. At first glance this last step seems somehow artificial; however this is not the case because there is experimental evidence for vanishing structure factors. In cases, where no physically relevant packing is found with the extractable structure factors, one might even think about introducing zero structure factors for peaks which are – according to the indexation – expected, but in the experiment not observed[1]. Another important observed fact is that energetically based packing optimizations seem to be capable to find most of the thin film structures, and that they then generally agree well with experimental solutions. Nevertheless, only by checking the possible plenty solutions against the experimental pattern the proper solution can be selected.

The three examples did also show some

Limitations and Thinkable Enhancements

1. The **peak shapes** did depend on the position of the peak in the reciprocal space map for pentacene and was influenced by the execution of the experiment for PFP. This can be problematic for fitting as a model function has to be selected but might not exist for the observed peak shape. The vertical peak shape observed in the PFP data is an example for this case. Due to the fact that the peaks for PFP have been isolated it might have been possible to estimate the peak area by just summing all data points (of one peak) after a proper baseline correction. On the other side, due to overlaps this would not have been possible for pentacene. In conclusion, depending on the actual data a proper strategy has to be chosen (rod scans, background correction, background fitting, extraction of individual peaks, numerical estimation of peak areas without fitting, etc.).

2. Data containing **heavily overlapping peaks** cannot be used with an approach where individual structure factors have to be measured. An example of a phase which shows plenty of heavily overlapping peaks is the low temperature phase of sexitiophene (Horowitz et al.; 1995). To tackle these problems the only possible way is to perform packing optimizations using rod scans but for this task no software is available. Due to the availibility of the sources it could be possible to implement this functionality into FOX. On the other side there might exist a framework which can do direct space packing optimizations with custom models implemented by the user.

[1] Introducing these structure factors after the first solution process is more efficient because only few obviously non-fitting have to be set to zero. In contrast, a-priori one does not know which structure factors are crucial to be set to zero. Hence, potentially plenty have to be set to zero.

3. The influence of the **transmission function** was ignored.
4. The **reliability of the solution** could not be tested by statistical means because the prerequisites are not met by the data. Furthermore the data might be significantly influenced by **systematic errors** rendering quality estimation even more difficult if not impossible. For a proper estimation of quality it would be necessary to investigate the whole process of structure solution starting from the experiment in close detail.

5. Pentacene on Organic Dielectrics

Crystallization of Pentacene Thin Films on Polymeric Dielectrics

Armin Moser[1], *Heinz-Georg Flesch*[1], *Alfred Neuhold*[1], *Marco Marchl*[1], *Simon J. Ausserlechner*[1], *Matthias Edler*[2], *Thomas Griesser*[2], *Anja Haase*[3], *Detlef-Matthias Smilgies*[4], *Ján Jakabovič*[5],*Roland Resel*[1]

[1]Institute of Solid State Physics, Graz University of Technology, Austria
[2]Institute of Chemistry of Polymeric Materials, University of Leoben, Austria
[3]JOANNEUM RESEARCH, Institute of Nanostructured Materials and Photonics, Austria
[4]CHESS Center, Cornell University, USA
[5]Institute of Electronics and Photonics, Slovak University of Technology, Slovakia

Synthetic Metals, **161**, 2598–2602, (2012)
http://dx.doi.org/10.1016/j.synthmet.2011.09.027

5.1. Abstract

Thin films of pentacene have been deposited on five different organic dielectric layers of three different classes of organic materials: a conventional polymer, a photoreactive polymer and a self assembled monolayer. The morphology and crystallographic properties of the pentacene films were investigated with atomic force microscopy and grazing incidence x-ray diffraction. It is found that the films form well known crystallographic structures but show unusual crystal orientations with respect to the surface. The (0 0 1) lattice plane of the Campbell phase is tilted approximately 13° from the substrate surface normal while tilts between 4° and 7° are observed for the thin film phase. The island shape and density are found to be inhomogeneous on all substrates. In films where mainly large dendritic grains are observed the thin-film phase is the prevalent crystallographic phase while films with a high island density and small irregular grains are dominated by the Campbell phase. It is observed that the mean surface roughnesses and mean surface energies of the substrate play a minor role for the crystallization while the substrate's morphology on nanoscopic scale is crucial for the thin film growth.

5.2. Introduction

Pentacene is one of the most investigated semiconductors in organic thin film transistor (OTFT) research. Like other rod like organic molecules pentacene is very prone to form polymorphic crystallographic phases. There are several known bulk phases (Mattheus et al.; 2001) and one thin-film phase (Yoshida and Sato; 2008; Nabok et al.; 2007; Schiefer et al.; 2007). In thin films commonly a mixture of the thin-film phase and one bulk phase is observed. Up to a critical thickness - which depends on the deposition parameters - the films are dominated by the surface mediated thin-film phase while for thicker films also the bulk phase appears. But it is not excluded that the bulk phase also nucleates directly at the surface (Ruiz et al.; 2004; Mayer et al.; 2006). For OTFT applications it is desired that the pentacene film contains mainly the thin-film phase because it shows superior charge transport properties (Nabok et al.; 2007). Additionally the device parameters are dependent on the dielectric layer used. Frequently a silicon substrate with thermally grown oxide (SiO_x) as gate dielectric is used but with an (additional) organic dielectric layer it is possible to influence the device parameters positively. It is for example possible to tune the threshold voltages as well as the hole mobility of pentacene based OTFT (Yang et al.; 2007; Marchl et al.; 2010a,b). However, these layers change the growth of the pentacene crystallites. Differences in the morphology and crystalline qualities have been reported (Kanjilal et al.; 2007; Ribič et al.; 2009; Yang et al.; 2005).

We have investigated the crystallographic structure and morphology of pentacene thin films deposited on five different organic layers. The main focus is put on crystallographic properties like type of phase, orientation of crystallites and the relation between structure and morphology of the pentacene thin film.

5.3. Experimental Details

Thermally oxidized silicon wafers have been used as substrate for all samples, but different deposition techniques were used for the organic dielectrics. Chemical vapor deposition for the polymer parylene-c, spin-coating for the photo reactive polymer PBHND[1] and self assembled monolayer formation by immersion into solution for the T-SC/SA[2] layer. The chemical structures of the molecules are shown in Fig. 5.1.

5.3.1. Organic Dielectrics

Chemical vapor deposited parylene-c films are grown semi crystalline and pinhole free and form films of homogeneous thickness (Vincze et al.; 2009; Flesch et al.; 2009). Two parylene-c layers of nominally different thicknesses have been prepared and their actual thicknesses and surface roughnesses have been investigated by x-ray reflectivity (XRR) and are given in Tab.5.1. A clear difference in the layer thickness but no

[1] Poly(endo,exo-bis(2-nitrobenzyl)bicyclo[2.2.1]hept-5-ene-2,3-dicarboxylate)

[2] 70% 4-(2-(trichlorosilyl)ethyl)benzene-1-sulfonyl and 30% 4-(2-(trichlorosilyl)ethyl)benzene-1-sulfonic acid

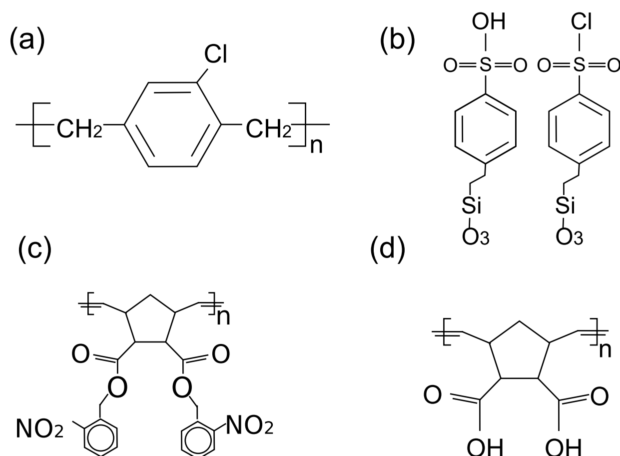

Figure 5.1.: The chemical structures of the used organic dielectric surfaces: **(a)** parylene-c, **(b)** T-SC/SA, **(c)** pristine PBHND, and **(d)** the UV irradiated PBHND

significant surface roughness difference is observed. The surface tension has been determined with a Drop Shape Analysis System DSA 100 (Krüss GmbH Germany) using the contact angles of water and diiodomethane as test liquids. Based on the Owens Wendt method (Owens and Wendt; 1969), the surface tension of the samples as well as the dispersive and polar components have been calculated.

PBHND is a photo reactive polymer synthesized by the procedure given in (Marchl et al.; 2010b). The polymer has been spin coated on thermally oxidized silicon wafers and selected samples were subsequently exposed to UV radiation for 0 min, 1 min and 20 min. Due to this UV illumination the chemical structure changes forming carboxylic acid groups attached to the polymer backbone. XRR investigations of a pristine and a 20 min UV exposed PBHND layer (Tab. 5.1) showed that the UV illumination does not change layer thickness and surface roughness significantly (confirmed by AFM). To investigate the surface energies contact angle measurements have been performed (Marchl et al.; 2010a). Comparing the pristine and the 20 min exposed substrates a decrease of the total surface energy from 47 to 41 mN/m, but an increase of the polarity from 2.6% to 4.2% is found.

The third dielectric layer is a self assembled monolayer produced by immersing a thermally oxidized silicon wafer into a solution containing a mixture of 70% TSC and 30% TSA (Pacher et al.; 2007). XRR thickness, surface roughness and the surface energies are given in Tab. 5.1.

5.3.2. Pentacene Deposition

By physical vapor deposition a nominally 35 nm thick pentacene film was deposited on all substrates. A rate of 0.1 - 0.2 nm/min was used for the first 5 nm and one of 0.5 nm/min for the following 30 nm. This deposition technique results in pentacene thin

	parylene-c		PBHND		
			pris-	20 min	TSC
	No. 1	No. 2	tine	UV	TSA
d / [nm]	23.70	7.50	14.20	12.60	1.70
σ / [nm]	1.20	1.10	0.80	1.00	0.50
γ / [mN/m]	37.91	42.91	47.00	41.00	43.60
γ_d / [mN/m]	36.92	42.42	45.78	39.28	41.4
γ_p / [mN/m]	0.49	0.98	1.22	1.72	2.20
$\frac{\gamma_p}{\gamma}$ / %	1.10	2.60	2.60	4.20	5.30

Table 5.1.: Thicknesses (d) and root mean square surface roughnesses (σ) of the dielectric layers obtained from XRR experiments. Total (γ), dispersive parts (γ_d), and polar parts (γ_p) of the surface energies, as well as polarities (γ_p/γ) of the dielectric layers obtained by contact angle measurements.

films where the crystallites are aligned preferentially with one lattice plane parallel to the substrate surface, but do not show any in-plane alignment. To refer to the orientation of the crystallites it is common practice to give the Miller indices of the surface-parallel lattice plane.

5.3.3. Investigation Techniques

XRR experiments have been performed on a Bruker D8 Discover setup in Bragg Brentano focusing condition using radiation from a copper sealed tube. Wavelength selection ($\mathrm{CuK}_\alpha = 1.542$ Å) was done by a secondary side graphite monochromator. The layer thickness was determined using the recursive algorithm of Parratt (Parratt; 1954) with the information about roughness included in the simulation by the model of Névot and Croce (Névot and Croce; 1980). For the simulation the package WinGIXA is used (Leenaers and de Boer; 1997).

Grazing incidence x-ray diffraction experiments (GIXD) were executed at the G2-Line of the Cornell High Energy Synchrotron Source (CHESS) (Smilgies et al.; 2005), with the wavelength set to 1.301 Å. A position sensitive 1D detector was used to record the scattered intensity, covering an out-of-plane angular range of approximately 8°($\hat{=}$ 0.7 Å^{-1} in q_z). The results of the GIXD experiments are presented as reciprocal space maps (RSM) using the vertical (q_z) and in-plane (q_p) component of the vector of momentum transfer as coordinates. Through indexation of the RSM the crystallographic unit cell and surface-parallel plane are obtained (Moser et al.; 2009).

The AFM system used is a commercial Dimension 3100 by Veeco. The measurements were performed in tapping mode with standard silicon tips by Olympus (AC 160TS). All samples are measured at room temperature and ambient conditions. The scan size is according to the grain size of the pentacene crystals (5 x 5) μm^2.

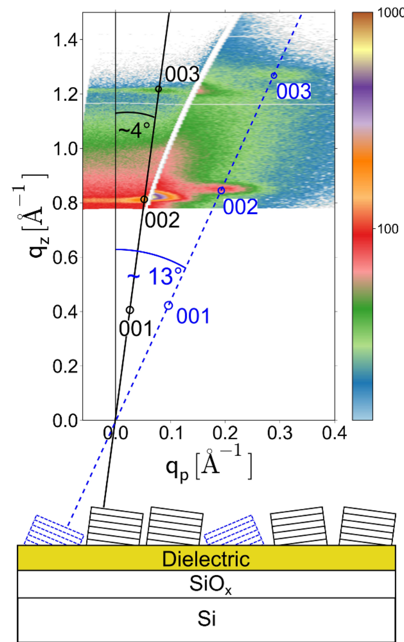

Figure 5.2.: Reciprocal space map of pentacene thin film grown on a parylene-c surface near the specular direction with a logarithmic color scale. The 0 0 L peaks of the thin-film phase (black rings, full line) and of the Campbell phase (blue rings, dashed line) are observed. The radii of the rings are proportional to the expected intensity. In the lower part a sketch of the crystallites on the surface is shown. The (0 0 1) lattice planes the thin-film phase (black, full line) and of the Campbell phase (blue, dashed line) are indicated.

5.4. Experimental Results

5.4.1. Pentacene on Parylene-C

A RSM (Fig. 5.2), measured around the specular direction, shows two distinct Bragg peak series of 0 0 L reflections which can be assigned unambiguously to the thin-film phase and Campbell phase (Yoshida and Sato; 2008; Nabok et al.; 2007; Schiefer et al.; 2007; Campbell et al.; 1961, 1962). Both 0 0 L peak series are clearly tilted from the specular direction revealing that the (0 0 1) planes of the Campbell phase crystallites are tilted approximately 13.0°, and the ones of the thin-film phase 4.0° from the substrate surface normal. For a successful indexation and hence determination of the surface-parallel plane a part of the scattering pattern near to the in-plane direction was measured (Fig. 5.3(a)). This RSM was indexed with the known lattice constants by just changing the surface-parallel planes showing that the thin-film phase grows with the (1 -2 75) plane and the Campbell phase with the (-1 -1 12) plane parallel to the substrate surface which is in agreement with the 4.0° and 13° tilt of the (0 0 1)

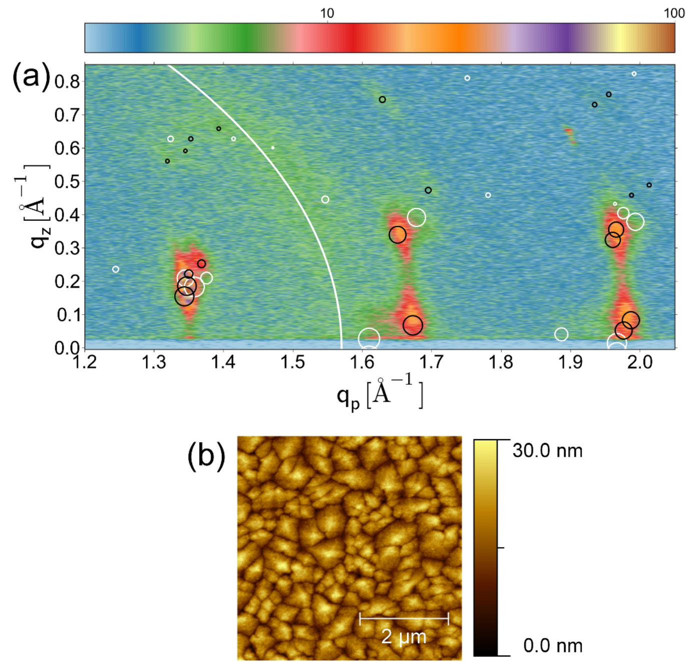

Figure 5.3.: **(a)** In-plane reciprocal space map of pentacene crystallites on the parylene-c surface together with indexation. Calculated peak positions for the thin film (white circles) and Campbell phase (black circles) are plotted on top of the log-scaled intensity pattern. The radii of the circles are proportional to the expected intensity. The 1 1 0 reflection of the parylene-c is drawn as white arc. **(b)** AF micrograph of the corresponding film.

planes. Due to the large peak widths and the resulting overlaps it is not possible to get a reliable quantitative estimate for the relative amount of the phases. But from the known packings of the crystallographic phases expected Bragg peak intensities can be calculated and by comparing these expected intensities to the observed ones one can estimate which phase dominates. This shows that the films on parylene-c are dominated by the thin-film phase. Finally it is noted that on the two parylene-c films with different thickness no differences between the pentacene layers on top of them have been found.

The AF micrograph in Fig. 5.3(b) shows the height image of the investigated film. Several pentacene islands of different shape can be observed showing a higher nucleation density than on silicon oxide (Ruiz et al.; 2004). A coexistence of large pyramidal grains and smaller grains of irregular shape is observed.

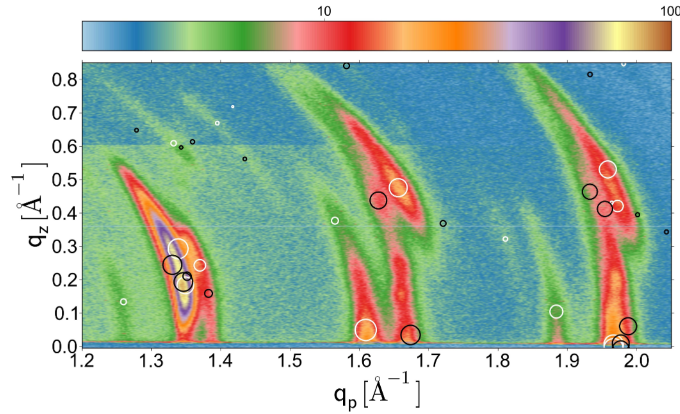

Figure 5.4.: Reciprocal Space Map of pentacene thin film on PBHND which was not exposed to UV. The recorded intensity is given on a logarithmic scale together with indexation. Expected peak positions of the Campbell phase (white circles) and thin film phase are indicated (black circles). The radii of the circles are proportional to the expected intensity. The not indexed peaks are stemming from a (0 0 1) oriented thin-film phase.

5.4.2. Pentacene on PBHND

GIXD and AFM data of pentacene films on differently UV exposed PBHND layers reveal a tremendous influence of the UV induced surface modification on the crystallographic properties and the morphology of the grown film.

The film grown on pristine PBHND contains the thin-film phase and Campbell phase (Fig. 5.4), but in contrast to the films on parylene-c the Campbell phase dominates this film. Additionally a broad crystallite orientation distribution (mosaicity) is revealed by the smearing of the Campbell phase diffraction features along an arc with fixed radius ($|\mathbf{q}|$) in the RSM. The maximum of the distribution (maximal intensity) is observed at a similar tilt angle as on parylene-c; the (0 0 1) lattice plane is tilted 12° from the surface normal with (-1 -1 15) as surface-parallel plane. In contrast the thin film phase shows a clear dominating (0 0 1) orientation and a minor (1 -2 40) orientation indicating a 7° tilt of the (0 0 1) planes. If the PBHND substrate is exposed for only 1 minute to UV radiation (see Sec. 5.8) the mosaicity of the pentacene film is decreased significantly. The thin-film phase dominates these films and two orientations are observed for both phases. Both show a dominating (0 0 1) orientation on the one hand and the same orientations as observed on parylene-c on the other hand. On the sample which was exposed for 20 min to UV (see Sec. 5.8) the mosaicity is further decreased, the thin-film phase dominates, and for both phases exclusively (0 0 1) oriented crystallites are found. This scattering pattern is quite similar to patterns usually observed for pentacene films on SiO_x (Yoshida and Sato; 2008; Nabok et al.; 2007; Schiefer et al.; 2007).

The AFM data (Fig. 5.5) of these films show also a tremendous influence of the

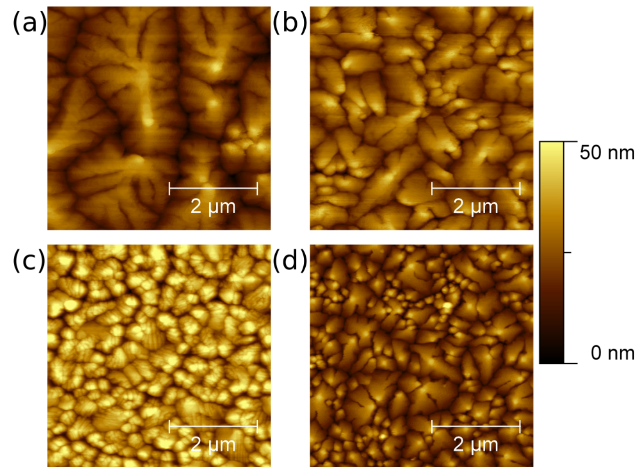

Figure 5.5.: AF micrograph of nominally 35 nm thick pentacene films on PBHND exposed to UV for different time spans - **(a)** 0 min, **(b)** 1 min, and **(c)** 20 min exposed - and of the pentacene film on the T-SC/SA layer **(d)**.

surface modification on the morphology of the pentacene layers. While the pristine sample shows a very high island density of small irregular grains, the sample exposed 20 min to UV shows large dendritic islands as usually observed on SiO_x (Ruiz et al.; 2004). In between these two extremes one finds a gradual change of the island size. The film grown on the one minute exposed substrate shows a medium nucleation density and a coexistence of small irregular and large dendritic grains.

5.4.3. Pentacene on T-SC/SA

The GIXD scattering pattern of pentacene on T-SC/SA (see Sec. 5.8) reveals a dominating thin-film phase with two different orientations. A (0 0 1) orientation and a (1 -2 50) orientation corresponding to a tilt around 5° are observed. In contrast only one orientation is found for the Campbell phase revealing a 13° tilt as on parylene-c.

The AFM data (5.5(d)) show a similar picture as on the 1 min exposed PBHND substrate. A medium nucleation density and coexisting large dendritic and small irregular islands are observed.

5.5. Discussion

The presented data on pentacene thin films grown on top of different dielectric layers show that all the pentacene films are polycrystalline and are composed of two well known crystallographic phases: The thin-film phase and Campbell phase. These phases are also observed on silicon oxide (Nabok et al.; 2007), where they are oriented with their (0 0 1) lattice plane parallel to the substrate surface and large dendritic islands are observed by AFM (Ruiz et al.; 2004). Films with the same morphology

and crystallographic properties have been found here on the 20 min exposed PBHND substrate. In all other cases it was found that the polymeric dielectrics have an influence on the orientation and morphology of the crystallites. Tilted crystallites are found on parylene-c, the pristine and 1 min UV exposed PBHND, and the T-SC/SA surface. Overall it is observed that the thin-film phase shows a higher tendency to form (0 0 1) oriented crystallites than the Campbell phase. To summarize, the dielectrics have an influence on the crystallite orientation while there is no change of the crystallographic structures formed.

The found surface-parallel planes of the tilted crystallites are quite unusual because surface-parallel planes are commonly cleavage planes which is not the case here because the planes intersect the pentacene molecules. There are examples where observations of this kind are explained by twinning effects within the organic film (Resel et al.; 2001; Moret et al.; 2005) but in the present case it was not possible to identify a clear twinning plane neither within one phase nor between different phases.

From the collected data it is also not possible to draw clear conclusions about the role of the surface energies. On PBHND it was observed that the amount of Campbell phase decreases with exposure time to UV and hence with increasing polarity of the substrate. A higher polarity favors 2D growth and therefore might promote the growth of the thin-film phase (Ribič et al.; 2009; Verlaak et al.; 2003). This behavior is not confirmed by the other samples. This shows that on the present dielectrics the surface energies play a minor role.

On surfaces with similar mean surface roughnesses (measured by XRR) different mosaicities and fractions of the two phases are observed, hence the measured roughness cannot be the reason for these observations. This can be explained if one considers that with the resolution of XRR as well as AFM it is not possible to access the nanoscopic morphology; i.e. the morphology on the scale of the pentacene unit cell which is important for the growth (Lee et al.; 2008).

In the AFM images it is also observed that there are local differences in the pentacene growth behavior which can only be caused by locally different surface properties of the substrate. It is remarkable that with the increase of the amount of dendritic grains also the diffraction features from the (0 0 1) oriented thin-film phase are getting more pronounced. This strengthens that the dendritic grains are built of the thin film phase. Dendritic grains are typically formed by diffusion limited aggregation which implies that a molecule can diffuse freely and is immediately included into a grain at the moment it gets into contact with it; i.e. after inclusion into the grain there are no or only few rearrangements expected. We suggest that this growth mechanism favors the formation of the kinetically but not thermodynamically stable thin-film phase. Outside these regions the nanoscopic roughness might influence the growth and lead to piling up of material and the formation of the bulk phase gets more probable there. This is also the reason why the bulk phase shows a stronger tendency to form a large mosaicity.

5.6. Conclusion

In this report it was shown that pentacene thin films grown on selected organic dielectrics show different crystallite orientations as well as different fractions of crystallographic phases than films grown on silicon oxide. The observed behavior cannot be explained by twinning effects, neither within one phase nor between different phases. Also the mean surface roughness as well as the mean surface energies do not play an important role. In general locally different growth behavior is found and reasoned that this is caused by locally different substrate surface properties and especially the morphology on the nanoscopic scale. Pronounced growth of large dendritic grains is found in films which are dominated by the thin film phase while the Campbell phase is prevalently found in films composed of small irregular islands.

5.7. Acknowledgment

The authors thank the Austrian Science Foundation (FWF) for supporting this work within the research project P21094 solution of surface induced crystal structures. The authors also thank Gregor Trimmel from the Institute of Chemistry and Technology of Organic Materials, Graz University of Technology, Austria for supplying material. This work is based upon research conducted at the Cornell High Energy Synchrotron Source (CHESS) which is supported by the NSF and NIH/NIGMS via NSF award DMR-0936384.

5.8. Supporting Informtaion

Figure 5.6 shows a direct comparison of all reciprocal space maps and AFM images. The black indexation shows peaks of the thin-film phase, the white one of the Campbell phase. The not indexed peaks on the 1 min exposed PBHND 5.6(c), the pristine PBHND 5.6(d), and on T-SC/SA 5.6(e) are stemming from an (0 0 1) oriented thin-film phase. Comparing Figure 5.6(d) and 5.6(b) one can recognize the decrease of mosaicity and of the amount of Campbell phase. The decrease of mosaicity follows from the decrease of the width of the peaks along an arc. The decrease of the Campbell phase from the decrease of the intensities of the corresponding diffraction peaks (marked with white circles in both pictures).

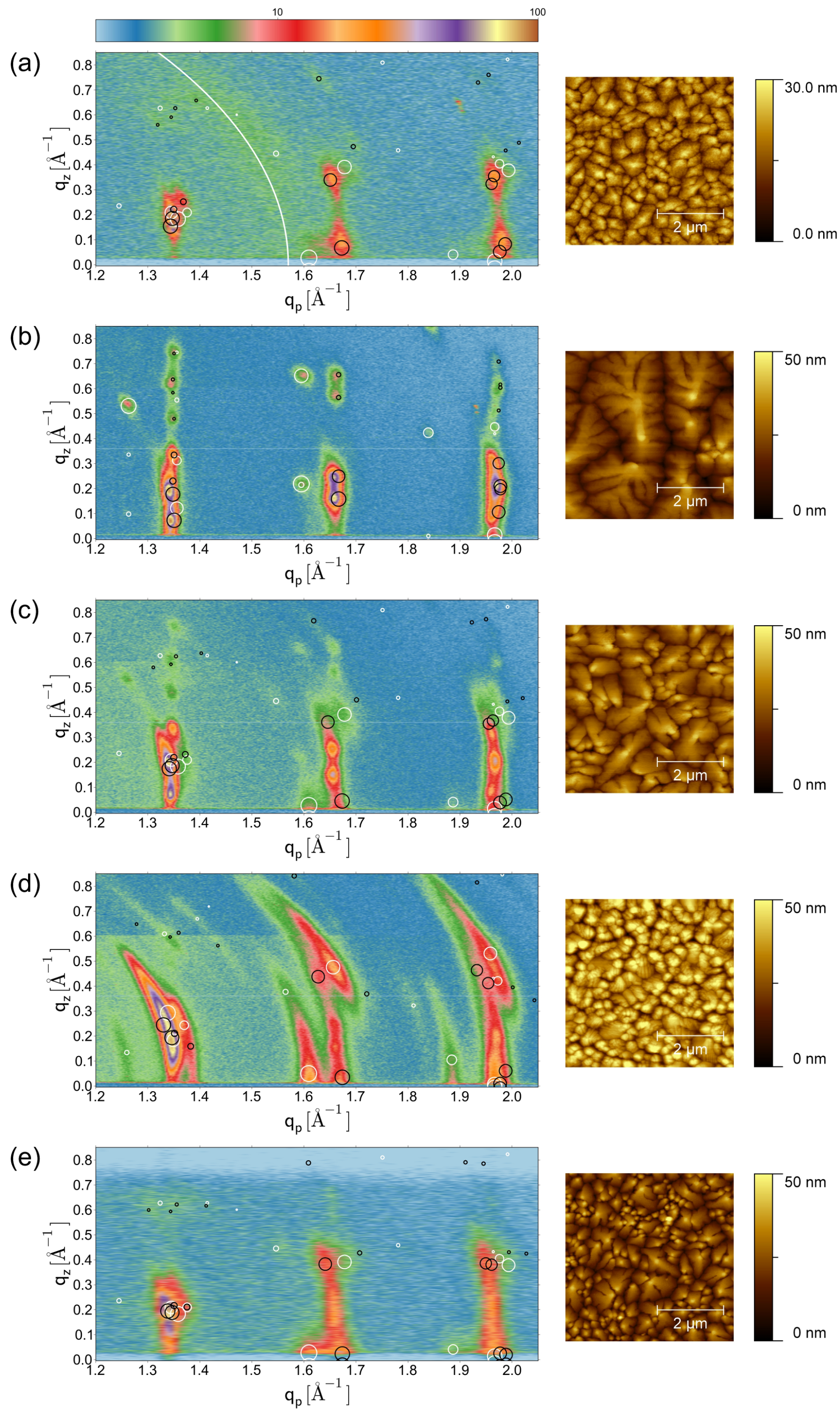

Figure 5.6.: Comparison of all reciprocal space maps and atomic force micrographs. **a)** on 20 nm parylene-c, **b)** on 20 min, **c)** on 1 min, **d)** on pristine PBHND, **e)** on T-SC/SA.

6. Temperature Stability of Pentacene Thin-Films

Temperature Stability of the Pentacene Thin-Film Phase

Armin Moser[1], *Jiří Novák*[1], *Heinz-Georg Flesch*[1], *Tatjana Djuric*[1], *Oliver Werzer*[1], *Anja Haase*[2],*Roland Resel*[1]

[1]Institute of Solid State Physics, Graz University of Technology, Austria
[2]Institute for Surface Technologies and Photonics, Joanneum Research Weiz, Austria

Applied Physics Letters, **99**, 221911–221911-3, (2011)
`http://dx.doi.org/10.1063/1.3665188`

6.1. Abstract

This work presents the influence of temperatures above 300 K on the crystal structure and morphology of pentacene thin films. The thermal expansion of the unit cell and the relative amount of different phases are investigated via grazing incidence x-ray diffraction. Geometrical considerations about the specific molecular packing of the thin-film phase explain the anisotropic non-linear expansion. Furthermore, around 480 K a phase transformation of the thin-film phase to the bulk phase is observed. In contrast only a weak influence of the temperature on the height distribution of the thin-film phase crystallites is found.

6.2. Introduction

Pentacene is a material widely used in organic thin film transistor research where thin films with thicknesses of some tens of nanometers are relevant. Although there are several polymorphic phases of pentacene (Mattheus et al.; 2001) typically only two of them are observed in thin films: the thin-film phase and Campbell phase (Yoshida and Sato; 2008; Nabok et al.; 2007; Schiefer et al.; 2007; Campbell et al.; 1962). While the Campbell phase is a bulk equilibrium structure the thin-film phase is a surface induced, metastable crystallographic phase, which is kinetically favored during the growth process (Dimitrakopoulos et al.; 1996). On weakly interacting substrates (e.g. silicon oxide) the crystallites of both phases are commonly oriented with the (001) lattice plane parallel to the substrate surface; i.e. the a and b unit cell vectors lie in

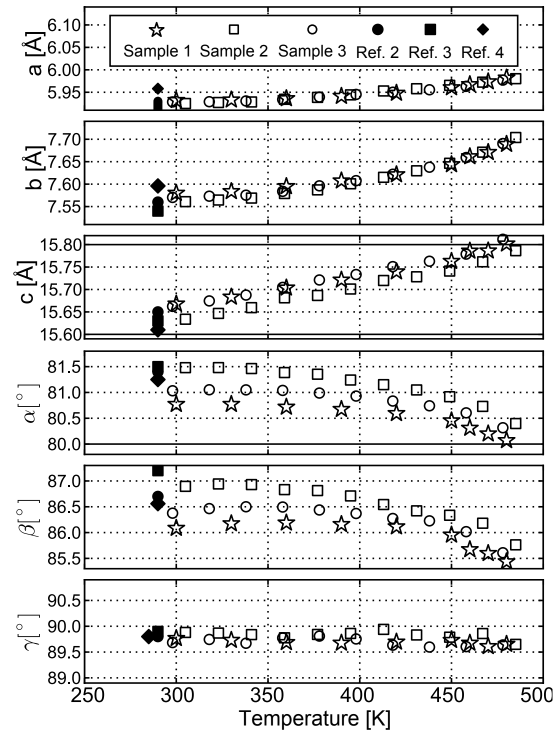

Figure 6.1.: Lattice constants of the pentacene thin-film phase as function of the temperature obtained from three independent diffraction experiments (empty symbols). The literature values at room temperature are given additionally (filled symbols).

the substrate surface plane and the long molecular axis (LMA) is nearly perpendicular onto the substrate surface. Atomic force microscopy (AFM) experiments commonly show terraced, dendritic islands with diameters of some microns (Zhang et al.; 2009; Haas et al.; 2004).

Despite the large number of scientific publications on pentacene thin films, there are only two studies showing some influence of temperatures above 300 K(Ji et al.; 2008; Fukuda et al.; 2009). Moreover they are more focused on device performance than on crystallographic properties. To fill this gap we have thoroughly investigated the crystallographic properties as well as the morphology via specular and grazing incidence x-ray diffraction experiments at temperatures ranging from 300 K up to desorption of the film at around 500 K.

6.3. Experimental Details

Pentacene thin films with a nominal thickness of 50 nm have been physical vapor deposited onto thermally oxidized silicon wafers at a base pressure of 1×10^{-5} mbar; the substrate was kept at room temperature. For the starting 5 nm a rate of 0.1 nm/min while for the remaining ones a rate of 0.6 nm/min was used. AFM experiments were performed on a commercial Dimension 3100 by Veeco with standard silicon tips in tapping mode at ambient conditions and reveal the usually observed morphology. Grazing incidence and specular x-ray diffraction experiments have been performed at the ID10B beamline of the European Synchrotron Radiation Facility. For a wavelength and goniometer independent representation of the data the components of the scattering vector $\mathbf{q}$ in the surface reference frame (Moser et al.; 2009) are used as coordinates. For temperature control and creation of a helium inert atmosphere a Domed Hot Stage 900 (Resel et al.; 2003) from Anton Paar Ltd. was used. To account for the thermal expansion of the heating stage, it was necessary to align the samples at each temperature step.

6.4. Results and Discussion

In the measured reciprocal space maps (RSM) diffraction peaks of the thin-film phase and Campbell phase have been observed. The positions of the Bragg peaks have been used to calculate the unit cell parameters at different temperatures. For the thin-film phase clear thermal shifts of the lattice parameters are observed (depicted in FIG. 6.1). The temperature dependence of the lattice constants a and b is non-linear, in contrast to that of c. Furthermore, the expansion of b (≈ 0.12 Å) is approximately twice that of a (≈ 0.05 Å). This 2:1 ratio of the expansion was also found for the Holmes phase (Holmes et al.; 1999; Mattheus et al.; 2001) under high pressure (Oehzelt et al.; 2006). This observation is typical for the herringbone packing motive and explained by geometrical considerations taking the van der Waals shape of the molecules into account (Oehzelt et al.; 2006). Also the non linearity of the in-plane expansion is caused by the distinct packing of the molecules. The molecules are nearly perpendicular onto

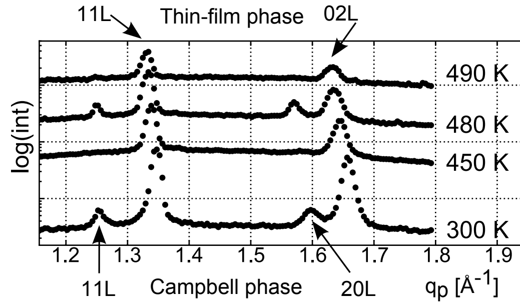

Figure 6.2.: Diffraction patterns at different temperatures as function of the scattering vector component parallel to the substrate surface (q_p). The patterns were obtained by integrating Bragg peak series observed in a reciprocal space map along q_z ranging from 0 to 1.0 Å^{-1}. The observed peaks can be assigned to the thin-film phase (indicated above) and the Campbell phase (indicated below).

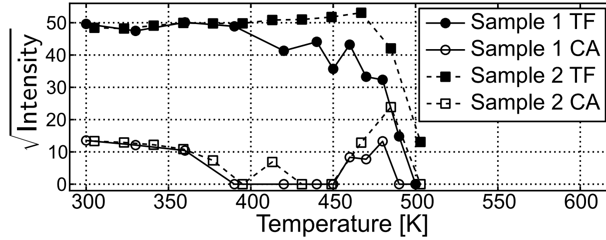

Figure 6.3.: Sum of Bragg peak intensities for the thin-film phase (TF) and for the Campbell (CA) phase which have been extracted from the in-plane scattering patterns. The data for two independent samples are presented.

the (001) plane, and hence the projection of their van der Waals shape to the (001) plane is elliptical. Upon heating librations of the rigid molecules around their LMA play an important role (Haas et al.; 2007). To avoid overlapping caused by the librations the molecules have to shift (non linearly) into a and b direction. In contrast the lattice constant c is nearly parallel to the LMA and the expansion is therefore dominated by translations of the whole molecule. Hence a more linear expansion into this direction is observed. An influence of the substrate is ruled out because the linear expansion coefficient $\left(\frac{1}{L(T_0)}\frac{\Delta L}{\Delta T}\right)$ of amorphous silicon oxide ($\approx 0.5 \cdot 10^{-6} K^{-1}$) (B. El-Kareh; 1994) is two orders of magnitude smaller than the one observed for pentacene ($\approx 1 \cdot 10^{-4} K^{-1}$). In contrast to the thin-film phase no reliable expansion curves could be obtained for the Campbell phase as only five peaks have been observed.

While the unit cell expansion was determined from the Bragg peak positions their intensities were analyzed to investigate quantitative changes of the observed phases during temperature treatment. To perform this analysis the intensities in the RSM have been summed along the q_z direction. From the resulting line scans (see FIG.

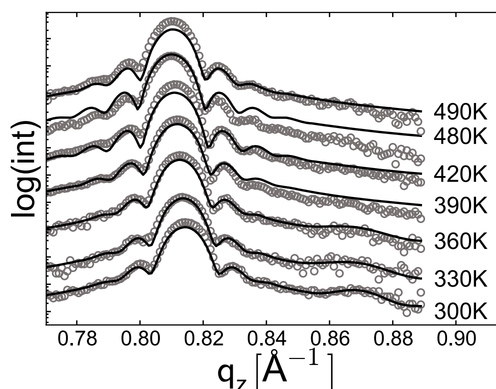

Figure 6.4.: Specular diffraction around the 002 Bragg peak of the thin-film phase ($q_z \approx 0.81$ Å^{-1}) and of the Campbell phase ($q_z \approx 0.87$ Å^{-1}) at different temperatures. The symbols indicate the experimental data while the lines correspond to fits using the model defined in Eq. (6.1)-(6.2)

6.2) the total integrated intensities per phase have been extracted and depicted in FIG. 6.3. At room temperature diffraction features from both phases are present, however upon heating the Campbell phase intensity starts to decrease while the thin-film phase intensity remains constant or even increases slightly. Between 380 K and 450 K no intensity from the Campbell phase is observed, but above 450 K it reappears and reaches a maximum intensity at around 480 K. Above this temperature finally both phases start to desorb and reach zero intensity around 500 K. Contrary, in the specular diffraction data (FIG. 6.4) the peak of the Campbell phase is only observed up to 360 K and the recurrence at 480 K cannot be recognized.

At low temperatures these observations show the vanishing of the Campbell phase while around 480 K a transformation from the thin-film phase to the Campbell phase is observed. When comparing the specular and in-plane data around 480 K it becomes obvious that the reformed Campbell phase crystallites have only a small vertical scattering volume but laterally a large one. In perfect agreement with our findings the AFM images of Ji et al. (Ji et al.; 2008) show thin elongated islands crystallizing on top of the film.

To gain more details about the phase changes and the morphology of the thin films the specular diffraction data has been further analyzed. For this purpose the height of each island is expressed in terms of the number of crystallographic layers N_i. Then the diffraction peak from one phase is described by a weighted sum of the interference functions from individual islands of specific height (Eq. (6.1)). The weights are determined by the island height distribution which has been chosen Gaussian in the present case (Eq. (6.2)) (Nefedov et al.; 1998). Furthermore to account for the two crystallographic phases their diffraction is calculated separately and then added. To perform global optimization the described model was implemented in the software

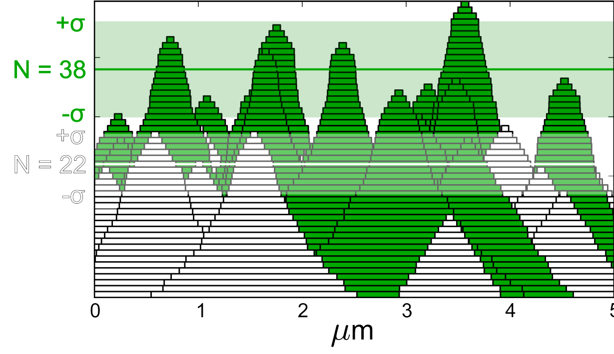

Figure 6.5.: Sketch of the Gaussian height distribution of the pentacene crystallites at 360 K. The filled islands show the thin-film phase while the empty ones correspond to the Campbell phase. The mean island heights (N) are indicated by a horizontal colored and white line. The standard deviation ($\pm\sigma$) areas are shaded. The parameters have been obtained from the corresponding fit of the specular data shown in FIG. 6.4

package GenX (Björck and Andersson; 2007).

$$I = \sum_{N_i=N_{min}}^{N_{max}} w_{N_i} \cdot \frac{\sin^2(N_i/2 \cdot qd_{001})}{\sin^2(1/2 \cdot qd_{001})} \tag{6.1}$$

$$w_{N_i} = \frac{1}{\sqrt{(2\pi)\Delta N^2}} \exp\left(-\frac{(N_i - N)^2}{\Delta N^2}\right) \tag{6.2}$$

For the thin-film phase this analysis revealed within the experimental precision a constant mean island height ($N \approx 38$) and standard deviation ($\Delta N \approx 7$). The thickness of the Campbell phase was found to be $N \approx 26$ with $\Delta N \approx 5$ at room temperature and to decrease to $N \approx 22$ at 330 K and 360 K. A sketch of the height distribution at 360 K is shown in FIG. 6.5. Please note that in the RSM the lateral width of the diffraction peaks is dominated by the resolution function of the apparatus and hence no lateral crystal size can be determined. Therefore the lateral widths for the above sketch have been chosen to resemble the island size typically observed in AFM images. It is also noted that below 420 K no broadening of the peaks due to temperature is observed (see supplementary material).

The morphological information obtained proofs that after the deposition process the thin-film phase crystallites are larger than the Campbell phase crystallites. Therefore it is suggested that upon heating - in analogy to Ostwald ripening - the thin-film phase crystallites grow on the expense of the Campbell phase. This is confirmed by the slight increase of the thin-film phase intensity in FIG. 6.3. In contrast around 480 K it is supposed that the metastable thin-film phase transforms into the more stable Campbell phase. In view of the used model the constant height distribution hints that during the phase transition some of the thin-film phase crystallites transform

completely into the Campbell phase. This behavior is similar to powders or single crystals where around 470 K a phase transition from the Holmes phase to the Campbell phase was found (Siegrist et al.; 2007).

6.5. Conclusion

In summary, we have found that the thermal expansion of the thin-film phase is independent from the substrate and its non-linearity caused by the distinct packing of the molecules. Between 300 K and 400 K the initially observed Campbell phase vanishes while at higher temperatures a phase transition from the metastable thin-film phase to the more stable Campbell phase was found. The morphological information obtained indicates that some crystallites change their crystal structure completely while the largest part of the crystallites stays unchanged. These findings encourage molecular dynamics calculations (Yoneya et al.; 2010; Pizzirusso et al.; 2011) to further study the details of the phase transformation from the thin-film to the Campbell phase around 480 K.

6.6. Acknowledgement

We thank the European Synchrotron Radiation Facility and F. Zontone as well as O. Konovalov for assistance. This work was supported by the Austrian Science Fund (FWF):[P21094]

6.7. Supplementary Material

T [K]	RT	330	360	390	420	450	460	470	480	490
FWHM [$Å^{-1}$]	0.017	0.017	0.017	0.017	0.019	0.019	0.024	0.024	0.026	0.024

Table 6.1.: In-plane full width at half maximum (fitted with a Gaussian)of the (0,-2,0) peak ($q_p \approx 1.65$,$q_z \approx 0.25$) depending on the temperature. Below 420 K no broadening of the peaks due to temperature is observed.

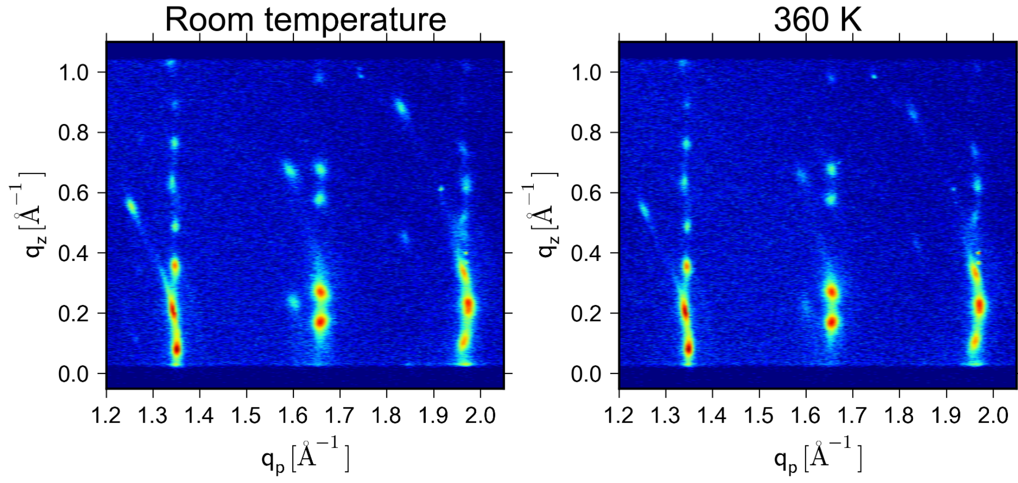

Figure 6.6.: Reciprocal space map of pentacene at room temperature and 360K. No influence of the increased temperature on the width of the peaks can be recognized. E.g. fitting the in-plane width of the (0 -2 0) peak ($q_p \approx 1.65$,$q_z \approx 0.25$) with a Gaussian gives for both temperatures a full width at half maximum (FWHM) of $\sigma = 0.017Å^{-1}$. Fitting the profile of this peak along the out of plane direction gives a FWHM of $\sigma = 0.028Å^{-1}$

6.8. Not Published Information

6.8.1. Unit Cell Determination

For the calculation of the expansion coefficients the unit cell parameters at each temperature step have been extracted. For this purpose the q_p and q_z position of three in-plane peaks (see Fig. 6.7) were determined via Gaussian fits of the corresponding line-scan. Also the q_z value of the specular 002 peak was extracted. With the data of this four peaks the unit cell was calculated using the following formulas.

$$a^* = \left|\frac{q_{h00}}{h}\right| \tag{6.3}$$

$$b^* = \left|\frac{q_{0k0}}{k}\right| \tag{6.4}$$

$$c^* = \left|\frac{q_{00l}}{l}\right| \tag{6.5}$$

$$\alpha^* = \arccos\left(\frac{\mathbf{q_{00l}q_{0k0}}}{|\mathbf{q_{00l}}||\mathbf{q_{0k0}}|}\right) \tag{6.6}$$

$$\beta^* = \arccos\left(\frac{\mathbf{q_{00l}q_{h00}}}{|\mathbf{q_{00l}}||\mathbf{q_{h00}}|}\right) \tag{6.7}$$

$$\gamma^* = \arccos\left(\frac{|\mathbf{q_{hk0}}|^2 - h^2a^{*2} - k^2b^{*2}}{2\cdot hk\cdot a^*\cdot b^*}\right) \tag{6.8}$$

The last equation (6.8) follows from

$$|\mathbf{q_{hk0}}|^2 = h^2a^{*2} + k^2b^{*2} + 2hk\cdot a^*b^*\cos\gamma^*.$$

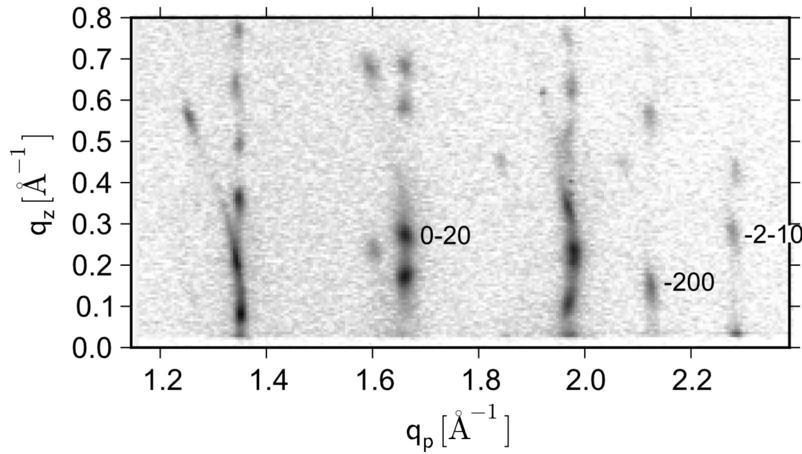

Figure 6.7.: In-plane peaks used for evaluation of the unit cell. The indices are given to the right of the corresponding peak.

7. Rate dependent phase behavior of α-sexithiophene

Evaporation rate dependent phase behavior of sexithiophene

Armin Moser[1], *Ingo Salzmann*[2], *Martin Oehzelt*[3], *Alfred Neuhold*[1], *Heinz-Georg Flesch*[1], *Jan Ivanco*[4,5], *Sergiu Pop*[5], *Teodor Toader*[5], *Dietrich R. T. Zahn*[5], *Detlef-Matthias Smilgies*[6], *Ján Jakabovič*[5],*Roland Resel*[1]

[1]Institute of Solid State Physics, Graz University of Technology, Austria
[2]Department of Physics, Humboldt-Universität zu Berlin, Germany
[3]Helmholtz-Zentrum Berlin für Materialien und Energie GmbH, Germany
[4]Institute of Physics, Slovak Academy of Sciences, Bratislava, Slovak Republic
[5]Institute of Physics, Chemnitz University of Technology, Chemnitz, Germany
[6]CHESS Center, Cornell University, USA

Applied Physics Letters
Under review

7.1. Abstract

This work reports the impact of the evaporation rate on the crystallographic phase formation of vacuum deposited α-sexithiophene thin films studied by X-ray diffraction methods. The experiments reveal the formation of two crystal phases of preferentially standing molecules, one of which is a thermodynamically stable phase occurring at low rates, while the second is favored by high rates. It exhibits an increased out-of-plane lattice spacing and diffraction features typical for liquid-crystalline phases. This frozen smectic phase of low order comprises molecules of nonuniform conformations, and is kinetically induced.

7.2. Introduction

Organic semiconductors in organic electronic devices generally exist as thin films and both their structural quality and crystalline order significantly impact the device performance. It was shown that only slight differences in the crystalline arrangement within distinct polymorphs (Dinelli et al.; 2004; Siegrist et al.; 2007; Mattheus et al.; 2003; Nabok et al.; 2007; Cheng and Lin; 2010) influence the intermolecular band dispersion and, hence, the charge transport properties (Troisi and Orlandi; 2005;

sample	D [Å]	T [K]	χ [Å/min]
a0	1560	300	36-360
a1	660	300	360-480
a2	600	411	3.6
b0	100	300	3
b1	250	300	5
b2	250	300	7

Table 7.1.: Sample designations, properties, and preparation parameters. D denotes the nominal film thickness, T the substrate temperature, χ the deposition rate.

Ambrosch-Draxl et al.; 2009; Nabok et al.; 2007). Numerous studies on polymorphism in organic thin-films identified the deposition parameters and the substrate nature to have a severe influence on the choice of polymorph. Moreover, it was reported that specific crystal structures different to the (mostly) solution-grown single-crystal polymorph are preferentially found in thin vacuum-deposited films (Schiefer et al.; 2007; Yoshida et al.; 2007; Nabok et al.; 2007; Salzmann et al.; 2011, 2008; Winter et al.; 2003). The crystal structure solution of such phases by grazing incidence X-ray diffraction (GIXD) is an emerging field (Yoshida et al.; 2007; Schiefer et al.; 2007; Nabok et al.; 2007; Moser et al.; 2009; Salzmann et al.; 2011; Mannsfeld et al.; 2011) and the identification of the physical parameters decisive for crystallization in a specific phase is of high importance to gain full control over the film-production process, thus, enabling a further optimization of future organic electronic devices.

In this study we investigated thin films of the prototypical p-type organic semiconductor α-sexithiophene (6T), which has been successfully employed in numerous applications including field-effect transistors (Cosseddu et al.; 2009; Fraboni et al.; 2010) and organic photovoltaic cells (Kouki et al.; 2010; Sakai et al.; 2009). Thin films were prepared by physical vapor deposition (PVD) under a precise variation of the deposition rate, which allowed elucidating the complex (co-)existence of the different crystalline phases (Servet et al.; 1994). In addition to identifying parameters that determine the existence of a specific phase, we found evidence for the smectic (Sm) nature of a 6T polymorph.

7.3. Experimental Details

Two sample series of 6T thin films were prepared by PVD on thermally oxidized silicon substrates at different substrate temperatures and deposition rates (TAB. 7.1). The nominal film thickness was measured by a quartz microbalance. The first series (samples a0-a2; deposition base pressure $< 5 \times 10^{-9}$ mbar) was investigated by specular X-ray diffraction (sXRD) and X-ray reflectivity (XRR) on a Bruker D8 Discover

in Bragg-Brentano geometry (CuK_α radiation, secondary graphite monochromator). The XRR data was fitted with the software GenX (Björck and Andersson; 2007), which calculates specular reflectivity according to the Parratt-formalism (Parratt; 1954) and uses a genetic algorithm for finding the global minimum in the parameter space utilizing a $Si/SiO_x/(N\times6T_{bilayer})$ layer-stack as model; to account for the crystalline nature of 6T the top layer was modeled by a sequence of bilayers with alternating electron density. Hence, the number of crystallographic layers (N) could be deduced from the fits. To obtain information on the lateral structure, GIXD investigations were performed. Reciprocal space maps (RSM) have been collected at the G2-Line of the Cornell High Energy Synchrotron Source using a one-dimensional detector and a wavelength of $\lambda = 1.30$ Å. The indexation of the RSM was done with the custom-made software PyGid, which calculates the Bragg-peak positions according to the scheme presented by Moser et al. (2009), while for the calculation of the structure factors the *Computational Crystallography Toolbox* (Grosse-Kunstleve et al.; 2002) was used. For the second samples series (b0 - b2, deposition base pressure $< 5 \times 10^{-8}$ mbar) sXRD experiments were performed at the W1 beamline of the synchrotron radiation source HASYLAB (DESY, Germany) with a wavelength of λ =1.18 Å and a LiF point detector.

To allow a geometry and wavelength independent representation all data is presented in the surface-reference frame (Moser et al.; 2009) with the in- and out-of-plane components of the scattering vector (q_p and q_z, respectively) given as coordinates.

7.4. Experimental Results

The sXRD data for two samples of the first series (a0, and a2) are compared in FIG. 7.1(a). The film deposited with lower rate on a substrate kept at elevated temperature (a2, top curve in Fig. 7.1(a)) only shows the 200 diffraction peak and higher order reflections. This indicates a pronounced texture of the film, that is, all crystallites are oriented with the (100)-lattice plane parallel to the substrate surface. From the characteristic lattice spacing the 6T low-temperature phase (LT-phase) (Horowitz et al.; 1995) is identified and the large observed number of higher-order reflections indicates good crystalline quality. In contrast, the film deposited with an elevated deposition rate at room temperature (a0, bottom line) shows – next to the h00 peaks – also the -411, -211, and 020 reflections of the LT-phase. In addition a series of diffraction peaks is observed, which corresponds to a lattice spacing of $d_{100} = 24.5$ Å (indexed as 100* and 200*). This lattice-plane distance was already reported before (Servet et al.; 1993, 1994) and the corresponding phase was denoted as β-phase of 6T. Note that the increase in specular lattice spacing found for the β-phase (compared to the LT-phase) is in-line with findings for several surface-mediated phases of other organic rod-like molecules (Yoshida et al.; 2007; Schiefer et al.; 2007; Nabok et al.; 2007; Salzmann et al.; 2011). Overall, we found that the film deposited at low rate and 411 K exclusively exhibits the LT-phase with only *one* crystalline orientation, whereas at elevated deposition rate both the β-phase and the LT-phase are simultaneously

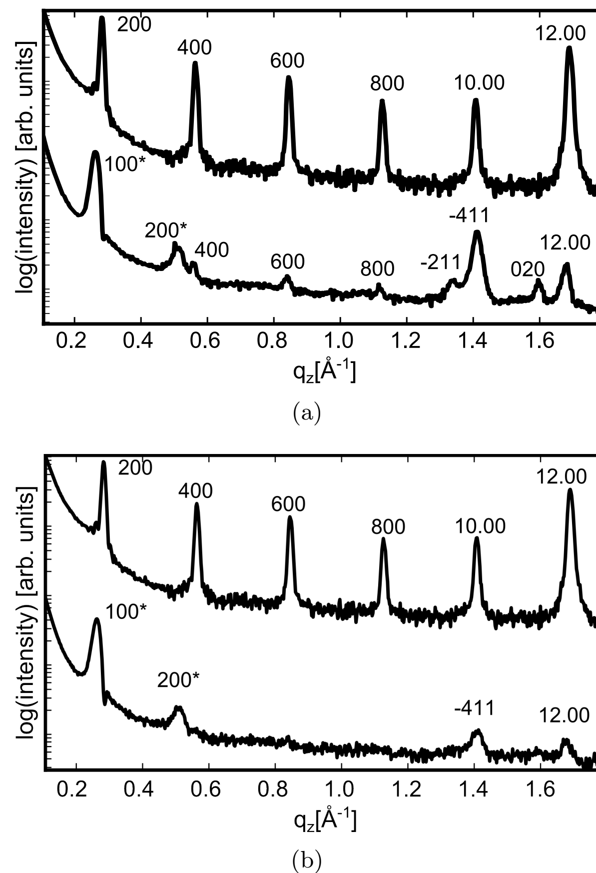

Figure 7.1.: **(a)** specular XRD scans of sample a2 (top line) and sample a0 (bottom line). **(b)** Specular XRD scans of sample a2 (top line) and sample a1 (bottom line). The diffraction peaks are indexed according to the LT-phase (indexed as hkl) and to the β-phase (indexed as hkl*).

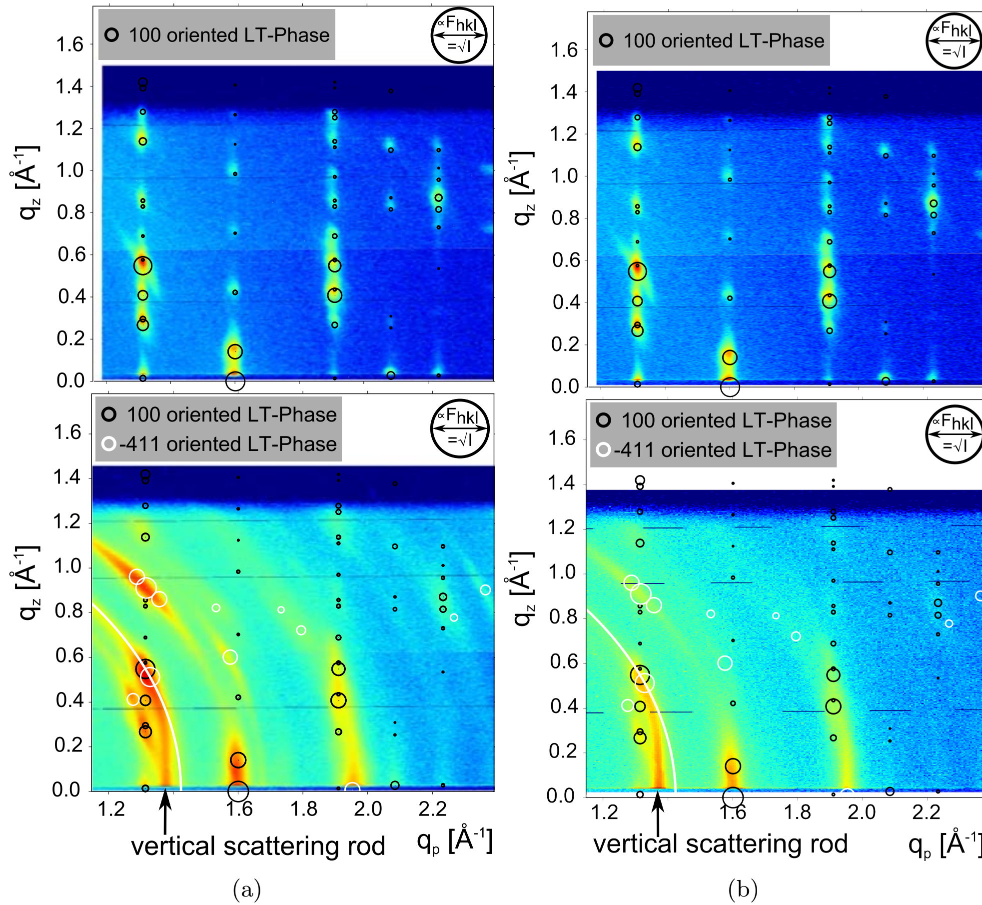

Figure 7.2.: **(a)** Reciprocal space maps of sample a2 (top) and a0 (bottom) on a logarithmic color scale together with indexation for a (100) (black) and (-411) (white) textured LT-phase. The large white ring is the Debye-Scherrer ring of the -4-11 diffraction peak. The vertical scattering rod at $q_p \approx 1.35Å^{-1}$ is marked by an arrow. **(b)** shows the reciprocal space maps of sample a2 (top) and a1 (bottom).

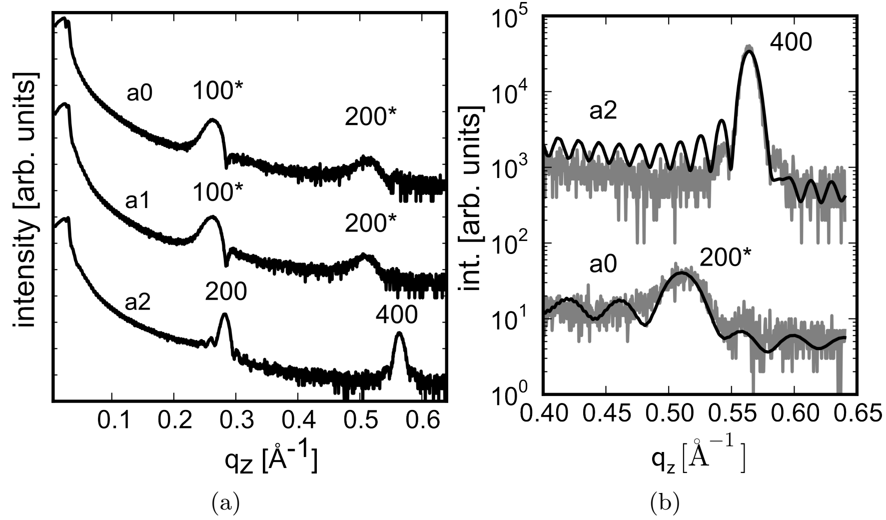

Figure 7.3.: **(a)** X-ray reflectivity data of the first sample series. The first two peaks of the LT-phase (hkl) and the β-phase (hkl*) are observed. **(b)** shows the fits (black line) of the 400 and 200* peak of the a2 and a0 sample. The fits were performed applying Parratt's formalism as described in the text. Note that for simplicity roughness was not included into the model and hence the thickness oscillations are too pronounced. From their periodicity and from the width of the main Bragg peak the number of crystallographic layers is still estimated reliably.

observed, where the latter shows a couple of preferred orientations of the crystallites.

Further information on the orientations and crystallographic phases is obtained from the GIXD experiments (FIG. 7.2). A comparison of the experimental data to calculated peak positions (center of rings) and intensities (area of rings) shows that the RSM of sample a2 is indeed fully explained by a (100)-textured LT-phase. In contrast, sample a0 is a mixture of (100) and (-411) oriented LT-phases. Notably, it is apparent that the peaks of the (-411) orientation are smeared out along Debye-Scherrer rings, which indicates a large mosaicity of the corresponding crystallites. Next to the diffraction peaks of the LT-phase a vertical scattering rod at $q_p \approx 1.35$ Å^{-1} is observed. Due to its straight vertical nature it can be excluded that it is caused by mosaicity, but is related to the β-phase already observed in the sXRD data (h00* series in FIG. 7.1). Interestingly, however, although the β-phase dominates the specular pattern, this scattering rod is the only β-phase derived diffraction feature in the map. Scattering rods in general arise from two-dimensional structures (Robinson and Tweet; 1992), which reveals 6T growth in a layered out-of-plane structure – observed by pronounced specular features – without inter-layer correlation of the lateral structure.

Further details about layer thickness and crystallinity are obtained by a quantitative evaluation of the XRR experiments (Fig. 7.3(a)). From fits of the Bragg peaks (Fig.

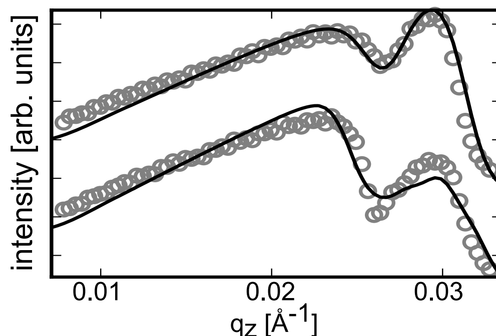

Figure 7.4.: X-ray reflectivity data (gray circles) and fits (black lines) of sample a2 (top) and a0 (bottom) around the critical angle of total reflection for 6T ($q_z \approx 0.024$ Å^{-1}) and the silicon-oxide substrate ($q_z \approx 0.03$ Å^{-1}) on a linear y-axis.

7.3(b)) the vertical size of crystalline domains can be estimated. From fitting the absorption observed in XRR data around the critical angles of 6T and silicon-oxide (SiO_x) (FIG. 7.4) the overall layer thickness can be deduced. For film a2 the peak width reveals LT-phase crystallites comprising $\approx$ 18 layers (equivalent to $\approx$ 400 Å) and the same thickness of $\approx$ 400 Å is found from the fit of the X-ray absorption. Hence, the LT-phase is coherently crystalline over its whole thickness. In contrast, sample a0 shows a layer thickness of 1500 Å, but, for the β-phase, only a comparably small crystalline domain-size of about 7 coherent layers (equivalent only 150 Å). Note that the data obtained for the thinner sample a1 shows both virtually identical specular and in-plane data (Fig. 7.1(a) and Fig. 7.2(b)). Therefore, we can clearly rule out an influence of the film thickness on the existence of a specific phase.

The sXRD data of the second sample series is depicted in FIG. 7.5. All three samples were deposited at room temperature with increasing deposition rate (shown from bottom to top). Clearly, depending on the different deposition rates, different phases are formed, which all are (100)-textured. The film prepared at smallest rate (bottom curve) exclusively shows the LT-phase, while that deposited at highest rate shows almost exclusively the β-phase and only a minor fraction of the LT-phase (top curve). Finally, the film achieved at medium rate represents an intermediate case exhibiting both the LT- and the β-phase. Overall, identical lattice-plane distances as reported for the first series above are observed. Comparing the peak widths of the peaks in FIG. 7.5 suggests a similar behavior as found for the first sample series: Again, the β-phase peaks arise from smaller crystallites (as deduced from the larger peak widths) than the LT-phase.

7.5. Discussion

Within this study thin films of 6T – vapor deposited at different deposition rates and substrate temperatures – were investigated by X-ray diffraction methods. Our

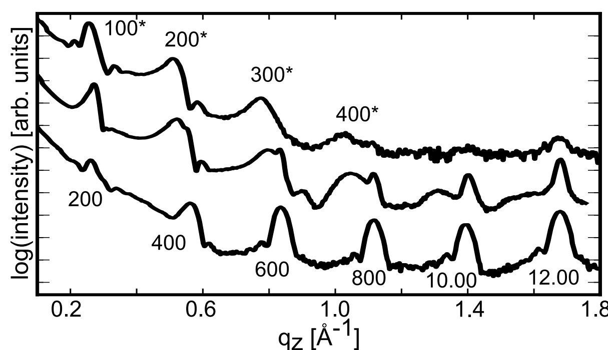

Figure 7.5.: Specular X-ray diffraction data of the second sample series (b0 – b2, from bottom to top). The peaks are indexed according to the LT-phase (hkl, bottom) and to the β-phase (hkl*, top).

experiments reveal that the deposition rate allows precisely tuning the phase ratio in 6T films at room temperature. This is demonstrated by the evaluation of two sample series, in which two 6T polymorphs, the LT- and the β-phase appear depending on the preparation parameters, both mainly in a standing ((100)-oriented) molecular orientation. At elevated deposition rates we found preferential formation of the β-phase, which has – compared to the LT-phase – an increased lattice plane distance d_{100}. For lower rates, the quantitative phase ratio sensitively depends on the deposition rates. If the deposition rate is just doubled from 3 to 7 Å/min the film entirely changes from being composed of LT-phase to being dominated by the β-phase. Increasing the rate further to very high values (samples a0, a1) does not significantly change the picture. Still, the same phases develop but, in contrast, the LT-phase now forms additional domains of lying ((-411) oriented) molecules. A possible explanation of this complex growth behavior is found in past studies for para-hexaphenyl, another rod like organic molecule. There it was reported that nuclei of lying molecules are first formed and that they undergo an orientational transition to standing molecules upon reaching a critical crystallite size (Potocar et al.; 2011). The analogous mechanism might apply for 6T growth and the reorientation from lying towards standing molecules is hindered at high deposition rates because the reorientation is limited to the surface of the grown film as orientations of adsorbed molecules are frozen by the consecutively deposited molecules. The mechanism affecting the molecular orientation in deposited molecular films have been a subject for numerous studies; the molecular orientation had been commonly assumed being determined by the interaction strength between the molecules and the substrate (Verlaak et al.; 2003). In contrast recent studies demonstrate the dominating role of growth kinetics governed by the surface order of substrates (Ivanco et al.; 2007; Djuric et al.; 2011). Here also the assumption of a kinetics-controlled molecular growth rationalizes the presence of lying molecules in the films grown at high deposition rates on a substrate otherwise inducing upright orientation.

Finally, the crystallographic characteristics of the β-phase remain to be discussed.

In the specular diffraction experiment with increasing rate the formation of the β-phase is observed together with an accompanying decrease of observed diffraction orders. Finally, at very high rates (samples a0, a1) only two specular peaks of the β-phase remain and the vertical crystallite size is small. Hence, an increase in rate is clearly detrimental to crystalline order and correlation length. The in-plane patterns of these samples reveal only one vertical scattering rod stemming from the β-phase (FIG. 7.2). Diffraction patterns, which show a well-pronounced diffraction in specular direction and significantly less defined peaks in the in-plane direction are typical for smectic phases (Seddon et al.; 2008b). Smectic A (SmA) or SmC phases (Barón; 2001; Seddon et al.; 2008a) show into in-plane direction one diffraction feature which is very broad into both q_z and q_p direction. SmB, SmF, or SmI phases, in contrast, show up to two scattering rods into in-plane direction. That is, diffraction features which are elongated along the q_z direction but well defined into q_p direction are expected. For details about the typical X-ray diffraction features of liquid crystalline materials please consult Seddon et al. (2008b). A precise analysis of the molecular packing, and, hence, the molecular conformation, is not possible for the β phase. However, we propose this liquid crystalline state to be caused by molecules of different conformations, because at the temperatures used for evaporation all possible internal conformations of the molecules are populated (Pizzirusso et al.; 2011), and due to the kinetic nature of the growth process the molecules do not reach the conformation required for the thermodynamical minimum-energy packing. This would be an all-trans conformation of the thiophene rings in the LT-phase crystal structure. Note that similar indications of liquid-crystalline states of 6T have been reported before, where a nematic state (Taliani et al.; 1990) was proposed, but X-ray diffraction data (Destri et al.; 1993) could not clearly identify its nature as nematic or smectic phase, and, more recently, indications for a SmA phase from molecular dynamics calculations (Pizzirusso et al.; 2011) were reported.

To conclude, in this work we studied the influence of deposition rate on the crystallographic phases of vacuum evaporated 6T thin films. Our experiments revealed the rate-dependent formation of the LT- and the β-phase of 6T as well as the rate-dependent growth of standing and lying LT-phase crystallites. A kinetically driven growth process was identified. While the LT-phase portion of the films – grown at low rates – exhibited high crystalline order, the high-rate β-phase was identified to be a frozen smectic state induced by growth kinetics. Our findings give evidence that the low deposition rates can be benefical for high crystalline quality of 6T functional layers.

The authors thank Yves Geerts for discussions about this topic and W. Caliebe (W1 beamline, DESY-HASYLAB, Hamburg, Germany) for experimental support. For financial support we thank the Austrian Science Fund:[21094]. Additionally this work is based upon research conducted at the Cornell High Energy Synchrotron Source (CHESS) which is supported by the NSF and NIH/NIGMS via NSF award DMR-0936384.

Bibliography

Ambrosch-Draxl, C., Nabok, D., Puschnig, P. and Meisenbichler, C. (2009). The role of polymorphism in organic thin films: oligoacenes investigated from first principles, *New Journal of Physics* **11**(12): 125010.

B. El-Kareh (1994). *Fundamentals of Semiconductor Processing Technologies* , Kluwer Academic Publishers, Dodrecht.

Barón, M. (2001). Definitions of basic terms relating to low-molar-mass and polymer liquid crystals (IUPAC Recommendations 2001), *Pure and Applied Chemistry* **73**(5): 845.

Bennett, D. (2010). *Understanding Single-Crystal X-Ray Crystallography*, Wiley-VCH Verlag, Weinheim.

Birkholz, M. (2006). *Thin Film Analysis by X-Ray Scattering*, 1st edn, Wiley-VCH Verlag, Weinheim.

Björck, M. and Andersson, G. (2007). GenX : an extensible X-ray reflectivity refinement program utilizing differential evolution, *Journal of Applied Crystallography* **40**(6): 1174.

Bloch, J. (1985). Angle and index calculations for 'z-axis' X-ray diffractometer, *J. Appl. Cryst.* **18**: 33.

Campbell, R. B., Robertson, J. M. and Trotter, J. (1961). The crystal and molecular structure of pentacene, *Acta Crystallographica* **14**(7): 705.

Campbell, R. B., Robertson, J. M. and Trotter, J. (1962). The crystal structure of hexacene, and a revision of the crystallographic data for tetracene, *Acta Crystallographica* **15**(3): 289.

Cheng, H. L. and Lin, J. W. (2010). Controlling Polymorphic Transformations of Pentacene Crystal through Solvent Treatments: An Experimental and Theoretical Study, *Cryst. Growth Des.* **10**(10): 4501.

Cosseddu, P., Vogel, J. O., Fraboni, B., Rabe, J. P., Koch, N. and Bonfiglio, A. (2009). Continuous Tuning of Organic Transistor Operation from Enhancement to Depletion Mode, *Adv. Mater.* **21**(3): 344.

Destri, S., Mascherpa, M. and Porzio, W. (1993). Mesophase formation in α-sexithienyl at high temperature –an X-ray diffraction study, *Advanced Materials* **5**(1): 43.

Dimitrakopoulos, C. D., Brown, A. R. and Pomp, A. (1996). Molecular beam deposited thin films of pentacene for organic field effect transistor applications, *Journal of Applied Physics* **80**(4): 2501.

Dinelli, F., Murgia, M., Levy, P., Cavallini, M., Biscarini, F. and de Leeuw, D. M. (2004). Spatially Correlated Charge Transport in Organic Thin Film Transistors, *Phys. Rev. Lett.* **92**: 116802.

Djuric, T., Ules, T., Flesch, H., Plank, H., Shen, Q., Teichert, C., Resel, R. and Ramsey, M. G. (2011). Epitaxially Grown Films of Standing and Lying Pentacene Molecules on Cu(110) Surfaces, *Crystal Growth & Design* **11**(4): 1015.

Dosch, H. (1987). Evanescent absorption in kinematic surface Bragg diffraction, *Phys. Rev. B* **35**: 2137–2143.

Favre-Nicolin, V. and Černý, R. (2002). *FOX*, 'free objects for crystallography': a modular approach to *ab initio* structure determination from powder diffraction, *Journal of Applied Crystallography* **35**(6): 734.

Feidenhans'l, R. (1989). Surface structure determination by X-ray diffraction, *Surface Science Reports* **10**(3): 105 – 188.
URL: *http://www.sciencedirect.com/science/article/pii/0167572989900022*

Flesch, H., Werzer, O., Weis, M., Jakabovič, J., Kováč, J., Haško, D., Jakopič, G., Wondergem, H. J. and Resel, R. (2009). A combined X-ray, ellipsometry and atomic force microscopy study on thin parylene-C films, *Physica Status Solidi (a)* **206**(8): 1727.

Fraboni, B., DiPietro, R., Cavallini, A., Cosseddu, P., Bonfiglio, A., Vogel, J. O., Rabe, J. P. and Koch, N. (2010). Correlating photocurrent spectra and electrical transport parameters in organic field effect transistors, *Org. Electron.* **11**(2): 273.

Fukuda, K., Sekitani, T. and Someya, T. (2009). Effects of annealing on electronic and structural characteristics of pentacene thin-film transistors on polyimide gate dielectrics, *Applied Physics Letters* **95**(2): 023302.

Grosse-Kunstleve, R. W., Sauter, N. K., Moriarty, N. W. and Adams, P. D. (2002). The Computational Crystallography Toolbox: crystallographic algorithms in a reusable software framework, *J. Appl. Cryst.* **35**: 126. `http://cctbx.sourceforge.net/`.

Haas, S., Batlogg, B., Besnard, C., Schiltz, M., Kloc, C. and Siegrist, T. (2007). Large uniaxial negative thermal expansion in pentacene due to steric hindrance, *Phys. Rev. B* **76**: 205203.

Haas, U., Haase, A., Maresch, H., Stadlober, B. and Leising, G. (2004). Growth process control of pentacene thin films and its application in full organic thin film transistors, *Polymers and Adhesives in Microelectronics and Photonics, 2004. POLYTRONIC 2004. 4th IEEE International Conference on*, pp. 219–224.

Holmes, D., Kumaraswamy, S., Matzger, A. J. and Vollhardt, K. P. C. (1999). On the Nature of Nonplanarity in the [N]Phenylenes, *Chemistry - A European Journal* **5**(11): 3399.

Horowitz, G., Bachet, B., Yassar, A., Lang, P., Demanze, F., Fave, J.-L. and Garnier, F. (1995). Growth and Characterization of Sexithiophene Single Crystals, *Chemistry of Materials* **7**(7): 1337.

Hummer, K., Puschnig, P., and Ambrosch-Draxl, C. (2003). Ab initio study of anthracene under high pressure, *Phys. Rev. B* **67**: 184105.

Ivanco, J., Haber, T., Krenn, J., Netzer, F., Resel, R. and Ramsey, M. (2007). Sexithiophene films on ordered and disordered TiO2 surfaces: Electronic, structural and morphological properties, *Surface Science* **601**(1): 178.

Ji, T., Jung, S. and Varadan, V. K. (2008). On the correlation of postannealing induced phase transition in pentacene with carrier transport, *Organic Electronics* **9**(5): 895.

Kanjilal, A., Ottaviano, L., Di Castro, V., Beccari, M., Betti, M. G. and Mariani, C. (2007). Pentacene Grown on Self-Assembled Monolayer: Adsorption Energy, Interface Dipole, and Electronic Properties, *The Journal of Physical Chemistry C* **111**(1): 286.

Kouki, F., Horowitz, G., Garnier, F. and Bouchriha, H. (2010). Photogeneration process in pristine sexithiophene based photovoltaic cells, *Org. Electron.* **11**(8): 1439.

Krischner, H. and Koppelhuber-Bitschnau, B. (1994). *Röntgenstrukturanalyse und Rietveldmethode*, 5th edn, Friedr. Vieweg und Sohn, Braunschweig.

Lee, H. S., Kim, D. H., Cho, J. H., Hwang, M., Jang, Y. and Cho, K. (2008). Effect of the Phase States of Self-Assembled Monolayers on Pentacene Growth and Thin-Film Transistor Characteristics, *Journal of the American Chemical Society* **130**(32): 10556.

Leenaers, A. J. G. and de Boer, D. K. G. (1997). Applications of Glancing Incidence X-Ray Analysis, *X-Ray Spectrometry* **26**(3): 115.

Lohmeier, M. and Vlieg, E. (1993). Angle calculations for a six-circle surface X-ray diffractometer, *J. Appl. Cryst.* **26**: 706.

Luger, P. (1980). *Modern X-Ray Analysis on Single Crystals*, Walter de Gruyter.

Mannsfeld, S. C. B., Tang, M. L. and Bao, Z. (2011). Thin Film Structure of Triisopropylsilylethynyl-Functionalized Pentacene and Tetraceno[2,3-b]thiophene from Grazing Incidence X-Ray Diffraction, *Advanced Materials* **23**(1): 127.

Marchl, M., Edler, M., Haase, A., Fian, A., Trimmel, G., Griesser, T., Stadlober, B. and Zojer, E. (2010b). Tuning the Threshold Voltage in Organic Thin-Film Transistors by Local Channel Doping Using Photoreactive Interfacial Layers, *Advanced Materials* **22**(47): 5361.

Marchl, M., Golubkov, A., Edler, M., Griesser, T., Pacher, P., Haase, A., Stadlober, B., Belegratis, M., Trimmel, G. and Zojer, E. (2010a). Photochemical control of the carrier mobility in pentacene-based organic thin-film transistors, *Applied Physics Letters* **96**(21): 213303.

Mattheus, C. C., Dros, A. B., Baas, J., Meetsma, A., de Boer, J. L. and Palstra, T. T. M. (2001). Polymorphism in pentacene, *Acta Crystallographica Section C Crystal Structure Communications* **57**(8): 939.

Mattheus, C. C., Dros, A. B., Baas, J., Oostergetel, G. T., Meetsma, A., de Boer, J. L. and Palstra, T. T. M. (2003). Identification of polymorphs of pentacene, *Synth. Met.* **138**(3): 475–481.

Mayer, A. C., Kazimirov, A. and Malliaras, G. G. (2006). Dynamics of Bimodal Growth in Pentacene Thin Films, *Physical Review Letters* **97**(10): 105503.

Moret, M., Campione, M., Borghesi, A., Miozzo, L., Sassella, A., Trabattoni, S., Lotz, B. and Thierry, A. (2005). Structural characterisation of single crystals and thin films of α,ω-dihexylquaterthiophene, *J. Mater. Chem.* **15**(25): 2444.

Moser, A. (2008). Crystal Structure Determination from Two-Dimensional Powders.

Moser, A., Werzer, O., Flesch, H.-G., Koini, M., Smilgies, D.-M., Nabok, D., Puschnig, P., Ambrosch-Draxl, C., Schiek, M., Rubahn, H.-G. and Resel, R. (2009). Crystal structure determination from two-dimensional powders: A combined experimental and theoretical approach, *Eur. Phys. J. Special Topics* **167**: 59.

Nabok, D., Puschnig, P., Ambrosch-Draxl, C., Werzer, O., Resel, R. and Smilgies, D. M. (2007). Crystal and electronic structures of pentacene thin films from grazing-incidence x-ray diffraction and first-principles calculations, *Phys. Rev. B* **76**(23): 235322.

Nefedov, A., Abromeit, A., Morawe, C. and Stierle, A. (1998). High-resolution x-ray scattering study of platinum thin films on sapphire, *Journal of Physics: Condensed Matter* **10**(4): 717.

Névot, L. and Croce, P. (1980). Caractérisation des surfaces par réflexion rasante de rayons X. Application à l'étude du polissage de quelques verres silicates, *Revue de Physique Appliquée* **15**(3): 19.

Oehzelt, M., Aichholzer, A., Resel, R., Heimel, G., Venuti, E. and Della Valle, R. G. (2006). Crystal structure of oligoacenes under high pressure, *Physical Review B* **74**(10): 104103.

Owens, D. K. and Wendt, R. C. (1969). Estimation of the surface free energy of polymers, *Journal of Applied Polymer Science* **13**(8): 1741.

Pacher, P., Lex, A., Proschek, V., Werzer, O., Frank, P., Temmel, S., Kern, W., Resel, R., Winkler, A., Slugovc, C., Schennach, R., Trimmel, G. and Zojer, E. (2007). Characterizing Chemically Reactive Thin Layers: Surface Reaction of [2-[4-(Chlorosulfonyl)phenyl]ethyl]trichlorosilane with Ammonia, *The Journal of Physical Chemistry C* **111**(33): 12407.

Parratt, L. G. (1954). Surface Studies of Solids by Total Reflection of X-Rays, *Phys. Rev.* **95**(2): 359.

Patterson, A. L. (1934). A Fourier Series Method for the Determination of the Components of Interatomic Distances in Crystals, *Phys. Rev.* **46**: 372–376.

Pizzirusso, A., Savini, M., Muccioli, L. and Zannoni, C. (2011). An atomistic simulation of the liquid-crystalline phases of sexithiophene, *Journal of Materials Chemistry* **21**(1): 125.

Potocar, T., Lorbek, S., Nabok, D., Shen, Q., Tumbek, L., Hlawacek, G., Puschnig, P., Ambrosch-Draxl, C., Teichert, C. and Winkler, A. (2011). Initial stages of a para-hexaphenyl film growth on amorphous mica, *Physical Review B* **83**(7): 075423.

Puschnig, P., Hummer, K., Ambrosch-Draxl, C., Heimel, G., Oehzelt, M. and Resel, R. (2003). Electronic, optical, and structural properties of oligophenylene molecular crystals under high pressure: An ab initio investigation, *Phys. Rev. B* **67**: 235321.

Rädler, J. (n.d.).
URL: *http://www.j-raedler.de/projects/polygon/*

Resel, R., Plank, H., Pogantsch, A., Leising, G. and Keckes, J. (2001). Twinning effects in polycrystalline hexaphenyl thin films, *Synthetic Metals* **121**(1-3): 1361.

Resel, R., Tamas, E., Sonderegger, B., Hofbauer, P. and Keckes, J. (2003). A heating stage up to 1173K for X-ray diffraction studies in the whole orientation space, *Journal of Applied Crystallography* **36**(1): 80.

Ribič, P. c. v. R., Kalihari, V., Frisbie, C. D. and Bratina, G. (2009). Growth of ultrathin pentacene films on polymeric substrates, *Phys. Rev. B* **80**(11): 115307.

Rietveld, H. M. (1969). A profile refinement method for nuclear and magnetic structures, *Journal of Applied Crystallography* **2**(2): 65.

Robinson, I. K. and Tweet, D. J. (1992). Surface X-ray diffraction, *Reports on Progress in Physics* **55**(5): 599.

Ruiz, R., Choudhary, D., Nickel, B., Toccoli, T., Chang, K., Mayer, A. C., Clancy, P., Blakely, J. M., Headrick, R. L., Iannotta, S. and Malliaras, G. G. (2004). Pentacene Thin Film Growth, *Chemistry of Materials* **16**(23): 4497.

Sakai, J., Taima, T., Yamanari, T. and Saito, K. (2009). Annealing effect in the sexithiophene:C(70) small molecule bulk heterojunction organic photovoltaic cells, *Sol. Energ. Mat. Sol. Cells.* **93**(6-7): 1149–1153.

Salzmann, I., Duhm, S., Heimel, G., Rabe, J. P., Koch, N., Oehzelt, M., Sakamoto, Y. and Suzuki, T. (2008). Structural order in perfluoropentacene thin films and heterostructures with pentacene, *Langmuir* **24**(14): 7294.

Salzmann, I., Nabok, D., Oehzelt, M., Duhm, S., Moser, A., Heimel, G., Puschnig, P., Ambrosch-Draxl, C., Rabe, J. P. and Koch, N. (2011). Structure Solution of the 6,13-Pentacenequinone Surface-Induced Polymorph by Combining X-ray Diffraction Reciprocal-Space Mapping and Theoretical Structure Modeling, *Cryst. Growth Des.* **11**(2): 600.

Salzmann, I. and Resel, R. (2004). STEREOPOLE: software for the analysis of X-ray diffraction pole figures with IDL, *J. Appl. Cryst.* **37**: 1029.

Schiefer, S., Huth, M., Dobrinevski, A. and Nickel, B. (2007). Determination of the crystal structure of substrate-induced pentacene polymorphs in fiber structured thin films, *J. Am. Chem. Soc.* **129**(34): 10316.

Schwarzenbach, D. (1993). *Crystallography*, 1st edn, John Wiley and Sons.

Seddon, J. M., Demus, D., Goodby, J., Gray, G. W., Spiess, H.-W. and Vill, V. (2008a). *Guide to the Nomenclature and Classification of Liquid Crystals*, Vol. 1, Wiley-VCH Verlag GmbH, Weinheim, pp. 17–25.

Seddon, J. M., Demus, D., Goodby, J., Gray, G. W., Spiess, H.-W. and Vill, V. (2008b). *Structural Studies of Liquid Crystals by X-Ray Diffraction*, Vol. 1, Wiley-VCH Verlag GmbH, Weinheim, pp. 635–679.

Servet, B., Horowitz, G., Ries, S., Lagorsse, O., Alnot, P., Yassar, A., Deloffre, F., Srivastava, P. and Hajlaoui, R. (1994). Polymorphism and Charge Transport in Vacuum-Evaporated Sexithiophene Films, *Chem. Mater.* **6**(10): 1809.

Servet, B., Ries, S., Trotel, M., Alnot, P., Horowitz, G. and Garnier, F. (1993). X-ray determination of the crystal structure and orientation of vacuum evaporated sexithiophene films, *Advanced Materials* **5**(6): 461.

Shmueli, U. (2007). *Theories and techniques of crystal structure determination*, IUCr texts on crystallography, Oxford University Press.

Shmueli, U. (ed.) (2006). *Reciprocal Space*, Vol. B of *International Tables for Crystallography*, 2nd (1st online) edn, Springer.

Siegrist, T., Besnard, C., Haas, S., Schiltz, M., Pattison, P., Chernyshov, D., Batlogg, B. and Kloc, C. (2007). A polymorph lost and found: The high-temperature crystal structure of pentacene, *Adv. Mater.* **19**(16): 2079.

Smilgies, D.-M. (2002). Geometry-independent intensity correction factors for grazing-incidence diffraction, *Rev. Sci. Inst.* **73**: 1706.

Smilgies, D.-M., Blasini, D. R., Hotta, S. and Yanagi, H. (2005). Reciprocal space mapping and single-crystal scattering rods, *J. Sync. Rad.* **12**: 807.

Stadlober, B., Haas, U., Maresch, H. and Haase, A. (2006). Growth model of pentacene on inorganic and organic dielectrics based on scaling and rate-equation theory, *Phys. Rev. B* **74**: 165302.

Taliani, C., Zamboni, R., Ruani, G., Rossini, S. and Lazzaroni, R. (1990). New Rigid Rod Liquid-Crystal Molecule Precursor of Conjugated Polymers: alpha-sexithienyl, *Journal of Molecular Electronics* **6**: 225.

Troisi, A. and Orlandi, G. (2005). Band structure of the four pentacene polymorphs and effect on the hole mobility at low temperature, *J. Phys. Chem. B* **109**(5): 1849.

Verlaak, S., Steudel, S., Heremans, P., Janssen, D. and Deleuze, M. S. (2003). Nucleation of organic semiconductors on inert substrates, *Phys. Rev. B* **68**(19): 195409.

Vincze, A., Jakabovič, J., Srnánek, R., Šatka, A., Kováč, J. j. and Kováč, J. (2009). Surface and interface properties of thin pentacene and parylene layers, *Central European Journal of Physics* **7**: 270.

Weißmantel, C. and Hamann, C. (1995). *Grundlagen der Festkörperphysik*, 4th edn, Johann Ambrosius Barth Verlag, Heidelberg.

Winter, B., Ivanco, J., Netzer, F. and Ramsey, M. (2003). Ordered mono- and multilayer films of sexiphenyl on Al(111): a LEED investigation, *Thin Solid Films* **433**: 269. Proceedings from the 12th International Conference on Thin Films.

Wu, Y., Toccoli, T., Koch, N., Iacob, E., Pallaoro, A., Rudolf, P. and Iannotta, S. (2007). Controlling the Early Stages of Pentacene Growth by Supersonic Molecular Beam Deposition, *Phys. Rev. Lett.* **98**: 076601.

Yagi, I., Tsukagoshi, K. and Aoyagi, Y. (2004). Growth control of pentacene films on SiO2/Si substrates towards formation of flat conduction layers, *Thin Solid Films* **467**(1–2): 168.

Yang, H., Kim, S., Yang, L., Yang, S. and Park, C. (2007). Pentacene Nanostructures on Surface-Hydrophobicity-Controlled Polymer/SiO2 Bilayer Gate-Dielectrics, *Advanced Materials* **19**(19): 2868.

Yang, H., Shin, T. J., Ling, M.-M., Cho, K., Ryu, C. Y. and Bao, Z. (2005). Conducting AFM and 2D GIXD Studies on Pentacene Thin Films, *Journal of the American Chemical Society* **127**(33): 11542.

Yoneya, M., Kawasaki, M. and Ando, M. (2010). Molecular dynamics simulations of pentacene thin films: The effect of surface on polymorph selection, *Journal of Materials Chemistry* **20**(46): 10397.

Yoshida, H., Inaba, K. and Sato, N. (2007). X-ray diffraction reciprocal space mapping study of the thin film phase of pentacene, *Appl. Phys. Lett.* **90**(18): 181930.

Yoshida, H. and Sato, N. (2008). Crystallographic and electronic structures of three different polymorphs of pentacene, *Phys. Rev. B* **77**(23): 235205.

Zhang, F., Xu, Z., Liu, X., Zhao, S., Lu, L., Wang, Y. and Xu, X. (2009). Studies on morphology and molecular arrangement of pentacene on different substrates, *Superlattices and Microstructures* **45**(6): 612.

Part III.

Appendix

A. Fourier Synthesis of Electron Density

As outlined in the main text, the electron density is the Fourier transform of the structure factors

$$\rho_e(x_f, y_f, z_f) = \frac{1}{V} \sum_{h=-\infty}^{\infty} \sum_{k=-\infty}^{\infty} \sum_{l=-\infty}^{\infty} F(hkl) e^{2\pi i (hx_f + ky_f + lz_f)}. \tag{A.1}$$

Changing the summations to run from 0 to ∞ and writing the electron density for only two dimensions it follows

$$\rho_e(x_f, y_f) = \frac{1}{A} \sum_{h=0}^{\infty} \sum_{k=0}^{\infty} \underbrace{F(hk) e^{2\pi i (hx_f + ky_f)} + F(-h-k) e^{2\pi i (-hx_f - ky_f)}}_{\spadesuit} + \tag{A.2}$$

$$+ \underbrace{F(-hk) e^{2\pi i (-hx_f + ky_f)} + F(h-k) e^{2\pi i (hx_f - ky_f)}}_{\clubsuit}. \tag{A.3}$$

For real valued data (electron densities) the relation

$$F(hk) = F(-1 \cdot (hk))^* \tag{A.4}$$

$$A_{hk} + iB_{hk} = A_{-h-k} - iB_{-h-k} \tag{A.5}$$

holds. Using Euler's identity ($e^{i\phi} = \cos\phi + i \sin\phi$), and writing $(hx_f + ky_f) = \mathbf{kr}$ it follows

$$\spadesuit = (A_{hk} + iB_{hk})(\cos(2\pi\mathbf{kr}) + i \sin(2\pi\mathbf{kr})) + \tag{A.6}$$

$$+(A_{hk} - iB_{hk})(\cos(2\pi\mathbf{kr}) - i \sin(2\pi\mathbf{kr})) \tag{A.7}$$

$$= \underline{2A_{hk} \cos(2\pi(hx_f + ky_f)) - 2B_{hk} \sin(2\pi(hx_f + ky_f)).} \tag{A.8}$$

$\clubsuit$ follows analogously and hence the electron density is

$$\rho_e(x_f, y_f) = \frac{2}{A} \sum_{h=0}^{\infty} \sum_{k=0}^{\infty} A_{hk} \cos(2\pi(hx_f + ky_f)) - B_{hk} \sin(2\pi(hx_f + ky_f)) + \tag{A.9}$$

$$+A_{-hk} \cos(2\pi(hx_f + ky_f)) - B_{-hk} \sin(2\pi(hx_f + ky_f)). \tag{A.10}$$

This last equation explicitly expresses that the electron density is the sum of plane waves with the real part of the structure factor the cosine amplitude and the imaginary part the sine amplitude. Additionally it is revealed that the amplitudes of waves with anti parallel wave vectors are the same. Hence only one term will be considered in the images showed in the following.

Two examples for two dimensional electron densities are shown on the next two pages. The first column shows the structure factors as function of h and k. From top to bottom successively terms (frequencies) of the Fourier series are added, starting from the terms with the highest amplitude. This sequence is shown in the structure factor plot as red number. The actual term added in the last step (plane wave) is shown colored in the second column on top of the original electron density (grey scale). The third column shows the actual interpolation, i.e. the sum of all so far selected terms. The last column finally shows the original electron density that was used to calculated the structure factors. This images should just illustrate that the best fitting frequencies show the highest intensities. They should also emphasize, that from one Bragg peak and its higher order reflections only information in the direction of the wave vector and no lateral one can be obtained.

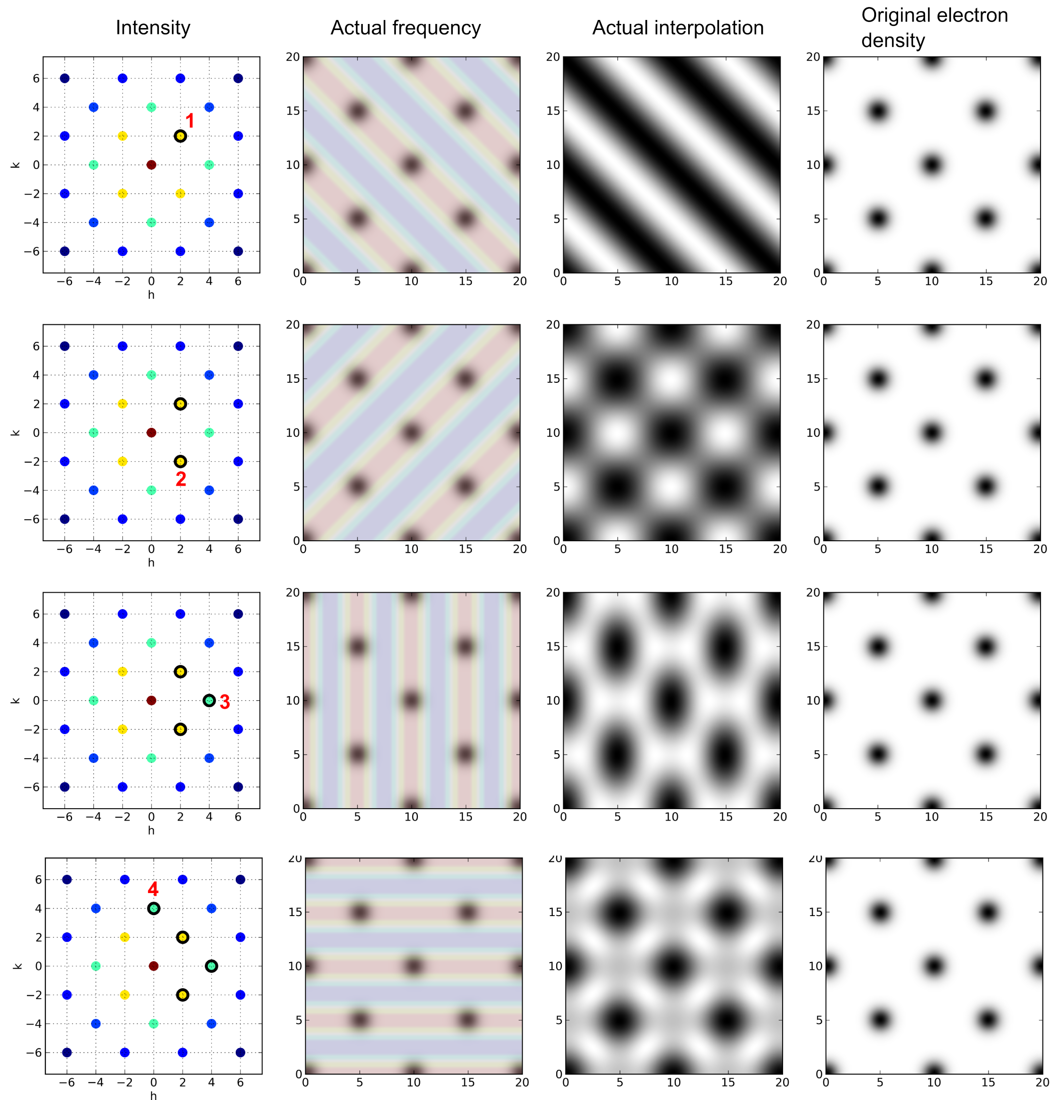

Figure A.1.: Fourier synthesis of a two-dimensional analogue of a silicon crystal.

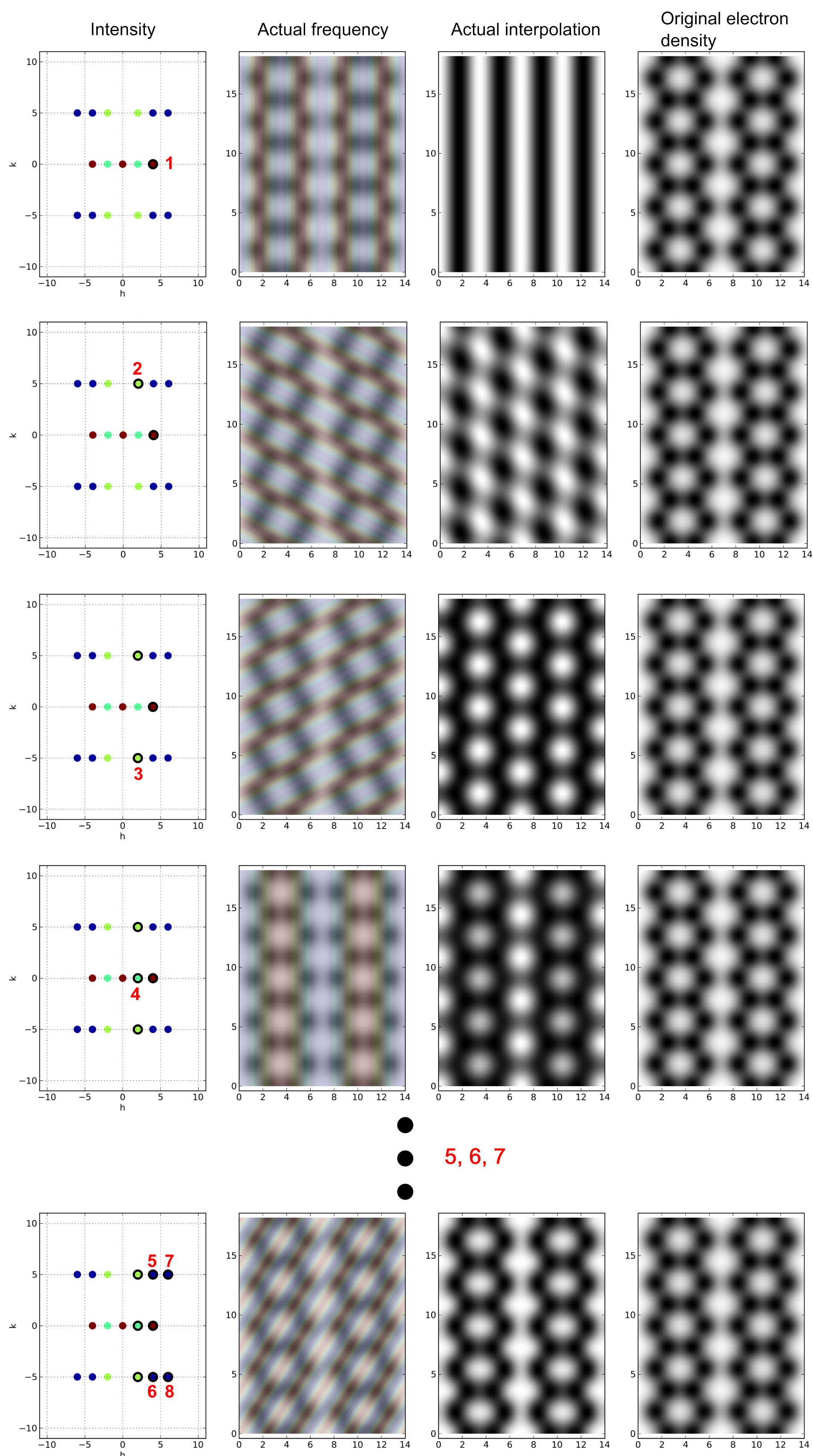

Figure A.2.: Fourier synthesis of two dimensional pseudo pentacene molecules.